Tobias Pankewitz

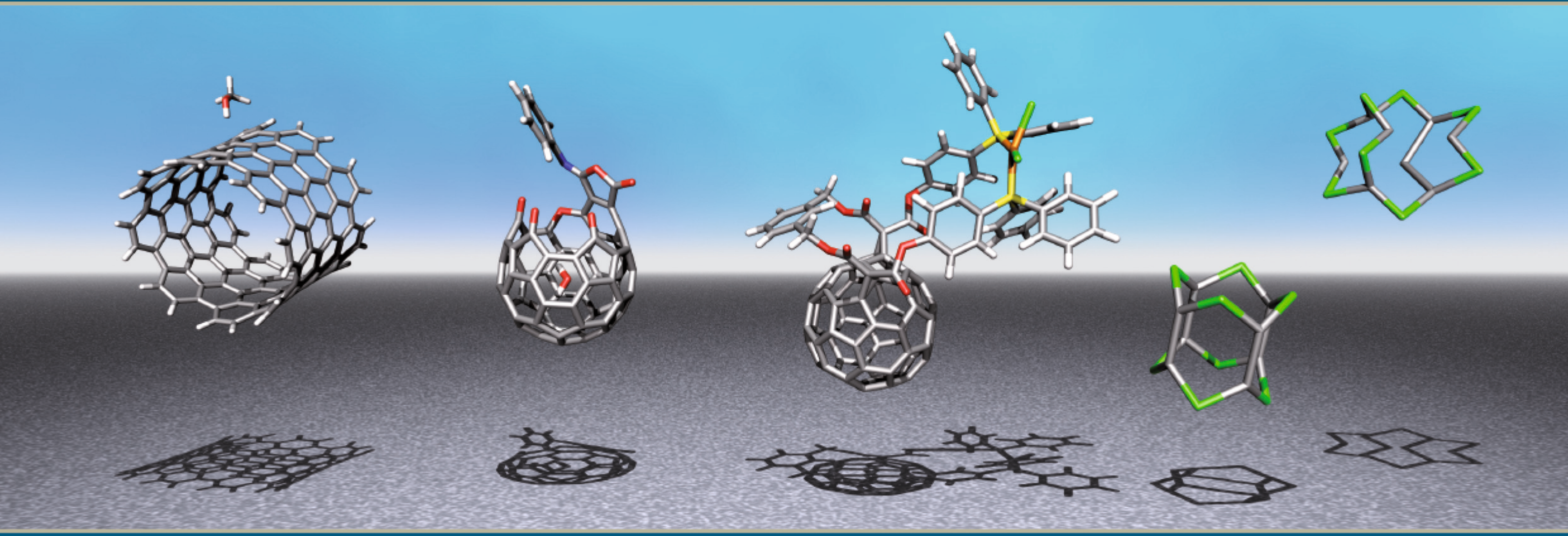

On the Diverse Bonding Situations in Nanostructures

An Ab Initio Computational Study

KIT Scientific Publishing

Tobias Pankewitz

On the Diverse Bonding Situations in Nanostructures

An Ab Initio Computational Study

On the Diverse Bonding Situations in Nanostructures

An Ab Initio Computational Study

by
Tobias Pankewitz

KIT Scientific
Publishing

Dissertation, Karlsruher Institut für Technologie
Fakultät für Chemie und Biowissenschaften,
Tag der mündlichen Prüfung: 21. Oktober 2009

Impressum

Karlsruher Institut für Technologie (KIT)
KIT Scientific Publishing
Straße am Forum 2
D-76131 Karlsruhe
www.uvka.de

KIT – Universität des Landes Baden-Württemberg und nationales
Forschungszentrum in der Helmholtz-Gemeinschaft

SOME RIGHTS RESERVED

Diese Veröffentlichung ist im Internet unter folgender Creative Commons-Lizenz
publiziert: http://creativecommons.org/licenses/by-nc-nd/3.0/de/

KIT Scientific Publishing 2010
Print on Demand

ISBN 978-3-86644-450-8

On the Diverse Bonding Situations in Nanostructures – An Ab Initio Computational Study

Zur Erlangung des akademischen Grades eines

Doktors der Naturwissenschaften
(Dr. rer. nat.)

von der Fakultät für Chemie und Biowissenschaften des
Karlsruher Instituts für Technologie (KIT) - Universitätsbereich
angenommene

Dissertation

von

Diplom-Chemiker

Tobias Pankewitz

aus Speyer

Dekan:	Prof. Dr. S. Bräse
Referent:	Prof. Dr. W. Klopper
Korreferent:	Prof. Dr. M. Elstner
Tag der mündlichen Prüfung:	21. Oktober 2009

Meiner Familie

Danksagung
Acknowledgement

An erster Stelle möchte ich mich bei Prof. Dr. Willem M. Klopper, dem Betreuer meiner Arbeit, bedanken. Ihm ist es gelungen, mir neben vielen Freiräumen auch die nötige Unterstützung zu geben, die zum Erfolg dieser Arbeit wichtig war.
Prof. Dr. Marcus Elstner danke ich für die Übernahme des Korreferats.

Prof. Dr. Hansgeorg Schnöckel und Dr. Patrick Henke möchte ich für die gute Zusammenarbeit im Bereich der Aluminium- und Magnesiumverbindungen danken, die zu so interessanten Ergebnissen geführt hat.
Auch dem Arbeitskreis von Prof. Dr. Stefan Bräse, im speziellen Dr. Thierry Muller, danke ich für die gute Zusammenarbeit und die freundliche Bereitstellung von Strukturen der Fullerenliganden.
I sincerely thank Prof. Liangbing Gan (Peking) for providing a preprint of the experimental results on the water encapsulation in [59]fullerenones and the crystal structures of the compounds discussed.
Many thanks also to Prof. Dr. George E. Froudakis (Heraklion) for a Fortran program to easily generate tube coordinates.

I want to thank Dr. Yannick Carissan (Marseille) for several helpful and inspiring discussions concerning carbon materials.
Dr. David Tew I sincerely thank for patiently sharing his knowledge.

My special thanks to Ericka Barnes (Middletown) for her dedicated help, carefully proofreading the whole manuscript and correcting some of my 'Germish'. She was a nice but strict thesis buddy, egging me to meet personal deadlines.

Dr. Andreas Glöß und Dr. Marco Kattanek danke ich für ihre geduldige Hilfe bei allen auftretenden Soft- und Hardwareproblemen und die vielen Dinge, die ich im Bereich der Computersystemadministration von ihnen lernen durfte.
Many thanks to Dr. Jorge Aguilera who shared the office with me the last four years for many interesting scientific and also non-scientific discussions.
Allen jetzigen und ehemaligen Mitgliedern der Karlsruher Theoretischen Chemie danke ich für die angenehme, kollegiale Atmosphäre und die schöne gemeinsame Zeit.

Contents

1. Introduction 1

2. Theoretical Background of Applied Methods 3
- 2.1. Introduction 3
- 2.2. Wavefunction-based methods 4
  - 2.2.1. Hartree–Fock theory and the self-consistent field procedure 5
  - 2.2.2. Møller–Plesset perturbation theory 6
  - 2.2.3. Coupled cluster theory 8
- 2.3. Density functional theory 9
  - 2.3.1. Exchange–Correlation functionals 11
  - 2.3.2. Technical details 14
- 2.4. Recent enhancements to DFT and MP2 methods 15
  - 2.4.1. Dispersion corrected DFT 16
  - 2.4.2. Spin-component-scaled MP2 17
- 2.5. Basis sets 19
- 2.6. Potential energy surface 22
  - 2.6.1. Structure optimisation 22
  - 2.6.2. Transition state search 23
- 2.7. Software 25

3. Applications – A Walk through Nanoscience 27
- 3.1. Benchmarking DFT-D with model systems 27
  - 3.1.1. Interaction of methanol with benzene 28
  - 3.1.2. Interaction of methanol with coronene 33
- 3.2. Single-walled carbon nanotubes 36
  - 3.2.1. Electronic properties of finite SWCNTs 38
  - 3.2.2. Interaction of small primary alcohols with SWCNTs 46
- 3.3. Water encapsulation in open cage [59]fullerenones 58
  - 3.3.1. Equilibrium structures of H_2O@[59]fullerenones 61
  - 3.3.2. Transition state structures of H_2O@[59]fullerenones 66
- 3.4. Metal complexes with functionalised fullerene ligands 70

3.5. Subvalent aluminium and magnesium compounds – on the diversity of metal–metal bonding 78
  3.5.1. Isomers of Al_2F_4 and Al_2Cl_4 – model compounds for Al_2R_4 species 82
  3.5.2. Oligomeric clusters of Mg_2Cl_2 87

4. Summary **99**

Zusammenfassung in Deutscher Sprache **101**

A. Abbreviations **103**

B. Copyright Permissions **107**

List of Tables **109**

List of Figures **113**

Bibliography **119**

1. Introduction

Computational chemistry's main focus is on the characterisation of molecules, of their structures, spectroscopic properties, energetics, and kinetics by way of numerical calculations. With progress in the development of robust quantum chemical methods, coupled with the rapid increase in computer power, the close symbiosis between theory and experiment in solving problems of chemical relevance has become characteristic for modern chemistry.

Two classes of carbon-based nanostructures, namely, the fullerenes[1] that were characterised in 1985 and carbon nanotubes that were discovered by Iijima[2] in 1991, are intriguing examples of how theoretical investigations and predictions can stimulate new experiments, and vice versa. In the last 20 years, numerous experimental and theoretical works have contributed to a comprehensive knowledge of these systems.[3,4] The development of new nanomaterials involves studies of nanostructures ranging from single molecules to surfaces and bulk materials. Thus, the computational chemist engaged in this field is facing more and more extended systems. Two important questions arise in this context: "Which computational method can I afford for this certain system of interest?" and "Is the chosen method able to describe the physics of my system with sufficient accuracy?" This balanced interplay between applicability and accuracy is a major issue to address prior to any application.

Today, modern density functional theory is routinely applied to many extended systems. The method performs with a robustness and efficiency that continually pushes the limit for the system size under consideration. Nevertheless, the method reveals some serious deficiencies, in particular, the calculation of weak interactions. Because of this, benchmarking the chosen computational method with higher-accuracy methods or experimental results remains essential.

Actual and potential uses of nanostructures range from storage materials to chemical sensors, from nanoelectronics to host–guest interactions with pharmaceutical relevance, *i.e.* drug delivery and tailored materials with desired properties.[5–10] Many of these system properties are characterised by a wide variety of bonding situations, ranging from weak interactions through space to strong metal–ligand bonds and metal–metal bonds between metal centres in rare oxidation states. Thus, fundamental investigations on these nanostructures, or models of them, are essential for further understanding.

The goal of the present work is to investigate a variety of nanostructures in the framework of density functional theory. Rigorous benchmarking is key to evaluating the balance between computational costs and accuracy of the methods used, and shall ensure the significance of the results. Wavefunction-based correlation methods will be utilised in cases where higher accuracy is required. The applications presented in this work cover a wide range of molecular interactions, from dispersive interactions to covalent metal–ligand and metal–metal bonding, and are selected on the basis of pressing questions that arise from experiments.

This dissertation is organised as follows: Chapter 2 presents the underlying theory of the computational methods utilised. Chapter 3 commences with a benchmark study on the description of weak interactions that are ruled by dispersion, using the two model systems benzene–methanol and coronene–methanol. The results of this study serve as a basis for the following two applications, firstly, the investigation of small primary alcohols interacting with single-walled carbon nanotubes in section 3.2 and secondly, water-encapsulation in open-cage [59]fullerenones in section 3.3. Section 3.4 links carbon-based nanostructures with metal-containing nanomaterials, investigating the complexation of metal centres with functionalised fullerene ligands. Finally, section 3.5 deals with subvalent aluminium and magnesium compounds, focusing on the metal–metal bond itself and the structural diversity of complexes on the way to bulk material. A conclusive summary and closing remarks can be found in chapter 4.

2. Theoretical Background of Applied Methods

The computational methods utilised throughout the present work and their underlying theory shall be outlined in this chapter. However, the main intention is to classify the applied methods with respect to their level of intrinsic approximations, to determine the computational accuracy and costs, and to focus on practical requisites, rather than to give a comprehensive overview on theoretical chemistry itself.

2.1. Introduction

Molecules are many-particle composites consisting of nuclei and electrons, thus the methods of quantum mechanics (QM) must be employed for a valid description of their electronic structure. In fact, in the field of quantum chemistry (QC) the chemical properties of molecules are derived by solving the many-particle problem.

Stationary states of a molecule are given by the solutions of the non-relativistic time-independent Schrödinger equation[11,12]

$$\hat{H}\Psi = E\Psi \tag{2.1}$$

The solution with the lowest energy eigenvalue defines the ground state of the molecule. The Born–Oppenheimer approximation, that is, the separation of nuclear and electronic motion, reduces the computational challenge to solving only the electronic part of the Schrödinger equation,

$$\hat{H}_{\mathrm{el}}\Psi_{\mathrm{el}} = E_{\mathrm{el}}\Psi_{\mathrm{el}} \tag{2.2}$$

where the nuclear positions are treated as parameters. The electronic Hamiltonian operator, $\hat{H}_{\mathrm{el}}$, contains the kinetic energy of the electrons ($\hat{T}_{\mathrm{e}}$), the nuclear–electron attraction ($\hat{V}_{\mathrm{ne}}$) and the electron–electron ($\hat{V}_{\mathrm{ee}}$) and nuclear–nuclear ($\hat{V}_{\mathrm{nn}}$) repulsions

$$\hat{H}_{\mathrm{el}} = \hat{T}_{\mathrm{e}} + \hat{V}_{\mathrm{ne}} + \hat{V}_{\mathrm{ee}} + \hat{V}_{\mathrm{nn}} = \sum_{i=1}^{N_{\mathrm{elec}}} \hat{h}_i + \sum_{i<j}^{N_{\mathrm{elec}}} \hat{g}_{ij} + \hat{V}_{\mathrm{nn}} \tag{2.3}$$

Collecting the operators by the number of electron indices yields the one-electron operator $\hat{h}_i$, describing the motion of electron i with spatial position $\mathbf{r}_i$ in the field of all the nuclei (Z_a denotes the charge of nucleus a at position $\mathbf{R}_a$)

$$\hat{h}_i = -\frac{1}{2}\nabla_i^2 - \sum_{a=1}^{N_{\text{nuclei}}} \frac{Z_a}{|\mathbf{R}_a - \mathbf{r}_i|} \tag{2.4}$$

and the two-electron operator $\hat{g}_{ij}$, describing the electron–electron repulsion

$$\hat{g}_{ij} = \frac{1}{|\mathbf{r}_i - \mathbf{r}_j|} \tag{2.5}$$

The operators are given in atomic units ($m_\text{e} = e = \hbar = 1$).
Exact solutions to the electronic Schrödinger equation are unknown for systems with more than one electron due to the two-electron operator $\hat{g}_{ij}$, and thus it must be solved in an approximate fashion. These approximations shall be discussed in the following sections.

2.2. Wavefunction-based methods

The Hartree–Fock (HF) method is the simplest ansatz for approximately solving the molecular Schrödinger equation.[13–15] In the complete basis set limit, the HF wave function is able to account for $\sim$99% of the total energy (HF limit). However, in most cases the missing 1% is essential for the valid description of system properties of chemical relevance (*e.g.* structural parameters, binding energies, reaction enthalpies, vibrational frequencies and so forth). The difference of the exact, non-relativistic energy, E, and the HF energy, E_{HF}, defines the correlation energy, E_{corr}

$$E = E_{\text{HF}} + E_{\text{corr}} \tag{2.6}$$

The source of the energy difference is attributed to the *independent-particle* ansatz of HF theory, which approximates the electron–electron interaction in a mean-field fashion even though the motions of the individual electrons are correlated. *Post*-HF methods are aimed at describing the 'missing' part of the HF energy, E_{corr}, and are consequently called 'correlation methods'.
In the present work, two correlation methods are employed for benchmarking purposes: the Møller–Plesset perturbation theory (MP) and the coupled cluster theory (CC).[16–18] The Hartree–Fock method providing the zeroth order reference and the MP and CC approaches for the correlation treatment are presented in the following sections.

2.2.1. Hartree–Fock theory and the self-consistent field procedure

In Hartree–Fock theory, the wave function Ψ is approximated by a single Slater determinant

$$\Phi_{\mathrm{SD}} = \frac{1}{\sqrt{N!}} \begin{vmatrix} \phi_1(1) & \phi_2(1) & \cdots & \phi_N(1) \\ \phi_1(2) & \phi_2(2) & \cdots & \phi_N(2) \\ \vdots & \vdots & \ddots & \vdots \\ \phi_1(N) & \phi_2(N) & \cdots & \phi_N(N) \end{vmatrix} \tag{2.7}$$

that is, an antisymmetrised product of N orthonormal spin-orbitals ϕ_i, where N refers to the number of electrons in the system. The spin-orbitals ϕ_i are also referred to as molecular orbitals (MOs). Employing the variational principle to minimise the energy with respect to the MOs yields the canonical Hartree–Fock equations

$$\hat{f}\phi_i = \epsilon_i \phi_i \tag{2.8}$$

where ϕ_i are the canonical Hartree–Fock orbitals, and the eigenvalues ϵ_i are the corresponding orbital energies. The Fock operator, $\hat{f}$ is an effective one-electron energy operator

$$\hat{f} = \hat{h} + \hat{J} - \hat{K} \tag{2.9}$$

It gives for an electron the kinetic energy of that electron and the attraction to all the nuclei (via $\hat{h}$), as well as an averaged repulsion to all the other electrons (via the Coulomb and exchange operators $\hat{J}$ and $\hat{K}$). It is this averaged repulsion to all other electrons that is referred to by the aforementioned *mean-field* approximation of HF theory.

In practical use, a basis set expansion is employed, expressing the unknown MOs in terms of a set of known functions. This linear combination of atomic orbitals (LCAO) to form MOs is an invaluable tool in electronic structure theory and is widely used. The LCAO expansion of an MO ϕ_i is

$$\phi_i = \sum_{\alpha}^{M_{\mathrm{basis}}} c_{\alpha i} \chi_\alpha \tag{2.10}$$

where $c_{\alpha i}$ are the expansion coefficients and χ_α the atomic orbitals (AOs). The Hartree–Fock equations in the AO basis yield the Roothaan–Hall equations which are written in matrix notation as

$$\mathbf{FC} = \mathbf{SC}\boldsymbol{\epsilon} \tag{2.11}$$

In the equation above, $\mathbf{F}$ denotes the Fock matrix, $\mathbf{S}$ the overlap matrix, $\mathbf{C}$ the coefficients matrix and $\boldsymbol{\epsilon}$ the diagonal matrix of orbital energies.

The Roothaan–Hall equations must be solved in an iterative procedure starting with a set of guess MO coefficients. This set of initial MO coefficients is optimised within each iteration until it produces a self-consistent field (SCF). The convergence of the SCF procedure is controlled by an energy criterion for the change in the HF energy within two consecutive iterations. Start MOs for all calculations performed in the present work are obtained by a semiempirical extended Hückel theory (EHT) calculation.
A formal scaling of $\mathcal{O}(N^4)$ with the system size N arises only for HF methods that calculate the full set of two-electron integrals (*i.e.* disk-based HF methods) since the total number of these integrals increases as N^4. However, *direct* HF methods utilising integral prescreening techniques (*e.g.* the HF program of TURBOMOLE[19,20]) show a reduced scaling between $\mathcal{O}(N^2)$ and $\mathcal{O}(N^3)$, depending on the dimensionality of the atomic arrangement and the compactness of the basis set used.[21,22]

2.2.2. Møller–Plesset perturbation theory

The simplest ansatz to add the missing electron correlation to the HF solution is a perturbation theory approach. Møller–Plesset perturbation theory (MP) defines the Hamiltonian $\hat{H}$ as composed of an unperturbed reference, $\hat{H}_0$, and the perturbation $\hat{H}'$

$$\hat{H} = \hat{H}_0 + \lambda \hat{H}' \tag{2.12}$$

where λ determines the strength of the perturbation. The unperturbed Hamiltonian, $\hat{H}_0$, is chosen as the sum over Fock operators

$$\hat{H}_0 = \sum_{i}^{N_\text{elec}} \hat{f}_i \tag{2.13}$$

Thus, the perturbed operator $\hat{H}'$ gives the difference between the exact and the mean electron–electron interaction. As the Hamiltonian $\hat{H}$ depends on λ, the same holds for the wave function Ψ and the corresponding energy E. Both can be given as Taylor series with λ as the expansion coefficient

$$\Psi = \Psi_0 + \lambda \Psi_1 + \lambda^2 \Psi_2 + \cdots \tag{2.14}$$

$$E = E_0 + \lambda E_1 + \lambda^2 E_2 + \cdots \tag{2.15}$$

Plugging the expansions into the Schrödinger equation and collecting terms by the power of λ yields the Møller–Plesset perturbation equations. Solving these equations gives the following expressions for the zeroth-order and first-order energies

$$E_0 = \langle\Psi_0|\,\hat{H}_0\,|\Psi_0\rangle = \langle\Psi_0|\sum_{i}^{N_{\text{elec}}} \hat{f}_i\,|\Psi_0\rangle = \sum_{i}^{N_{\text{elec}}} \epsilon_i \tag{2.16}$$

$$E_1 = \langle\Psi_0|\,\hat{H}'\,|\Psi_0\rangle \tag{2.17}$$

The zeroth-order energy is just a sum of MO energies. Both, the zeroth-order and first-order energy evaluations only require the zeroth-order wave function, Ψ_0, that is, the HF determinant. The zeroth-order and first-order energies sum to the HF energy

$$E_{\text{HF}} = E_0 + E_1 \tag{2.18}$$

Thus, the second-order energy (a sum of two-electron integrals over MOs) is the first correction term introducing electron correlation

$$E_2 = \sum_{i<j}^{\text{occ}} \sum_{a<b}^{\text{vir}} \frac{\langle ij\|\,ab\,\rangle\,\langle ab\|\,ij\,\rangle}{\epsilon_i + \epsilon_j - \epsilon_a - \epsilon_b} \tag{2.19}$$

The calculation of the Møller–Plesset perturbation correction up to second-order defines the MP2 model. The MP2 method and the MP methods in general are non-variational but size extensive.

MP2 typically accounts for 80–90% of the correlation energy and thus represents a computationally inexpensive approach (when compared to other correlation methods) of including the majority of the electron correlation effects.[22] However, it is obvious from the perturbation ansatz that MP2 only performs well in cases where the HF reference wave function already is a good approximation to the exact wave function. Furthermore, MP2 energies show slow convergence with the basis set size and consequently, MP2 calculations demand large orbital basis sets.

As an MP2 calculation consists of the HF reference wave function calculation ($\sim \mathcal{O}(N^2)$–$\mathcal{O}(N^3)$), the AO to MO integral transformation ($\mathcal{O}(N^5)$), and the MP2 energy calculation ($\mathcal{O}(N^4)$), the formal scaling with the system size N (in parenthesis) indicates the rate limiting step in the large system limit. However, this limit is actually not reached in any of the MP2 calculations performed throughout this work. Even for the largest system calculated, that is, $H_2O@C_{60}$ in a def2-QZVP basis set comprising a total of about 3500 basis functions, the HF reference calculation remains by a factor of 2–3 the most time consuming part of the entire calculation.

2.2.3. Coupled cluster theory

Coupled cluster (CC) theory employs an exponential ansatz for the wave function

$$\Psi_{\mathrm{CC}} = \exp(\hat{T})\Psi_0 = \sum_{k=0}^{\infty} \frac{1}{k!}\hat{T}^k\Psi_0 \tag{2.20}$$

where $\hat{T}$ is an excitation operator working on the HF reference wave function Ψ_0. This excitation operator, $\hat{T}$, is defined as

$$\hat{T} = \hat{T}_1 + \hat{T}_2 + \hat{T}_3 + \cdots + \hat{T}_{N_{\mathrm{elec}}} \tag{2.21}$$

in such a way that the $\hat{T}_n$ operator acting on the HF reference wave function generates all n-tuple excited Slater determinants by exciting n electrons from occupied orbitals $i, j, \ldots$ to virtual orbitals $a, b, \ldots$ (equations are given here for $\hat{T}_1$ and $\hat{T}_2$)

$$\hat{T}_1\Psi_0 = \sum_{i}^{\mathrm{occ}}\sum_{a}^{\mathrm{vir}} t_i^a\Psi_i^a \tag{2.22}$$

$$\hat{T}_2\Psi_0 = \sum_{i<j}^{\mathrm{occ}}\sum_{a<b}^{\mathrm{vir}} t_{ij}^{ab}\Psi_{ij}^{ab} \tag{2.23}$$

The expansion coefficients t are termed *amplitudes* in CC theory. A similarity transformation of the Hamiltonian operator and projection of the Schrödinger equation onto the n-tuply excited determinants, μ_n, yields the coupled cluster equations

$$\langle\mu_n|\, e^{-\hat{T}}\hat{H}e^{\hat{T}}\, |\Psi_0\rangle = 0 \tag{2.24}$$

These form a coupled set of non-linear equations that must be solved iteratively to determine the amplitudes. The coupled cluster energy is then obtained from

$$E_{\mathrm{CC}} = \langle\Psi_0|\, \hat{H}e^{\hat{T}}\, |\Psi_0\rangle = E_{\mathrm{HF}} + \Delta\mathrm{CC} \tag{2.25}$$

where E_{HF} is the HF energy.

The truncation of the excitation operator $\hat{T}$ defines the coupled cluster method, *i.e.* CCS with $\hat{T} = \hat{T}_1$, CCSD with $\hat{T} = \hat{T}_1 + \hat{T}_2$, CCSDT with $\hat{T} = \hat{T}_1 + \hat{T}_2 + \hat{T}_3$ and so forth. The CC methods are non-variational but size extensive. CCSD formally scales as $\mathcal{O}(N^6)$, and CCSDT as $\mathcal{O}(N^8)$ with the system size N. In order to reduce the extremely high computational cost associated with CCSDT, the triples contribution is evaluated by perturbation theory and added to the CCSD results in the CCSD(T) model[23]

$$E_{\mathrm{CCSD(T)}} = E_{\mathrm{HF}} + \Delta\mathrm{CCSD} + \Delta(\mathrm{T}) \tag{2.26}$$

The evaluation of the perturbative triples contribution $\Delta(\mathrm{T})$ requires terms from fourth- and fifth-order perturbation theory. Consequently, CCSD(T) formally scales as $\mathcal{O}(N^7)$ with system size. Due to fortuitous cancellation (the overestimation of triples contribution in the perturbative treatment cancels the error that results from the neglect of the quadruples and higher excitations) CCSD(T) even outperforms the full CCSDT model.[24] Given that a sufficiently large basis set is employed, the CCSD(T) method is able to meet the goal of 'chemical accuracy' ($\sim 4\,\mathrm{kJ\,mol^{-1}}$) for most systems. In the hierarchy of computational approaches employed in the present work, CCSD(T) is the most accurate but at the same time the most costly method.

2.3. Density functional theory

The basis of density functional theory (DFT) is the first Hohenberg–Kohn theorem,[25] that the ground state expectation value, O_0, of any observable $\hat{O}$ is a functional of the ground state electron density ρ_0

$$O_0 = O[\rho_0] = \langle \Psi[\rho_0] | \, \hat{O} \, | \Psi[\rho_0] \rangle \tag{2.27}$$

Thus, in DFT the electron density of a system is the central quantity that has to be evaluated and once it is known, the system's energy, wave function and any other property is uniquely defined.

The number of electrons, N, is the simplest quantity that can be derived by spatial integration of the electron density

$$N[\rho] = \int \rho(\mathbf{r}) d\mathbf{r} \tag{2.28}$$

where $N[\rho]$ denotes that the number of electrons is a *functional* of the electron density. Perhaps the most important observable (functional) is the energy of the system

$$E[\rho] = T[\rho] + E_{\mathrm{ne}}[\rho] + E_{\mathrm{ee}}[\rho] \tag{2.29}$$

where $T[\rho]$ is the kinetic energy and $E_{\mathrm{ne}}[\rho]$ and $E_{\mathrm{ee}}[\rho]$ are the nuclear–electron and electron–electron interaction energies.

Unfortunately, the exact functional $E[\rho]$ is unknown due to two contributions to the total energy. Whereas the functional for the nuclear–electron attraction energy is given as

$$E_{\mathrm{ne}}[\rho] = -\sum_{a}^{N_{\mathrm{nuclei}}} \int \frac{Z_a \rho(\mathbf{r})}{|\mathbf{R}_a - \mathbf{r}|} d\mathbf{r} \tag{2.30}$$

there is only one part of $E_{\mathrm{ee}}[\rho]$, the classical Coulomb contribution

$$J[\rho] = \frac{1}{2} \iint \frac{\rho(\mathbf{r}_1)\rho(\mathbf{r}_2)}{|\mathbf{r}_1 - \mathbf{r}_2|} d\mathbf{r}_1 d\mathbf{r}_2 \tag{2.31}$$

known. The second problematic contribution is the kinetic energy term, $T[\rho]$, whose exact functional form is only known for the uniform electron gas, that is, the Thomas–Fermi model (a poor approximation for molecules).[26,27] The practical solution to this problem employed in computational chemistry is the Kohn–Sham (KS) formalism,[28] which splits the kinetic energy functional into two parts: a known contribution, $T_{\mathrm{s}}[\rho]$, of the non-interacting system that has the same density as the real system and the missing part, the kinetic correlation energy $(T[\rho] - T_{\mathrm{s}}[\rho])$, which is added in an approximate manner. The same procedure is applied to the unknown functional $E_{\mathrm{ee}}[\rho]$. The total energy of the real system then is

$$\begin{aligned} E[\rho] &= T_{\mathrm{s}}[\rho] + E_{\mathrm{ne}}[\rho] + J[\rho] + (T[\rho] - T_{\mathrm{s}}[\rho]) + (E_{\mathrm{ee}}[\rho] - J[\rho]) = \\ &= T_{\mathrm{s}}[\rho] + E_{\mathrm{ne}}[\rho] + J[\rho] + E_{\mathrm{XC}}[\rho] \end{aligned} \tag{2.32}$$

where the unknown energy contributions are collected in the exchange–correlation functional $E_{\mathrm{XC}}[\rho]$. Note that with KS theory, orbitals (the KS orbitals) have to be re-introduced into the DFT methods for calculating $T_{\mathrm{s}}[\rho]$ with sufficiently high accuracy.

The Kohn–Sham equations are a set of pseudo-eigenvalue equations

$$\hat{h}^{\mathrm{KS}} \phi_i^{\mathrm{KS}} = \epsilon_i \phi_i^{\mathrm{KS}} \tag{2.33}$$

where $\hat{h}^{\mathrm{KS}}$ is an effective one-electron operator, similar to the Fock operator in HF theory ($\hat{f}$ in eq. 2.9). An LCAO expansion of the KS orbitals analogously yields the matrix equation in the AO basis (compare with eq. 2.11)

$$\mathbf{h}^{\mathrm{KS}} \mathbf{C} = \mathbf{S} \mathbf{C} \boldsymbol{\epsilon} \tag{2.34}$$

that has to be solved in an iterative SCF procedure.

DFT methods describe molecules at a correlated level via the inclusion of electron correlation in the E_{XC} functional. It is the approximate form of the $E_{\mathrm{XC}}[\rho]$ functional used that distinguishes various DFT methods from each other and that determines the accuracy of the calculations. A major drawback of DFT methods is the lack of a systematic way of extending a series of calculations to approach the exact result as it is known for wavefunction-based methods (*e.g.* the CC series). Nevertheless, there exists a hierarchy of density functional approximations organised by the ingredients in E_{XC} that allows for a rough estimate of the accuracy one can expect for a certain property of interest (cf. eqs. 2.35–2.37). On the first (and lowest) rung are pure functionals of the electron density based on the local density approximation (LDA).

$$E_{\mathrm{XC}}^{\mathrm{LDA}}[\rho] \tag{2.35}$$

$$E_{\mathrm{XC}}^{\mathrm{GGA}}[\rho, \nabla\rho] \tag{2.36}$$

$$E_{\mathrm{XC}}^{meta-\mathrm{GGA}}[\rho, \nabla\rho, \nabla^2\rho] \tag{2.37}$$

On the second rung follows the generalised gradient approximation (GGA) with E_{XC} functionals of the density and the first derivative of the density that provide significant improvements in accuracy for calculating molecules. Functionals on the third rung, the *meta*-GGA functionals, additionally depend on higher order derivatives of the electron density, *i.e.* the second order term $\nabla^2\rho$ or, alternatively, the orbital kinetic energy density τ. Including fractions of exact HF exchange to GGA or *meta*-GGA functionals results in the so-called hybrid functionals. Examples of LDA, GGA, *meta*-GGA, and hybrid functionals are discussed in the following section, based on the functionals employed in the DFT calculations of the present work.

2.3.1. Exchange–Correlation functionals

When constructing approximate functional forms for the exchange–correlation energy, the separation of E_{XC} into a pure exchange part, E_{X}, and a correlation part, E_{C}, as

$$E_{\mathrm{XC}} = E_{\mathrm{X}} + E_{\mathrm{C}} \tag{2.38}$$

is customary and founded on the physics of the exchange and the correlation contributions having different scaling properties.

Local density approximation

The model of the uniform (or homogeneous) electron gas is the basis of the local density approximation. The LDA assumes a slowly varying electron density that can be described locally by this model. The exact functional of the exchange energy for the uniform electron gas is given by the Dirac formula[29,30]

$$E_{\mathrm{X}}^{\mathrm{LDA}} = -\frac{3}{4}\left(\frac{3}{\pi}\right)^{\frac{1}{3}} \int \rho(\mathbf{r})^{\frac{4}{3}} d\mathbf{r} \tag{2.39}$$

An exact analytic form of the corresponding correlation energy functional, $E_{\mathrm{C}}^{\mathrm{LDA}}$, is unknown. However, the correlation energy of the uniform electron

gas has been determined by highly accurate numerical quantum Monte–Carlo simulations and there exist analytic formulas for $E_{\mathrm{C}}^{\mathrm{LDA}}$, where the most popular ones derived by Vosko, Wilk, and Nusair (VWN) as well as a newer functional form by Perdew and Wang (PW) are fitted to these results.[31–33]
The LDA approximation is suitable for extended systems, such as metals, with a close to homogeneous electron distribution. However, the electron density in molecular systems is by no means homogeneous, that is, the uniform electron gas is an invalid approximation. Consequently, LDA calculations of molecules give much too short bond distances and severely overestimate interaction energies ($\sim 100\,\mathrm{kJ\,mol^{-1}}$ for bond energies).[34]

Generalised gradient approximation

A first step towards accounting for the inhomogeneities in the electron density of molecular systems (a non-uniform electron gas) is achieved by the generalised gradient approximation, which incorporates the gradient of the electron density into the functional form of E_{XC} (gradient-corrected functionals). In 1988, Becke pioneered one of the most popular GGA exchange functionals (B88) as a correction to $E_{\mathrm{X}}^{\mathrm{LDA}}$.[35] It provides a substantial improvement to the LDA exchange energy and has the correct asymptotic behaviour for the energy density while containing only a single adjustable parameter β (determined by fitting to data of the rare gas atoms). Combining the B88 correction for the exchange energy with Perdew's correction to the correlation energy (P86)[36,37] results in the BP86 functional

$$E_{\mathrm{XC}}^{\mathrm{BP86}} = E_{\mathrm{X}}^{\mathrm{LDA}} + E_{\mathrm{X}}^{\mathrm{B88}} + E_{\mathrm{C}}^{\mathrm{VWN}} + E_{\mathrm{C}}^{\mathrm{P86}} \tag{2.40}$$

whereas the alternative combination with the correlation energy functional of Lee, Yang, and Parr (LYP) yields the BLYP functional[38]

$$E_{\mathrm{XC}}^{\mathrm{BLYP}} = E_{\mathrm{X}}^{\mathrm{LDA}} + E_{\mathrm{X}}^{\mathrm{B88}} + E_{\mathrm{C}}^{\mathrm{LYP}} \tag{2.41}$$

The correlation functional P86 is derived from properties of the uniform electron gas and employs one empirical parameter that was fitted to the correlation energy of the Ne atom. In contrast, LYP is not based on the homogeneous electron gas but is derived from an analytic expression for the correlation energy of the helium atom.
Another GGA functional by Perdew, Burke, and Ernzerhof (PBE) contains four non-empirical parameters that are purely derived from select properties the exact functional would have, omitting any fitting to experimental data[39]

$$E_{\mathrm{XC}}^{\mathrm{PBE}} = E_{\mathrm{X}}^{\mathrm{LDA}} + E_{\mathrm{X}}^{\mathrm{PBE}} + E_{\mathrm{C}}^{\mathrm{PW}} + E_{\mathrm{C}}^{\mathrm{PBE}} \tag{2.42}$$

The GGA functionals in general improve on the pure LDA results for most molecular systems and provide reliable structural parameters with sufficient mutual agreement among the various functionals. However, the quality of energetics strongly depends on the chosen systems and occasionally reveals major discrepancies for different GGA functionals.

Higher order gradient methods

Higher order gradient methods are the logical extensions to the GGA functionals. The class of *meta*-GGA functionals depends (apart from the density and the density gradient) also on the second order derivatives of the electron density, $\nabla^2\rho$, or the orbital kinetic energy density $\tau(\mathbf{r})$

$$\tau(\mathbf{r}) = \frac{1}{2}\sum_i^{\text{occ}} |\nabla\phi_i(\mathbf{r})|^2 \tag{2.43}$$

The orbital kinetic energy density, τ, and the Laplacian of the density, $\nabla^2\rho$, are interrelated by the KS orbitals and thus contain essentially the same information about the system. The recent exchange–correlation functional of Tao, Perdew, Staroverov, and Scuseria (TPSS)

$$E_{\text{XC}}^{\text{TPSS}} = E_{\text{X}}^{\text{LDA}} + E_{\text{X}}^{\text{TPSS}} + E_{\text{C}}^{\text{PW}} + E_{\text{C}}^{\text{TPSS}} \tag{2.44}$$

is constructed as a non-empirical *meta*-GGA functional for describing both molecules and solids.[40] The TPSS functional produces structural parameters that are comparable to GGA results but provides noticeable improvements for energetics of molecules when compared to similarly constructed GGA functionals (*i.e.* PBE).[41,42]

Hybrid functionals

In absolute numbers, the exchange contributions to the total energy are usually an order of magnitude larger than the corresponding correlation effects. Thus, a straightforward approach for further improvements would be the combination of the exact exchange energy (HF exchange of a single Slater determinant) with just the correlation part, E_{C} of existing GGA or *meta*-GGA functionals. However, this approach fails for molecular systems, yielding poor results when compared to common GGA functionals with approximate forms of E_{XC}. The failure of the procedure originates from the essentially artificial separation of E_{XC} in an individual exchange and correlation part. Gritsenko *et al.* have shown that virtually all GGA exchange functionals are designed in such a way that they

effectively represent not only the exchange contributions, but also the molecular non-dynamical correlation, while the corresponding GGA correlation functionals represent dynamical correlation only.[43] Thus, dropping the $E_{\mathrm{X}}^{\mathrm{GGA}}$ functional part in favour of exact exchange also neglects part of the correlation energy.
Based on the adiabatic connection formula (λ-dependence of E_{XC}) the suitable portion of exact HF exchange to include into the functional is deduced for different hybrid functionals. The most popular hybrid model is the B3LYP method based on Becke's 3-parameter-functional (B3)

$$E_{\mathrm{XC}}^{\mathrm{B3LYP}} = (1-a)E_{\mathrm{X}}^{\mathrm{LDA}} + aE_{\mathrm{X}}^{\mathrm{HF}} + bE_{\mathrm{X}}^{\mathrm{B88}} + (1-c)E_{\mathrm{C}}^{\mathrm{VWN}} + cE_{\mathrm{C}}^{\mathrm{LYP}} \tag{2.45}$$

where the parameters a, b, and c are fitted to experimental data (atomisation energies, ionisation potentials and proton affinities of systems consisting of elements from the second and third period) resulting in values of $a = 0.20$, $b = 0.72$, and $c = 0.81$.[44,45]
The success of hybrid functionals, and of B3LYP in particular, is founded on the improved results for organic molecules (compared to pure GGAs) and the good performance for main group compounds in general.

2.3.2. Technical details

The exchange–correlation potential, V_{XC}, is a complex functional of the electron density and in case of GGAs and *meta*-GGAs also of derivatives of the density or the KS orbitals. As a result, a general analytical solution for the integrals of the exchange–correlation energy is inaccessible and thus, a numerical integration scheme employing grids (quadrature of exchange–correlation terms) has to be performed.
The numerical integration is performed by decomposing the integrand into atomic contributions f_a and evaluating the corresponding integrals by separate radial and spherical quadrature

$$\int f_a(\mathbf{r})d\mathbf{r} = \int_0^\infty \int_\Omega r^2 f_a(r,\omega)drd\omega \approx \sum_p w_p^{\mathrm{rad}} \sum_q w_q^{\mathrm{spher}} f_a(r,\omega) \tag{2.46}$$

where w_p^{rad} and w_q^{spher} are the quadrature weights of the radial and spherical contributions. A radial integration scheme of the Gauß–Chebyshev type and a spherical integration scheme using the efficient octahedral Lebedev grids is implemented in TURBOMOLE.[46] Grids of different size are available in TURBOMOLE ranging from *grid 1* (coarse) to *grid 7* (finest) and for the multiple grids from *m3* to *m5*. The latter employ a coarser grid (1–3) during the SCF iterations, while employing the fine grid (3–5) in the final energy and gradient evaluations.

Two problems associated with the use of finite grids for the evaluation of E_{XC} arise. Firstly, since all the grids are incomplete, the numerically evaluated energies (spherical integration) are dependent on the orientation of the molecule within the grid. Due to a certain error per atom, summing up to the total error in E_{XC} for a molecule, this sensitivity of the energy to rotations of the molecule aggravates for larger systems. Especially for molecules with numerous atoms regularly ordered along a select axis, as for example in nanotubes, the error due to rotations is getting more distinct (no fortuitous cancellation) and fine-meshed grids are needed (final energies for carbon nanotubes are evaluated in the present work with the finest *grid 7*).

Secondly, when assuming a general expression for the approximate numerical quadrature of E_{XC}

$$E_{\text{XC}} \approx \tilde{E}_{\text{XC}} = \sum_g w_g f_g \tag{2.47}$$

where the weights w_g are products of the atomic and quadrature weights w_a, w_p^{rad}, and w_q^{spher} and where f_g are the atomic contributions to E_{XC}, the first derivative of $\tilde{E}_{\text{XC}}$ with respect to a generalised coordinate (*e.g.* the gradient) is given as

$$\frac{d}{d\tau}\tilde{E}_{\text{XC}} = \sum_g \left(f_g \frac{d}{d\tau} w_g + w_g \frac{d}{d\tau} f_g \right) \tag{2.48}$$

The first term in the summation gives the weight function derivatives, that do not vanish for a finite grid but are most of the time neglected in standard calculations. As a consequence the gradient does not vanish for the real minima on the potential energy surface and the supposedly calculated 'minimum' structures showing a zero-gradient deviate from the real minimum structures. The TURBOMOLE program allows to account for the weight derivatives which is strongly recommended for molecules possessing shallow potential minima (enable optionally) and especially for the calculation of higher order derivatives (*e.g.* the Hessian to obtain vibrational frequencies, automatically enabled).

2.4. Recent enhancements to DFT and MP2 methods

Improvements in computational accuracy are addressed not only by new method developments, but also by enhancements to already established methods. These improvements aim to address known deficiencies, as well as to conserve the efficiency and robustness that are characteristic of that method. In this section, an enhancement to DFT methods and a modification to MP2 are discussed.

2.4.1. Dispersion corrected DFT

The term 'dispersion' describes long-range attractive forces that act through space between separate molecules or different parts of the same molecule, even in the absence of charges or permanent electric moments. Also termed as van der Waals (vdW) interaction, dispersion is a quantum-mechanical phenomenon that originates from many-particle effects. Thus, dispersion is purely an electron correlation effect. As a consequence, standard wavefunction-based correlation methods such as MP2 or CCSD(T) (described in section 2.2) are the methods of choice for the description of these weakly interacting systems. Their disadvantage is the above mentioned unfavourable formal scaling of $\mathcal{O}(N^5)$ and $\mathcal{O}(N^7)$, respectively, with the system size N, making their use in the study of nanostructures with hundreds of atoms far from feasible.

In general, DFT does incorporate correlation effects. However, long-range dispersion occurs even with vanishing overlap, and even the modern gradient-corrected density functionals fail to account for it.[47–49] With DFT currently being the most promising and widely used method in calculating large molecules and nanostructures, a lot of work has been done to address the shortcomings of current functionals that do not properly account for dispersion.

A straightforward approach for addressing these issues is the addition of an empirical dispersion correction term, initially employed by Ahlrichs *et al.*[50] in the late 1970s to correct Hartree–Fock energies for missing correlation. More than 20 years later, this approach was adopted by Elstner *et al.* for the density-functional tight-binding (DFTB) method, as well as by Wu and Yang, Grimme and many others for DFT.[51–54]

According to the design of Grimme,[53] and as implemented in TURBOMOLE, a dispersion correction to DFT based on damped $-C_6 \cdot R^{-6}$ potentials (DFT-D) is described as follows. An empirical dispersion energy-correction term, E_{disp}, is added to the DFT energy, resulting in the total DFT-D energy expression

$$E_{\text{DFT-D}} = E_{\text{DFT}} + E_{\text{disp}} \tag{2.49}$$

The term E_{disp} has the form

$$E_{\text{disp}} = -s_6 \sum_{i=1}^{N_{\text{a}}-1} \sum_{j=i+1}^{N_{\text{a}}} \frac{C_6^{ij}}{R_{ij}^6} f_{\text{dmp}}(R_{ij}) \tag{2.50}$$

where N_{a} is the number of atoms, C_6^{ij} the vdW coefficient for the interaction between the atoms i and j, and R_{ij} their interatomic distance, s_6 a functional-dependent global scaling factor that was fitted to a test set of vdW complexes, and f_{dmp} a damping function[52–54] of the form

$$f_{\mathrm{dmp}}(R_{ij}) = \frac{1}{1 + \exp[-\alpha(R_{ij}/R^0_{ij} - 1)]} \tag{2.51}$$

where R^0_{ij} is the sum of atomic vdW radii. This damping function approaches zero for small values of R_{ij}, avoiding 'double counting' in the region of covalent bonding distances, and approaches one for large values of R_{ij}, yielding the correct asymptotic behaviour for E_{disp}.

In the first formulation in 2004, the vdW coefficients, C_6^{ij}, were taken as harmonic means of two atomic C_6 coefficients obtained from the work of Wu and Yang,[52] with each atomic C_6 coefficient averaged over all possible hybridisations.[53] The global scaling factor, s_6, was fitted to a test set of 18 vdW complexes for the functionals BLYP, BP86, and PBE, resulting in values of 1.4, 1.3, and 0.7, respectively, using a value of $\alpha = 23$[52] in the damping function. In 2006, Grimme proposed a revised DFT-D approach using new atomic C_6 coefficients, evaluating C_6^{ij} by the geometric mean and applying a less steep damping function with $\alpha = 20$.[55] In this revised approach, the missing atoms of the second period and all atoms of the third through fifth periods were added onto the parameter list. The refitting was done to a larger, more general test set of weakly interacting molecules. The revised s_6 scaling factors for the functionals BLYP, BP86, PBE, TPSS, and B3LYP are 1.2, 1.05, 0.75, 1.0, and 1.05, respectively.

In section 3.1, these two parameter versions of the DFT-D approach shall be tested for their performance and applicability to the systems of interest in the present work.

2.4.2. Spin-component-scaled MP2

The simplest wavefunction-based correlation method considered as a viable alternative to DFT is MP2. As already pointed out in the previous section, MP2 is able to describe dispersion forces in molecular systems, and also has advantages over DFT when charge transfer processes are involved. However, standard MP2 is well known to be inferior to the best density functionals available in the calculation of thermochemistry data such as heats of formation or reaction energies.[44,56–58] Furthermore, standard MP2 shows a tendency to systematically overbind for dispersive π–π interactions and other weakly bound systems when compared to CCSD(T).[53,57,59–61] Thus, enhancements to conventional MP2 methods aiming at increasing the accuracy while maintaining, or even perhaps decreasing, the computational costs are desired.

The total MP2 correlation energy can be partitioned into an opposite-spin (OS) electron pair and same-spin (SS) electron pair contribution

$$E_{\mathrm{MP2}} = E_{\mathrm{MP2}}^{\mathrm{OS}} + E_{\mathrm{MP2}}^{\mathrm{SS}} \tag{2.52}$$

That the two different spin cases behave differently was well-known and, for example, exploited by Klopper in a refined extrapolation scheme towards the complete basis set (CBS) limit.[62] This scheme applies an X^{-3}-type extrapolation to the OS pair energies and an X^{-5}-type extrapolation to the SS pairs, taking into account their different convergence with cardinal number X of the Dunning cc-pVXZ basis sets (cf. section 2.5). Based on these different behaviours, in 2003 Grimme proposed a simple but effective correction to the MP2 scheme that significantly improves the accuracy of the method.[57] The correction is based on a separate scaling of $E_{\mathrm{MP2}}^{\mathrm{OS}}$ and $E_{\mathrm{MP2}}^{\mathrm{SS}}$, and is thus called spin-component-scaled MP2 (SCS-MP2)

$$E_{\mathrm{SCS-MP2}} = p_{\mathrm{OS}} E_{\mathrm{MP2}}^{\mathrm{OS}} + p_{\mathrm{SS}} E_{\mathrm{MP2}}^{\mathrm{SS}} \tag{2.53}$$

The starting scaling coefficients, p_{OS} and p_{SS}, were rationalised by the observation that the opposite-spin pair contribution is underestimated by MP2 ($\sim$ 80–85% of the total correlation energy) in typical molecules, and that the ratio $E_{\mathrm{MP2}}^{\mathrm{OS}}/E_{\mathrm{MP2}}^{\mathrm{SS}}$ is, on average, between three and four. These empirical scaling coefficients were then fitted to a test set of 51 reactions, yielding the values of $p_{\mathrm{OS}} = 6/5$ and $p_{\mathrm{SS}} = 1/3$. Although SCS-MP2 scales as standard MP2 theory, SCS-MP2 has statistically proven to give more accurate reaction energies, heats of formations, atomisation energies, and so forth.[57,58] Furthermore, for molecular geometries and vibrational frequencies, SCS-MP2 outperforms MP2 and shows significant improvements in the description of weakly bound systems that are dominated by dispersion.[63]

A simplified variant of the SCS-MP2 approach involves the scaling of the OS component of the correlation energy while neglecting the SS component. The scaled opposite-spin second order correlation (SOS-MP2) energy then becomes

$$E_{\mathrm{SOS-MP2}} = p_{\mathrm{SOS}} E_{\mathrm{MP2}}^{\mathrm{OS}} \tag{2.54}$$

As expected, a somewhat larger scaling factor (when compared to SCS-MP2) of $p_{\mathrm{SOS}} = 1.3$ is obtained.[64] In the interest of avoiding the calculation of the SS component, Jung *et al.*[64] successfully proposed an SOS-MP2 implementation that is devoid of any fifth-order steps present in conventional MP2 theory. This reduced scaling results in an only slight decrease in accuracy relative to SCS-MP2.[58,64] Thus, with SOS-MP2 at hand, the system sizes subject to calculations can be pushed further.

Note that the present work reports SCS-MP2 values exclusively, since the implementation of SOS-MP2 in the Turbomole version used throughout these studies did not exploit the favourable scaling yet and still scaled as SCS-MP2 ($\mathcal{O}(N^5)$ with system size N).

2.5. Basis sets

Inherent in almost all DFT and wavefunction-based electronic structure methods is the introduction of basis sets. As already pointed out in section 2.2.1 the LCAO approach employs a set of know functions, the AOs χ_α, for expanding the unknown MOs Φ_i (cf. eq. 2.10). Atomic orbitals can be described by Slater functions as known from the hydrogen atom, the Slater type orbitals (STOs). However, in terms of computational efficiency, atom-centred Gaussian type orbitals (GTOs) are preferred to STOs, although the orbital description by GTOs is inferior to STOs and as a rule of thumb one needs three GTOs to represent one STO. The problem with the STOs is that there is no analytic solution of four-centre two-electron integrals over STOs. GTOs in terms of Cartesian coordinates are expressed as

$$\chi^{\text{GTO}}_{\zeta,l_x,l_y,l_z}(x,y,z) = N x^{l_x} y^{l_y} z^{l_z} e^{-\zeta r^2} \tag{2.55}$$

where ζ is the orbital exponent that defines the compactness of the orbital and N a normalisation factor. The sum of l_x, l_y, and l_z determines the type of orbital (*e.g.* $l = l_x + l_y + l_z = 0$ an s-orbital, $l = 1$ a p-orbital, $l = 2$ a d-orbital and so forth). To meet the need of an enlarged set of GTOs for a valid orbital description while limiting the computational costs, contracted basis sets are used. An AO is represented by a *fixed* linear combination (contraction) of k primitive GTOs (PGTOs) that form the contracted GTO (CGTO)

$$\chi^{\text{CGTO}} = \sum_k a_k \chi_k^{\text{PGTO}} \tag{2.56}$$

Minimum basis sets (with only one CGTO per occupied AO) are insufficient for quantitative calculations on molecules. Several enhancements to a minimum basis set (as will be discussed) are necessary to obtain quantitatively correct results.

Basis sets are classified by their *zeta* quality. Doubling all functions of a minimum basis results in a double zeta (DZ) type basis (zeta is used due to the Greek letter ζ in the exponent of the functions). Since the valence electrons have a huge impact on the chemical properties of a molecule, an accurate description of the valence orbitals is the first target to address. Consequently, solely doubling the number of valence orbitals produces a split valence basis (SV), and is also denoted as valence double zeta (VDZ) or double zeta valence (DZV) or simply double zeta (DZ) basis set. To increase the flexibility of the basis set in describing bonds and bond polarisations, higher angular momentum functions (higher than what is occupied in the atomic ground state) are needed. These polarisation functions are indicated with the letter 'P' in most basis sets (*e.g.* DZVP). For correlation methods, the polarisation functions are essential to properly account for the two types of electron correlation, the 'in–out' and 'angular' correlation. Thus, a large basis set (at least triple zeta) is needed to fulfill the requirements of a balanced basis set. As the orbitals in DFT methods serve to reproduce the correct density and not the wave function itself, the basis set requirements for DFT calculation are less demanding.

The following types of basis sets are utilised throughout this work. Preoptimisations of structures (and optimisations of the largest structures) as well as exploratory analysis are performed with the TURBOMOLE split valence polarised basis sets (SV(P), def-SV(P) and def2-SV(P), synonyms for elements of the second period).[65,66] These basis sets contain for elements of the second period (Li–Ne) a (7s4p1d) set of primitive functions that are contracted to a [3s2p1d] set employing a {511/31/1} contraction scheme. For the hydrogen atom, a contraction of (4s)[2s]{31} is used. Thus, only a d-polarisation function is used for *non*-hydrogen atoms, as indicated by the acronym P in brackets.

Quantitative DFT results are calculated with the triple zeta valence plus polarisation (TZVP) series of TURBOMOLE basis sets (TZVP, def-TZVP and def2-TZVP).[66,67] For the hydrogen atom, a (5s1p)[3s1p]{311/1} contraction and for elements of the second period a (11s6p1d)[5s3p1d]{62111/411/1} contraction are utilised in these basis sets. The newest basis set of improved triple zeta quality (def2-TZVP) introduces one further d-function and an f-function for the elements of the second period resulting in a contraction of (11s6p2d1f)[5s3p2d1f]{62111/411/11/1}.

For calculations employing correlation methods, either the TURBOMOLE basis sets of quadruple zeta quality (QZVP, def2-QZVP) or the correlation consistent Dunning basis sets are used.[66,68–71] The term correlation consistent (cc) in the series of polarised valence X-tuple zeta (cc-pVXZ) basis sets refers to the fact that polarisation functions that are equally important for accounting for a certain portion of the correlation energy are added all at the same time. Augmenting the Dunning basis sets with diffuse functions (functions with small exponents) results in the aug-cc-pVXZ series. Diffuse functions are especially important for the description of properties far away from the nucleus, *e.g.* in anions.

Standard basis sets for correlation treatment are routinely optimised for the valence electron correlation employing a frozen core approximation. The frozen core approximation is based on the experience that it is mostly the valence electrons that rule the chemical behaviour of molecules (*e.g.* bond formation). Thus, the correlation of the core-electrons ideally is a constant contribution causing, when one neglects it, a constant error in the absolute energies that cancels out in relative energies. However, if core–valence and core–core correlation shall be accounted for explicitly in a minimal-core or a full all-electron calculation, the standard correlation basis sets perform poorly. In such calculations core–valence (CV) and weighted core–valence (wCV) basis sets are needed that add additional tight functions (large exponent) for describing the core and that are optimised for this special purpose. The core–valence Dunning basis set series aug-cc-pCV*XZ* and aug-cc-pwCV*XZ* are used for minimal-core correlated calculations in the present work.[72,73]

The basis set incompleteness is an error that any calculation performed in a finite basis suffers from. However, with the use of balanced basis sets most of the error should cancel out for relative energies that are evaluated as differences between total energies calculated in the *same* basis. Nevertheless, due to the use of atom-centred basis functions the quality of the basis set is dependent on the geometry of the molecule. This phenomenon introduces errors when, for example, comparing relative energies of different conformers. The error gets especially severe for the calculation of weak interactions, *e.g.* in van der Waals complexes. The basis set for the calculation of the energy of the complex is 'more complete' in terms of available functions than the one used for the individual molecules. Pictorially speaking, one molecule within the complex can use basis functions of the binding partner and *vice versa*. This causes a basis set superposition error (BSSE) in the calculated binding energies. The binding energy of a complex AB is evaluated as

$$\Delta E(\mathrm{AB}) = E(\mathrm{AB})_{ab}^{\mathrm{AB}} - E(\mathrm{A})_{a}^{\mathrm{A}} - E(\mathrm{B})_{b}^{\mathrm{B}} \tag{2.57}$$

where a denotes the basis functions of fragment A and b the basis functions of fragment B. The superscripts AB, A, and B indicate the geometries of the complex and the optimised individual fragments, respectively. An approximation of the BSSE in $\Delta E(\mathrm{AB})$ can be determined by the counterpoise (CP) energy[74]

$$\Delta\mathrm{CP} = E(\mathrm{A})_{ab}^{\mathrm{AB}} + E(\mathrm{B})_{ab}^{\mathrm{AB}} - E(\mathrm{A})_{a}^{\mathrm{AB}} - E(\mathrm{B})_{b}^{\mathrm{AB}} \tag{2.58}$$

where $E(\mathrm{A})_{ab}^{\mathrm{AB}}$ denotes the energy of fragment A calculated in the geometry it has in the complex and employing the full basis set ab (the functions b of fragment B are present as ghost functions), and where $E(\mathrm{A})_{a}^{\mathrm{AB}}$ denotes the energy of fragment A in the same geometry but with only the basis functions a present in the calculation. The same definitions apply to fragment B. The counterpoise-corrected binding energy is then

$$\Delta E^{\mathrm{CP}}(\mathrm{AB}) = \Delta E(\mathrm{AB}) - \Delta\mathrm{CP} \tag{2.59}$$

Due to the aforementioned slower convergence of correlated wave function calculations with basis set size, a BSSE correction of weak interactions evaluated at the correlated level is vital. Nevertheless, also for corresponding DFT calculations with commonly sized basis sets the BSSE can remain substantial for weakly bound systems.

2.6. Potential energy surface

The different methods and approaches discussed thus far in the previous sections determine the total energy of a given molecular geometry. Calculating the energy of all possible nuclear arrangements in a molecule provides the potential energy surface (PES), that is, a multidimensional surface (hypersurface) of the potential energy with respect to all spatial coordinates of the composing atoms. Even with a coarse mapping, the construction of a complete PES is not feasible for larger molecules. However, when investigating molecules in computational chemistry, primarily just selected stationary points on the PES are of particular interest, *i.e.* minima and first order saddle points. The optimisation of a molecular structure in general is the search for these stationary points.

2.6.1. Structure optimisation

The minima mark the stable configurations of a molecule (equilibrium structures) on the molecular PES and are of interest for conformational analysis of a molecule. Herein, the most important structure is the global minimum structure , that is, the molecular structure with the lowest possible potential energy. Minima on the PES are characterised by a vanishing gradient (zero slope) and a Hessian with solely positive eigenvalues. The gradient and the Hessian at a point $\mathbf{x}_c$ on the PES are given by the first and second derivatives of the energy function (defining the PES) with respect to all atomic coordinates

$$\mathbf{g}_c = \nabla f(\mathbf{x}_c) = \begin{bmatrix} \frac{\delta f}{\delta x_1} \\ \vdots \\ \frac{\delta f}{\delta x_n} \end{bmatrix} \tag{2.60}$$

$$\mathbf{H}_c = \nabla^2 f(\mathbf{x}_c) = \begin{bmatrix} \frac{\delta^2 f}{\delta x_1 \delta x_1} & \cdots & \frac{\delta^2 f}{\delta x_1 \delta x_n} \\ \vdots & \ddots & \vdots \\ \frac{\delta^2 f}{\delta x_n \delta x_1} & \cdots & \frac{\delta^2 f}{\delta x_n \delta x_n} \end{bmatrix} \tag{2.61}$$

First order saddle points on the PES characterised by a vanishing gradient and a Hessian with one and only one negative eigenvalue represent molecular transition states (TS). These TS are maxima on the minimum energy paths (MEP) connecting the reactants and the products of chemical reactions and are needed for the calculation of reaction barriers and rates.

For locating minima on a PES, there exist various algorithms and methods ranging from a simple linear model of including only the gradient information into the search (*e.g.* steepest descent, conjugate gradient methods) to the more sophisticated quadratic model that utilises also information about the curvature of the PES by including the Hessian in exact or approximate form (Newton and *quasi*-Newton methods).[22,75] Its the family of second-order *quasi*-Newton–Raphson optimisation methods (with step control by level-shifting, augmented Hessian, and so forth) that makes the search for minima robust and efficient. Finding first order saddle points (TS) is much more difficult as there is no general approach available that warrants success. This will be pointed out in the following section.

2.6.2. Transition state search

The transition state search is far from being routine and it requires a lot of chemical intuition (about how the TS possibly could look like) to successfully locate the first order saddle points. There exist two families of approaches for locating TS.

First, the local methods that propagate the geometry on the basis of local information about the PES, *i.e.* the energy, the local gradient and the Hessian (surface walking procedure) and thus only require the reactant configuration. Unfortunately, these local TS search algorithms need a very good guess structure that lies sufficiently close to the real TS in order to work successfully. An initial 'best guess' for the TS structure can be obtained for example, by constructing a guess energy pathway from the reactants to the products including intermediate structures (chemical intuition, *vide supra*) which are optimised by a constrained minimisation (mimicking the reaction coordinate by freezing some internal coordinates). The maximum energy structure on the guess energy pathway then usually is a good starting structure for the local TS search algorithms.

Second, the interpolation methods that require information about at least two minima (*e.g.* reactants and products) to interpolate the TS between these two endpoints. The nudged elastic band (NEB) method[76,77] and the string method (SM)[78,79] are examples of interpolation methods that are widely used for calculating TS and complete MEPs of chemical reactions. These methods work with a sequence of configurations (nodes or beads) that interpolate between the reactant and product configurations (discrete path). That way, the optimisation problem of finding a saddle point is converted into a minimisation of an object function that describes the discrete path (band, string). The NEB method describes the discrete path by a number of beads that are connected by harmonic springs (elastic band) thus augmenting the 'true' potential of all intermediate structures with the spring energies. In contrast, the string method employs a reparametrisation step after each evolution step to redistribute the nodes along the evolved string. Whereas for both, the NEB and string methods the user needs to provide an initial guess for the reaction pathway (initial band, initial string) the growing string method (GSM) gets along with only two string fragments, *e.g.* the reactant and product configurations, then evolving (*growing*) the string from its endpoints.[79] Due to the optimisation of an initial guess pathway, the number of energy calculations increases with the number of nodes along the path. Furthermore, most interpolation methods require a force calculation at each node of the path each time the path moves. Thus, the computational costs per iteration for the interpolation methods are severely larger than for the surface walking methods that mostly require only a single energy and force calculation per iteration. The surface walking method and the growing string method that are utilised for the TS searches with TURBOMOLE in the present work are discussed below in more detail.

The surface walking procedure

The local surface walking method in the TURBOMOLE module STATPT performs a trust region image minimisation (TRIM) to locate the TS.[80,81] An 'image' surface is generated by defining a function whose gradient and Hessian at each point are identical to the real surface except for a sign change in the lowest eigenmode. This definition makes the first order saddle points of the original function coincide with the minima of the image function. Thus, the TS search on the real surface can be performed as a minimisation on the 'image' surface that will automatically maximise the energy along the selected Hessian eigenvector (transition vector) while minimising the energy for all the others.

An exact initial Hessian has to be calculated for the guess structure (*vide supra*) while an updated Hessian is used within the iterations. Nevertheless, further exact Hessian calculations (defined in the optimisation setup or by a manual restart) are most likely necessary to successfully locate the TS. For a good guess structure, there exists only one Hessian eigenvector with a negative eigenvalue (imaginary vibrational frequency) that will be followed during the TS optimisation. Most conveniently, this eigenvector is verified by graphically visualising the corresponding vibrational mode that has to resemble, at least in parts, the assumed reaction coordinate.

The growing string method

The growing string method is a variant of the SM where two separate strings are evolved independently towards the TS until they meet. The united string is then moved towards the MEP analogously to the SM. The starting string fragments are associated with the reactant and product configurations but do not necessarily have to be minima on the PES. While a prescribed parametrisation density, σ, evolves, the string $\varphi(\sigma)$ (a discrete path) grows from each end.

The string in the SM, and the united string in the GSM, is normalised so that $\varphi(0)$ is the reactant and $\varphi(1)$ the product configurations. Since the string consists of a discrete number of intermediate configurations, the nodes, there act normal forces $f^{\perp}$ at each node pulling the string towards the MEP. Simultaneously minimising these forces at all the nodes results in the MEP ($f^{\perp}(\varphi_{\mathrm{MEP}}) = 0$). The minimisation problem is solved iteratively. Each iteration consists of an evolution step that moves the string closer to the MEP and a subsequent reparametrisation step to recover the prescribed parametrisation density, σ (redistribution of nodes along the string).

The growing string method, as other interpolation methods in general, are preferably used for unimolecular systems possessing several low frequency modes and bimolecular reactions where the local methods perform poorly. The GSM in particular is suited for cases where good initial guess pathways (needed for the string and NEB methods) are unavailable due to a poor agreement of linearly interpolated pathways or a breakdown of pathways generated by chemical intuition (exceptional, unknown chemical systems). Alternatively, the method can also be used in an approximate manner (less rigid convergence criteria and fewer nodes along the string) to generate an initial best guess structure for a subsequent surface walking run.

2.7. Software

This section gives a short overview of the computer programs and software packages used in the different quantum chemical calculations throughout this work. A description of the computational details with references to all methods and basis sets shall then be given in the individual sections of chapter 3.

All DFT calculations were carried out with the program package TURBOMOLE, applying standard basis sets that come along with the distribution.[19,20] TURBOMOLE was also used for the MP2 and SCS-MP2 calculations. The CCSD(T) calculations were performed with the MOLPRO quantum chemistry package.[82] Preparation, manipulation, and visualisation of molecular coordinate files were achieved with the ECCE builder,[83] MOLDEN,[84] and VMD[85] programs.

3. Applications – A Walk through Nanoscience

3.1. Benchmarking DFT-D with model systems

When describing weak interactions of small molecules with carbon based nanostructures such as fullerenes or carbon nanotubes, there is an urgent need for cost-efficient computational methods. The DFT-D method, which includes an empirical dispersion correction (introduced in section 2.4.1) that addresses the fact that standard DFT neglects this contribution, is suited for this task. Testing the reliability of the DFT-D method with additional wavefunction-based calculations is essential, but the size of the carbon nanostructures under consideration in this study is too large for this benchmarking. Thus, the need for reasonable and appropriate model systems that will represent such nanostructures arises. For example, a benzene molecule is considered as the minimal molecular building unit of a carbon nanotube or fullerene. The coronene molecule ($C_{24}H_{12}$) is yet another more extended building unit of large carbon nanostructures. Some relevant interacting systems of benzene and coronene, such as benzene–Ne, benzene–CH_4, benzene–NH_3, benzene–H_2O, and coronene–H_2O are already included in the test set for the DFT-D parametrisations of Grimme.[53,55]

In the following section, the performance assessment of DFT-D is complemented with studies of models that are structurally and chemically related to the interaction of small primary alcohols with carbon nanotubes, as examined later in section 3.2.2. Thus, a benchmark test for the interaction of methanol (MeOH) with the molecules benzene and coronene is performed by comparing DFT-D with the wavefunction-based correlation method SCS-MP2 (introduced in section 2.4.2). The results for the latter are, in turn, compared to CCSD(T) for the smaller benzene–MeOH test system.

The computational details are as follows. Potential energy surface scans for methanol approaching a benzene and a coronene molecule are performed with DFT-D in the parametrisation of Grimme from 2004, using the functionals BP86,[32,35–37] BLYP,[35,38] and PBE.[33,39] A TZVP basis set and the corresponding auxiliary basis for the resolution-of-the-identity (RI) approximation are applied.[46,86–88] For the functionals BP86 and PBE, these scans are accomplished with conventional DFT for comparison. Multiple integration grids, with gridsize m3 for the benzene model and gridsize m4 for the coronene model, are used along with the default SCF convergence criterion of $10^{-6}\,E_h$. Final convergence criteria of the structure optimisations are set to $10^{-4}\,E_h/a_0$ for the Cartesian gradient norm and $10^{-6}\,E_h$ for the energy change. To ensure a well-defined rectangular approach towards the centre of the π system (X), the oxygen$\cdots$ring-centre distance (R_{OX}) together with an angle and a dihedral angle are frozen, while all other degrees of freedom are optimised. The PES is evaluated for $R_{\mathrm{OX}} = 220 - 600$ pm in steps of 20 pm, then for $R_{\mathrm{OX}} = 600 - 800$ pm in steps of 50 pm. The DFT and DFT-D equilibrium distances, R_{OX}, and binding energies, D_{e}, are calculated for the individual functionals, including the oxygen$\cdots$ring-centre coordinate in the optimisation while keeping the rectangular approach. Furthermore, these values are recalculated employing the revised DFT-D parameters from 2006 with the functionals BP86, BLYP, PBE, TPSS,[33,40] and B3LYP[35,38,44,45] to compare the performance of the two approaches. The results of the revised DFT-D approach will be indicated in the text as DFT-D*. The MP2 and SCS-MP2 potential curves are calculated with the TURBOMOLE module RIMP2 by means of single-point energy calculations at the BP86-D/TZVP geometries.[89] A QZVP basis set with corresponding auxiliary basis is applied.[68,90,91] The MP2 and SCS-MP2 equilibrium R_{OX} and D_{e} values are determined from these curves. The SCS-MP2 calculations are performed with the default scale factors of $p_{\mathrm{OS}} = 6/5$ and $p_{\mathrm{SS}} = 1/3$. In the case of benzene–methanol, the CCSD(T) binding energy is evaluated for the BP86-D/TZVP equilibrium geometry using the correlation-consistent triple-zeta basis set of Dunning (cc-pVTZ).[69,92,93] The potential energy curves and all binding energies D_{e} are corrected for BSSE by applying the function counterpoise technique including fragment relaxation.[74,94]

3.1.1. Interaction of methanol with benzene

The equilibrium geometries of the perpendicular approach of MeOH to the ring centre of benzene, using conventional DFT without dispersion correction and DFT-D, are shown for the functional BP86 in Fig. 3.1. The potential curves of the PES scans calculated at the DFT, DFT-D, MP2, and SCS-MP2 levels of theory are plotted in Fig. 3.2. As can be seen in the equilibrium geometries in Fig. 3.1, the influence of dispersion on the structure of benzene–MeOH is significant and cannot be neglected. The BP86/TZVP R_{OX} distance is 355 pm—much too long compared to BP86-D/TZVP (335 pm). In the BP86/TZVP structure, the OH bond of MeOH points down and is perpendicular to the ring plane, causing the CO bond to be somewhat tilted with respect to the plane. In the BP86-D/TZVP

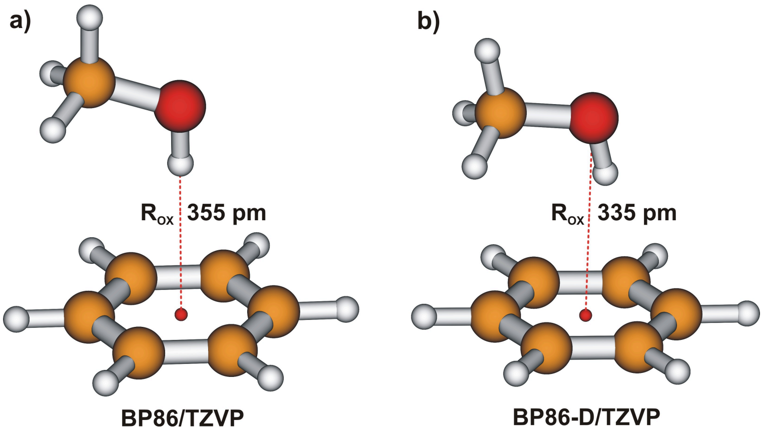

Figure 3.1. Equilibrium geometries of the perpendicular approach of MeOH to the centre X of a benzene ring. a) conventional DFT, BP86/TZVP b) DFT-D including empirical dispersion correction, BP86-D/TZVP.

structure, however, the CO bond lies in a plane parallel to the ring plane, rotating the OH bond away from the OX connecting line by about 14°. These structural findings can be explained by two different forces present in the system. Neglecting dispersion in the computational method, the system is only weakly bound by $-3.3\,\mathrm{kJ\,mol^{-1}}$ at the BP86/TZVP level due to electrostatic interactions. The OH distance is elongated by 0.3 pm with respect to the free MeOH molecule, indicating that the π–σ^*_{OH} interaction weakens the OH bond. This electrostatic interaction, the only one of the two forces present, is captured at the conventional DFT level and explains the observed perpendicular orientation of the OH bond with respect to the ring plane. D_e increases to $-14.8\,\mathrm{kJ\,mol^{-1}}$, accounting for the attractive dispersion interaction with BP86-D/TZVP. It is mainly the dispersive attraction between the CH_3 group and the benzene ring that is responsible for this enhanced binding, as well as for the rotation of the OH bond off the perpendicular orientation. This rotation of the OH bond, in turn weakens the electrostatic interaction. The structure of benzene–MeOH reported by Pribble *et al.*[95] at the B3LYP/6-31+G* level is similar to the BP86/TZVP structure of the present work and also suffers from lack of dispersion. The binding energy, D_e, increases to $-8.7\,\mathrm{kJ\,mol^{-1}}$ when the PBE functional is employed with conventional DFT. Since the PBE functional, by definition, cannot account for long-range dispersion, the stronger binding compared to BP86 must be attributed to fortuitous error cancellation. The PBE-D implementation corrects for this unphysical extra binding by scaling down ($s_6 < 1$) in turn the empirical dispersion correction contribution (cf. BP86 and BLYP values of $D_\mathrm{e}^{\mathrm{disp}}$ with the corresponding PBE value in Table 3.1).

Table 3.1. Optimised equilibrium distances R_{OX} and binding energies D_{e} for the test model benzene–MeOH using DFT, DFT-D, MP2, SCS-MP2, and CCSD(T).

	R_{OX} /pm	D_{e} /kJ mol^{-1}	$D_{\mathrm{e}}^{\mathrm{uncorr}\ a}$ /kJ mol^{-1}	$D_{\mathrm{e}}^{\mathrm{disp}\ b}$ /kJ mol^{-1}
BP86/TZVP	355	−3.3	−5.4	
PBE/TZVP	343	−8.7	−11.3	
BP86-D/TZVP	335	−14.8	−17.6	−14.6
BLYP-D/TZVP	342	−13.5	−16.5	−14.3
PBE-D/TZVP	338	−15.0	−17.9	−7.4
MP2/QZVP//BP86-D/TZVP	$\sim 320^{c}$	−18.6	−21.0	
SCS-MP2/QZVP//BP86-D/TZVP	$\sim 340^{c}$	−13.8	−15.7	
CCSD(T)/cc-pVTZ//BP86-D/TZVP	-	−13.5	−19.1	

[a] BSSE uncorrected binding energies

[b] Dispersion contribution to the binding energy evaluated according to eq. 2.50

[c] Equilibrium distances derived from the potential curves

In the framework of DFT-D, all tested functionals agree to within 1.5 kJ mol^{-1} in the equilibrium region, with the binding energies ranging from −13.5 to −15.0 kJ mol^{-1}. The DFT-D potential curves (cf. Fig. 3.2) coincide within a wide range of R_{OX} but are quite shallow around the minimum. This causes R_{OX} to be a very soft binding parameter, resulting in equilibrium distances that range from 335 pm for BP86-D to 342 pm for BLYP-D. The PBE-D potential curve shows two peculiar features: a kink at around 440–480 pm and a jump at 500 pm. These can be explained by the intersection of two diabatic potential curves along the R_{OX} coordinate in this region. Whereas optimisations with BP86-D and BLYP-D give the diabatic curves with the global minimum at 330–340 pm, the optimisations with PBE-D follows an adiabatic path wherein the MeOH molecule rotates and the CH_3 group tilts down as the R_{OX} value is increased (440–480 pm). The jump at 500 pm is due to the optimisation switching back to the aforementioned diabatic curve. The difficulties in the optimisation with PBE-D around 440–480 pm have no influence on the equilibrium distance and binding energy, however. The MP2/QZVP potential curve and the equilibrium values of $R_{\mathrm{OX}} = 320$ pm and $D_{\mathrm{e}} = -18.6$ kJ mol^{-1} confirm the expected overbinding of MP2 (already mentioned in section 2.4.2) for such weakly interacting systems.

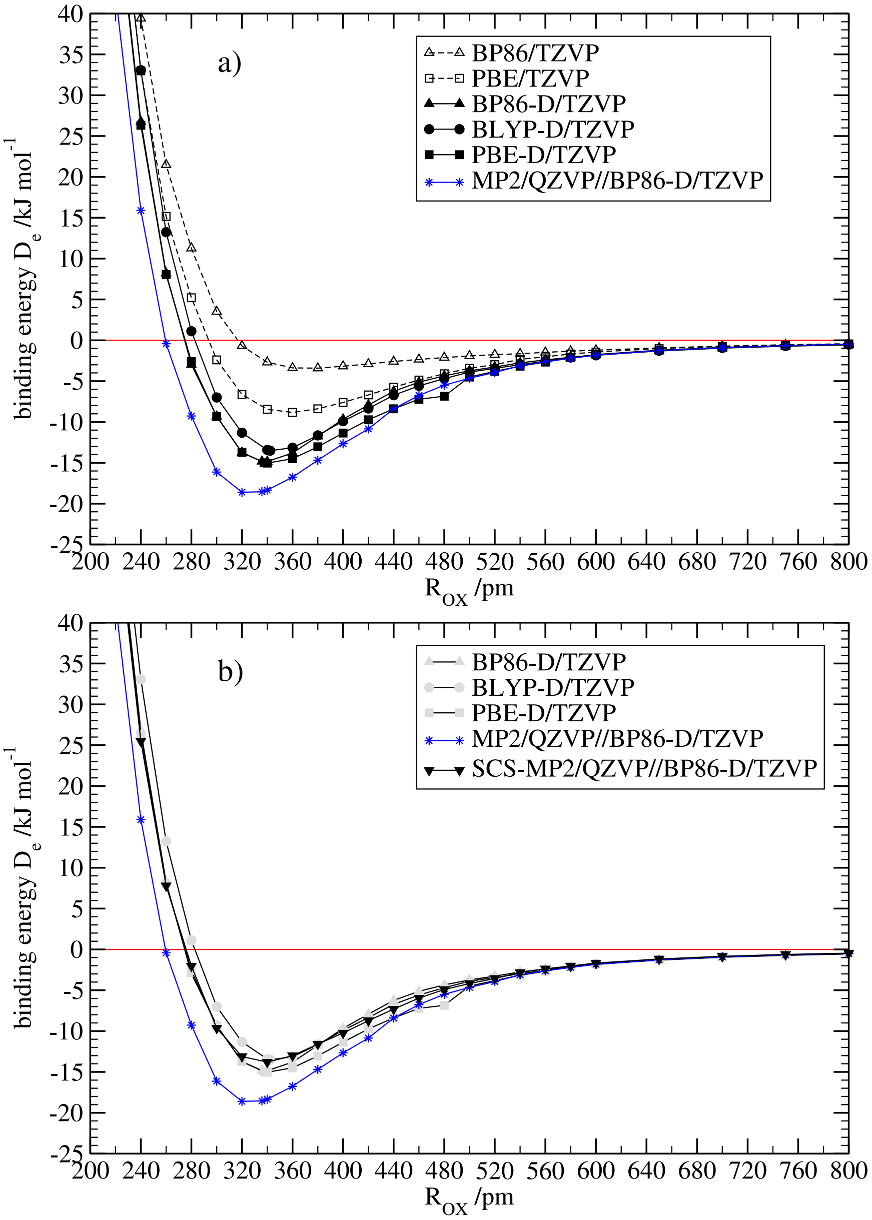

Figure 3.2. Potential energy curves of the perpendicular approach of MeOH to the ring centre X of benzene. a) BP86-D, BLYP-D, and PBE-D curves are compared to conventional BP86 and PBE curves without dispersion correction as well as to MP2 results. b) SCS-MP2 results compared to standard MP2 and DFT-D curves (formerly filled black symbols are shown in grey).

For comparable systems like benzene–NH_3 or coronene–NH_3, Bauschlicher and Ricca derived a scaling factor from CCSD(T) calculations of 0.83 to correct their MP2 energies.[61] In the present work, SCS-MP2 calculations are performed to improve on the MP2 results. At the SCS-MP2 level, the binding energy decreases by $4.8\,\mathrm{kJ\,mol^{-1}}$ to $-13.8\,\mathrm{kJ\,mol^{-1}}$, with an equilibrium R_{OX} value of 340 pm that is elongated when compared to that of standard MP2. The D_{e} and R_{OX} values for the model system, benzene–MeOH, using different levels of theory are summarised in Table 3.1. The SCS-MP2 potential curve shown in Fig. 3.2b coincides very well with the DFT-D curves, especially matching the BP86-D potential curve. For further verification, the CCSD(T) binding energy of the equilibrium geometry (BP86-D/TZVP) has been calculated and shown to confirm the SCS-MP2 value to within $0.3\,\mathrm{kJ\,mol^{-1}}$. From these findings, two conclusions are drawn. First, the good agreement of the DFT-D results with SCS-MP2 is promising, especially since DFT-D is a cost-efficient method that is suited for the target systems. This first conclusion will be further affirmed by the larger test system in the following section (*vide infra*). Secondly, SCS-MP2 has shown to be a valuable tool for further investigations, since it allows one to compare the DFT-D results with an accurate wavefunction-based *ab initio* method. This comparison shall be applied in relevant cases throughout this work.

Investigating the revised DFT-D approach of 2006 (DFT-D*) for benzene–MeOH with the functionals BP86, BLYP, PBE, TPSS, and B3LYP, an overestimation of the binding energy is observed for all functionals. Moreover, the newly added *meta*-GGA functional TPSS and the hybrid functional B3LYP overbind by up to $7\,\mathrm{kJ\,mol^{-1}}$ when compared to CCSD(T). All functionals consequently result in much too short R_{OX} values ($\sim$ 15–20 pm too short compared to SCS-MP2).

Table 3.2. Optimised equilibrium distances R_{OX} and binding energies D_{e} for the test model benzene–MeOH, applying the revised DFT-D approach (labelled as DFT-D*).

	R_{OX} /pm	D_{e} /$\mathrm{kJ\,mol^{-1}}$
BP86-D*/TZVP	319	−18.7
BLYP-D*/TZVP	325	−17.8
PBE-D*/TZVP	322	−19.9
TPSS-D*/TZVP	320	−20.3
B3LYP-D*/TZVP	323	−19.2

These results are summarised in Table 3.2. It can also be seen from Figure 2 in Ref. 55 that for the systems benzene–NH_3 and benzene–H_2O in the test set, the revised DFT-D approach overestimates the binding energies by up to 8 kJ mol^{-1} (benzene–H_2O). This trend shall be further addressed in the following section.

3.1.2. Interaction of methanol with coronene

The DFT-D, MP2, and SCS-MP2 potential energy curves for the perpendicular approach of MeOH to the centre of a coronene molecule are plotted in Fig. 3.3. For DFT-D, the PES along the R_{OX} coordinate shows a local minimum at about 480 pm, with the equilibrium at 330–340 pm depending on the functional. Contrary to benzene–MeOH, the optimisations for all tested DFT-D functionals give the adiabatic potential curve along the R_{OX} coordinate. In the local minimum structure of coronene–MeOH at 480 pm, the CH_3 group is pointing down towards the ring centre, as shown in the geometry inset in Fig. 3.3. The equilibrium structures of benzene–MeOH and coronene–MeOH are very similar. However, in coronene–MeOH, the carbon of the CH_3 group has moved closer to the ring plane compared to the oxygen atom, consequently rotating the OH

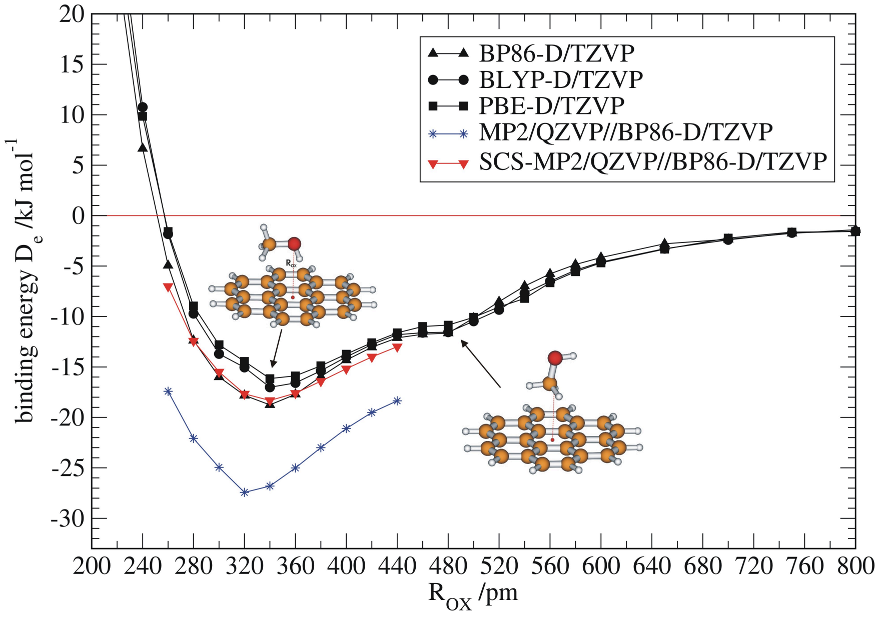

Figure 3.3. Potential energy curves of the perpendicular approach of MeOH to the centre X of coronene. BP86-D, BLYP-D, and PBE-D potential curves are compared to MP2 and SCS-MP2 results. The local minimum found at R_{OX} ~ 480 pm corresponds to a structure in which the CH_3 group is pointing down towards the coronene, as shown in the figure.

bond 20° away from the OX connecting line. The binding energy is increased by about 1 kJ mol^{-1} for PBE-D and up to 4 kJ mol^{-1} for BP86-D when compared to benzene–MeOH. This is in accord with a shortening of the equilibrium R_{OX} distances by about 1–3 pm. The electrostatic interaction is increased due to an enhanced quadrupole moment in coronene compared to benzene, but the main contribution to the observed stronger binding and the shortened R_{OX} distances originate from dispersion (cf. D_{e} and $D_{\mathrm{e}}^{\mathrm{disp}}$ values in Tables 3.1 and 3.3). In coronene–MeOH, additional dispersive interaction arises from the carbon atoms formally surrounding a 'benzene core'. Regarding the potential curves, MP2 again overestimates the binding energy and overbinds by about 9 kJ mol^{-1} in the equilibrium ($R_{\mathrm{OX}} = 320$ pm), whereas the DFT-D and SCS-MP2 curves coincide nicely. The PBE-D and BLYP-D curves are still off by about 1–2 kJ mol^{-1} in the equilibrium region, while the BP86-D/TZVP curve agrees very well with the SCS-MP2 curve. The R_{OX} and D_{e} values for all methods employed are summarised in Table 3.3.

Table 3.3. Optimised equilibrium distances R_{OX} and binding energies D_{e} for the test model coronene–MeOH using DFT-D are compared with MP2 and SCS-MP2 results.

	R_{OX} /pm	D_{e} /kJ mol^{-1}	$D_{\mathrm{e}}^{\mathrm{uncorr}\ a}$ /kJ mol^{-1}	$D_{\mathrm{e}}^{\mathrm{disp}\ b}$ /kJ mol^{-1}
BP86-D/TZVP	332	−18.7	−23.1	−26.3
BLYP-D/TZVP	339	−17.0	−21.3	−25.7
PBE-D/TZVP	337	−16.0	−20.3	−12.8
MP2/QZVP//BP86-D/TZVP	∼ 320^{c}	−27.4	−31.4	
SCS-MP2/QZVP//BP86-D/TZVP	∼ 330^{c}	−18.3	−21.9	

[a] BSSE uncorrected binding energies
[b] Dispersion contribution to the binding energy evaluated according to eq. 2.50
[c] Equilibrium distances derived from the potential curves

Applying the revised DFT-D approach, it was observed that the trends for coronene–MeOH are very similar to the trends for benzene–MeOH in the previous section. It can be seen from Table 3.4 that all functionals overbind by up to 8 kJ mol^{-1}, resulting in equilibrium distances, R_{OX}, that are much too short (∼ 10 pm too short compared to SCS-MP2). This overbinding is reminiscent of what is observed for MP2. Similarly, Grimme *et al.* reported an overbinding for the interaction of H_2O and NH_3 with corannulene at the revised DFT-D level.[96] They attribute this finding to a general problem with DFT, that is, its tendency to overestimate charge transfer contributions. The first DFT-D parametrisation works amazingly well for benzene–MeOH, as shown in the previous section, and has also given convincing results for the test set members benzene–H_2O and benzene–NH_3, presumably by compensating for the overbinding with the parametrisation. The DFT-D approach in the 2004 parametrisation obtains results of SCS-MP2 quality also for the larger test system, coronene–MeOH, and shall therefore be employed in further applications. Because of the especially good agreement of BP86-D/TZVP with SCS-MP2 for both tested systems, BP86 will be the functional of choice for the succeeding investigations.

Table 3.4. Optimised equilibrium distances R_{OX} and binding energies D_e for the test model coronene–MeOH, applying the revised DFT-D approach (labelled as DFT-D*).

	R_{OX} /pm	D_e /kJ mol^{-1}
BP86-D*/TZVP	316	-24.9
BLYP-D*/TZVP	322	-23.9
PBE-D*/TZVP	321	-23.4
TPSS-D*/TZVP	316	-26.0
B3LYP-D*/TZVP	322	-24.9

3.2. Single-walled carbon nanotubes

The science of carbon nanotubes (CNTs) started with the discovery of multiwalled tubes (MWCNTs) in 1991 by Iijima and the synthesis of single-walled carbon nanotubes (SWCNTs) two years later.[2,97–99] Since then, carbon nanotubes have been inspiring an interdisciplinary research community of physicists, chemists, biologists, pharmacists, material scientists, and engineers due to their outstanding functional mechanical, electrical, and optoelectronic properties.[4,100–102] SWCNTs are hollow cylinders formally built from a graphene sheet that is rolled up to form a tube. Consequently, the microscopic structure of CNTs is closely related to graphene, and the tubes are labeled in terms of the graphene lattice vectors. Depending on the manner in which the graphene sheet is rolled up, various SWCNTs, uniquely defined by their chiral vectors, $\mathbf{C_h}$, can be obtained as illustrated in Fig. 3.4. The chiral vector, $\mathbf{C_h}$, is defined by multiples of the graphene lattice vectors, $\mathbf{a}_1$ and $\mathbf{a}_2$,

$$\mathbf{C_h} = n\mathbf{a}_1 + m\mathbf{a}_2 \equiv (n, m) \tag{3.1}$$

with a pair of integers, (n, m), termed as chiral index. The direction of the chiral vector is defined by the angle between $\mathbf{a}_1$ and $\mathbf{C_h}$, that is, the chiral angle Θ. Chiral angles from 0° to $+30°$ give rise to right-handed tubes, whereas tubes with chiral angles from 0° to $-30°$ are left-handed. Zigzag $(n, 0)$ SWCNTs with a chiral angle of $\Theta = 0°$ and armchair (n, n) SWCNTs with a chiral angle of $\Theta = 30°$ possess a reflection plane and therefore are achiral. The chiral index, (n, m), of a carbon nanotube determines not only its geometrical properties, *e.g.* the diameter, but also its electronic properties, such as the band structure. Employing a simple zone-folding (ZF) scheme for graphene, that is, imposing confinements due to boundary conditions around the nanotube circumference, the electronic band structure of SWCNTs can be calculated by Hückel-type or tight-binding (TB) models. Within the ZF approximation, (n, m) SWCNTs are metallic when $(n - m)/3$ is an integer, and are semiconducting otherwise. The band gap of the semiconducting (n, m) SWCNTs depends inversely on the tube diameter. For small-diameter tubes ($< 0.7\,\text{nm}$), the '$(n - m)/3$ metallic/semiconducting' rule breaks down. The reason for this is the neglect of the tubes' curvature in the ZF approximation for the graphene stripes. This nonzero curvature gives rise to a mixing of π and σ states that are strictly perpendicular in graphene. The mixing, and thus the influence on the electronic properties, increases with decreasing diameter of the tubes. When the curvature effects are included in the electronic Hamiltonian of the model, the SWCNTs that are '*metallic*' in Hückel theory can be placed in two categories: the truly metallic armchair (n, n) SWCNTs, and the quasimetallic SWCNTs with small, but nonzero band gaps.[103–106]

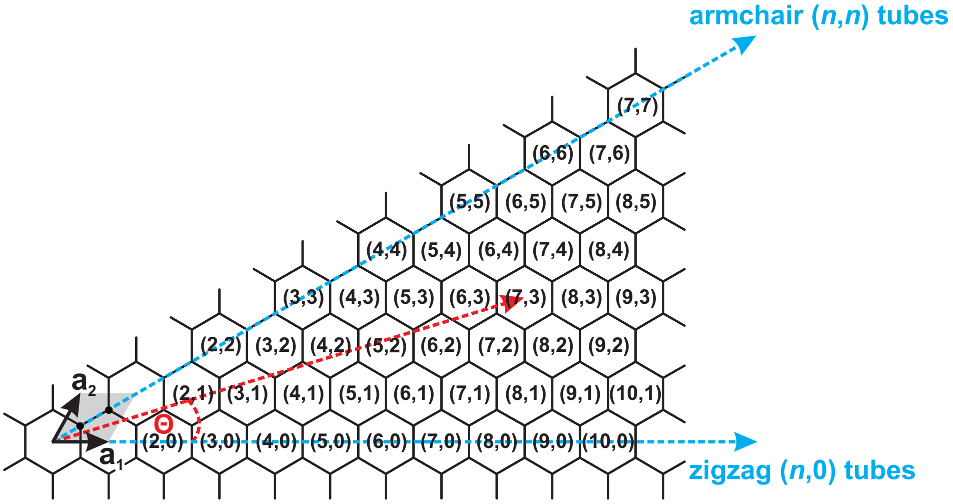

Figure 3.4. SWCNT vector map for right-handed tubes. The unit cell of graphene (highlighted in gray) is spanned by the two primitive lattice vectors $\mathbf{a}_1$ and $\mathbf{a}_2$ and contains two carbon atoms (marked as black dots). Armchair SWCNTs are defined by chiral vectors, $\mathbf{C_h}$, along the (n, n) direction (as indicated in blue) with a chiral angle of $\Theta = 30°$. Zigzag SWCNTs are defined by $\mathbf{C_h}$ along the $(n, 0)$ direction with $\Theta = 0°$. As an example, $\mathbf{C_h}$ of the chiral (7,3) SWCNT, as well as the chiral angle, Θ are given (in red).

In electronic structure calculations of CNTs, two different routes are followed. The first approach employs calculations under periodic boundary conditions, exploiting the quasi-one dimensionality of the tubes and the translational periodicity along the tube axis. The second is a cluster approach, working with finite tube sections to model the CNT. Cutting the tubes into finite sections introduces an additional confinement of the electrons along the tube axis that influences their electronic structure.[107–109] Therefore, a representative cluster must be carefully selected, and any property derived from this finite model must prove its portability to the SWCNT.

When computationally working with finite models of SWCNTs one encounters some problems and peculiarities for the zigzag tubes concerning spin states, frontier orbitals and their location, as well as energy gaps. Some of them have already been reported in the literature,[107,109,110] others are just noted in passing by without further investigation and by applying workarounds.[111,112] Therefore, in section 3.2.1, the electronic properties of finite zigzag $(n, 0)$ SWCNTs are investigated in terms of orbitals, orbital localisation, orbital energies, spin states, and energy gaps. An extrapolation scheme for $(n, 0)$ SWCNT band gaps, using the energy gaps of the finite tube sections with increasing length, shall be presented. Although more detailed works report on the electronic properties, band gaps, and reactivities of finite armchair SWCNTs,[108,113–115] the band gaps in tube sections of an armchair example shall be discussed in section 3.2.1 since this type of SWCNT will later be used in the computational study in section 3.2.2. Within the CNT research, the interaction of small molecules, such as H_2, CH_4, O_2, NH_3, NO_2, SO_2, H_2O, and so forth with SWCNTs is a subfield of considerable interest.[6,61,116–124] This scientific interest has, apart from others, two main foci. Firstly, CNTs are considered as promising materials for gas storage, particularly for the storage of hydrogen.[116–119] Secondly, SWCNTs reveal a high sensitivity towards gaseous molecules, some of which have a large impact on the electronic properties of the tubes. This suggests an application of SWCNTs as chemical sensors.[6,121–124]

More recently, several studies focusing on the adsorption of hydrocarbons and alcohols on CNTs have been conducted.[125–129] Someya *et al.* reported, for example, a significant change ($\sim 50\%$) in the drain current of a carbon nanotube based field-effect transistor (SWCNT-FET) upon exposure to methanol and ethanol (EtOH) vapours.[126] Furthermore, CNTs can be used as novel supports in liquid fuel cells. Since methanol based fuel cells are currently the most promising type of fuel cells,[130] detailed knowledge of the CNT–alcohol interaction is needed. The investigation of the preferred adsorption sites—exohedral (on the outer side of the tube) or endohedral (inside the tube)—is crucial. Moreover, the nature of the interactions must also be investigated and quantified. Reliable intermolecular potentials are essential, *e.g.* for simulations. The Fourier transform infrared (FTIR) spectroscopy study on the adsorption of MeOH and EtOH on SWCNTs by Ellison *et al.*[127] and the thermal desorption spectroscopy (TDS) experiments of Burghaus *et al.*[128,129] provide evidence for the preference for the endohedral adsorption site, as well verification that the interaction is due to physisorption.

In section 3.2.2, the interaction of methanol and ethanol with SWCNTs shall be investigated in detail, employing the DFT-D approach that was benchmarked especially for this purpose; recall that the DFT-D approach yielded accurate results of SCS-MP2 quality in section 3.1. The preference for different adsorption sites (as mentioned in the previous paragraph) will be addressed by calculating the exohedral and endohedral interaction energies of both methanol and ethanol with SWCNTs of various diameters.

3.2.1. Electronic properties of finite SWCNTs

Band gaps in SWCNTs are normally derived from simple ZF predictions or TB and DFT calculations with periodic boundary conditions. In this section, a procedure for obtaining the band gaps in zigzag SWCNTs of various diameters from finite tube sections (H-terminated) employing a cluster approach is presented. A detailed analysis of the effects on the electronic properties of the zigzag tubes due to the cutting is conducted, with a special focus on frontier orbitals. To investigate the spatial position of the orbitals, as well as the orbital energies and the corresponding band gaps of the zigzag SWCNTs, the (7,0), (10,0), and (13,0) tubes as representatives of semiconducting CNTs in comparison with the 'metallic' (by means of Hückel theory) (9,0) tube are chosen. To model the infinite tubes in the cluster approach, various tube sections of each member ranging from $x = 3$ to 20 benzene-ring units along the tube axis are examined, covering a length range from 0.64 to 4.29 nm. Dangling bonds at the tube ends are saturated with hydrogen atoms (H-termination). Finite (4,4) tube sections up to 3.0 nm length ($x = 1$–12) are chosen as representative of the metallic armchair SWCNTs (in the infinite case) and actual band gaps are determined with respect to the tube length.

The computational details are as follows. The structures of all tube models are fully optimised at the DFT level employing the BP86 functional with an SV(P) basis set.[65] The DFT calculations are performed using spin-unrestricted Kohn–Sham (UKS) theory, utilising Fermi smearing with fractional occupation numbers in frontier orbitals in the course of the SCF iterations. A multiple integration grid with gridsize m4 is used. Final convergence criteria of the structure optimisations are set to $10^{-4}\,E_h/a_0$ for the Cartesian gradient norm and $10^{-6}\,E_h$ for the energy change. Having achieved convergence with this approach, the occupation numbers are set to integer values and a subsequent SCF run (convergence criterion $10^{-6}\,E_h$) is conducted for the final solution. The same procedure is applied to all (7,0) and (10,0) tube models using the GGA functional PBE and the *meta*-GGA functional TPSS in order to investigate the functional dependence of the results. The basis set dependence is studied by additionally using the larger TZVP[67] basis together with BP86 for the full sets of (10,0) and (9,0) tube models. Without imposing symmetry restrictions on the short finite SWCNTs (optimisation in C_1), the equilibrium geometries of the zigzag tube sections with an odd number of benzene units along the tube axis have $D_{n\mathrm{h}}$ symmetry, while the zigzag tube sections with an even number possess $D_{n\mathrm{d}}$ symmetry, where $n = 7, 9, 10$, and 13 for the (7,0), (9,0), (10,0), and (13,0) tubes, respectively. The equilibrium geometries of the armchair (4,4) tube sections with only an even or only an odd number of benzene units along the tube axis have $D_{4\mathrm{d}}$ symmetry, while armchair sections with an even–odd alternating number of benzene rings possess $D_{4\mathrm{h}}$ symmetry. Consequently, the optimisations of the longer tube sections are carried out using these symmetries. The calculations described thus far are carried out utilising the multipole-accelerated resolution-of-the-identity (MARI-J) technique, employing appropriate auxiliary basis sets.[86–88,131] Note that it is essential to exploit high symmetry and to use the MARI-J approximation to keep the computational costs manageable for the large tubes. For the large diameter (13,0) tube, the longest and fully optimised tube model is comprised of as many as 572 atoms. To compare with Ref. 111, the H-terminated (9,0) SWCNT model with $x = 5$ and the corresponding closed tube model are additionally optimised at the B3LYP/SV(P) level of theory. This closed tube section is capped with two C_{60} fullerene hemispheres, resulting in D_{3h} symmetry for the overall structure.

The convergence of the SCF procedure gets more and more demanding with increasing length of the H-terminated zigzag tube sections. There are numerous near-degenerate frontier orbitals whose occupation is not clear *a priori*. This shall be illustrated in the following with the example of a H-terminated finite (7,0) SWCNT of 1.07 nm length ($x = 5$). Starting from the orbitals of an extended Hückel calculation, careful convergence with strong damping and with repeatedly changing the orbital occupation numbers to fill emergent holes in the occupation leads to the converged closed-shell solution shown in Fig. 3.5a. Two doubly degenerate e representations, $20e'_3$ and $18e''_3$, arise that are equal in energy. One e-orbital acts as HOMO, the other as LUMO, giving rise to a zero HOMO–LUMO gap in this closed-shell singlet solution. Rearranging the electrons to a high-spin UKS calculation leads to a quintet state that is stabilised by 73.8 kJ mol^{-1} with respect to the singlet state (BP86/SV(P)). The relative energy changes for the frontier orbitals of the quintet state with respect to the singlet state are indicated in Fig. 3.5b. A HOMO–LUMO gap of 0.45 eV is found in the quintet state.

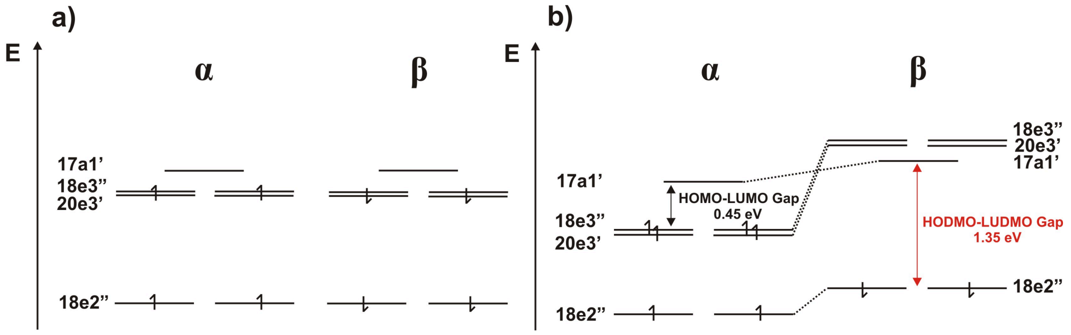

Figure 3.5. Energy diagram of frontier orbitals of the (7,0) SWCNT section, $x = 5$, 1.07 nm, D_{7h}: a) singlet b) quintet (both UKS calculations). The quintet state is stabilised by 73.8 kJ mol^{-1} at the BP86/SV(P) level of theory. The HOMO–LUMO and HODMO–LUDMO gaps are indicated for the quintet state.

The HOMO–LUMO gaps for the complete (7,0) SWCNT series ($x = 3$–20) calculated with the functionals BP86, PBE, and TPSS are plotted against the tube length, denoted by the curves with open symbols in Fig. 3.6. The HOMO–LUMO gap decays to zero rather quickly with increasing tube length for the functionals BP86 and PBE. Also the values calculated with TPSS drop below 0.1 eV for the longer tubes. The calculated HOMO–LUMO gaps of the finite tube sections clearly do not converge to the band gap of the infinite (7,0) SWCNT, which shows a moderate finite band gap and thus is a semiconductor. The frontier orbitals plotted for the (7,0) SWCNT section ($x = 5$) in Fig. 3.7 confirm the findings of Bulusheva *et al.* that localised frontier orbitals that arise at the ends of H-terminated zigzag SWCNTs 'have little to do' with the electronic structure of infinitely long tubes.[107] (These authors used semiempirical methods to investigate the electronic structure of zigzag nanotubes.) As can be seen in Fig. 3.7, the HOMOs $\alpha 20e'_3$ and $\alpha 18e''_3$ and the corresponding unoccupied β orbitals are localised at the tube ends. They have the most orbital contributions from C-atoms that are terminated by hydrogen. In contrast, the next lower-lying orbitals $\alpha 18e''_2$ and the LUMO $\beta 17a'_1$ are delocalised over the entire tube. Thus, to determine energy gaps in the H-terminated tube sections that are related to the band gap of the infinite tube, the highest occupied delocalised MO (HODMO)

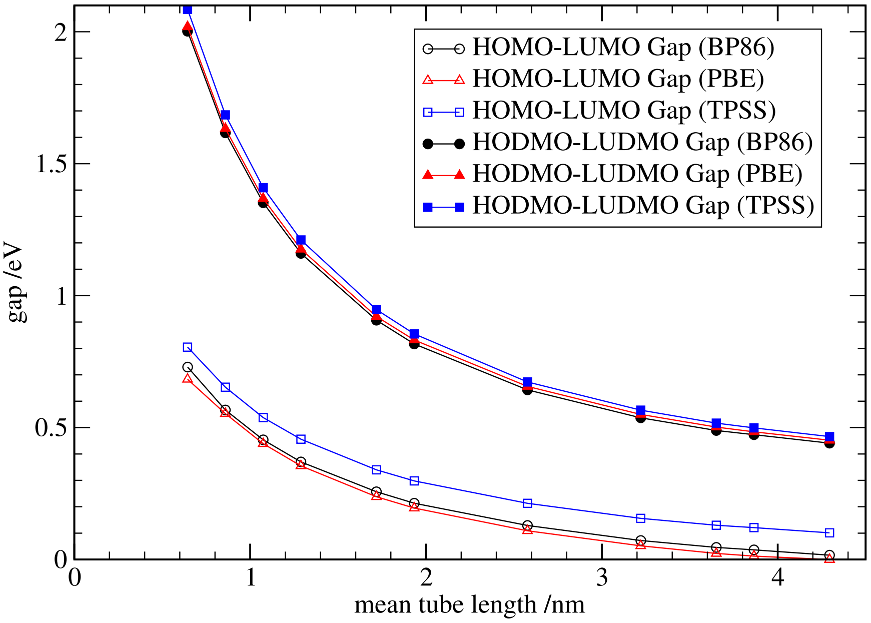

Figure 3.6. HOMO–LUMO and HODMO–LUDMO gaps in (7,0) SWCNT sections (0.64–4.29 nm) calculated with the functionals BP86, PBE, and TPSS in an SV(P) basis. Note that there is almost no functional effect on the HODMO–LUDMO gap.

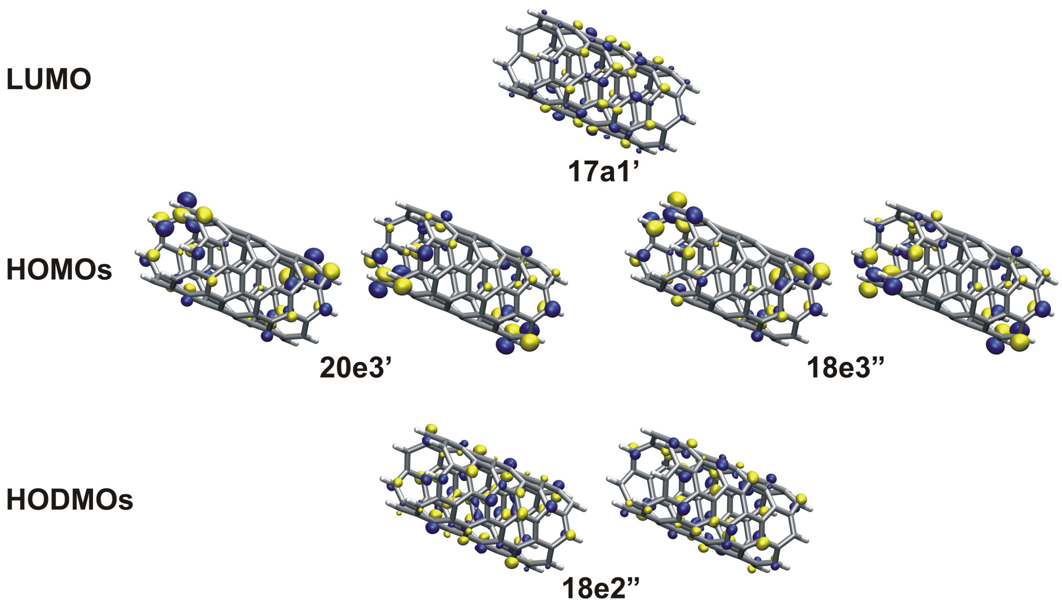

Figure 3.7. Frontier orbitals of the (7,0) SWCNT section, $x = 5$, 1.07 nm, D_{7h} at the BP86/SV(P) level of theory. The highest occupied molecular orbitals (HOMOs), which are localised at the ends of the tube, and the highest occupied delocalised molecular orbitals (HODMOs), which are delocalised over the entire tube, are plotted. The lowest unoccupied molecular orbital (LUMO) is also shown. Note that in this case the LUMO is delocalised over the tube and therefore is also the LUDMO.

can be defined together with the lowest unoccupied delocalised MO (LUDMO). HODMO–LUDMO gaps can then be calculated for the different tube sections and are plotted against the tube length in Fig. 3.6 (filled symbols). Extrapolation to the infinitely long tube leads to a HODMO–LUDMO gap of 0.4 to 0.5 eV for the (7,0) SWCNT, with very good agreement among the functionals tested. Note that in the example of the (7,0) tube section with $x = 5$, the LUDMO is also the lowest unoccupied orbital. This energetic order changes with increasing section length as well as with larger diameters. The *localised* unoccupied orbitals decrease in energy and consequently lie below the LUDMO when exceeding a certain tube diameter or length.

Frontier orbitals are calculated also for the finite (9,0), (10,0), and (13,0) SWCNT series. By orbital inspection and sorting into localised and delocalised orbitals, HODMO–LUDMO gaps are determined. The extrapolated band gaps for these SWCNTs are summarised in Table 3.5. The method yields reasonable band gaps in the range of 0.5–1.0 eV for the semiconducting tubes. The extrapolated band gap of 0.9–1.0 eV for the (10,0) SWCNT is consistent with the experimental value of 1.1 eV[132] as well as calculated band gap values of 0.76 eV (PBE) and

Table 3.5. Band gaps (eV) of the infinite (7,0), (10,0), and (13,0) SWCNT, extrapolated from HODMO–LUDMO gaps by consecutive elongation of the calculated sections.

	band gap (calc.)	band gap (exptl.)
(7,0) SWCNT	0.4–0.5[a]	
(9,0) SWCNT	~ 0.2[b]	
(10,0) SWCNT	0.9–1.0[a,b]	1.1[c]
(13,0) SWCNT	0.8–0.9[d]	

[a] BP86/SV(P), PBE/SV(P), and TPSS/SV(P) agree within 0.1 eV; no functional dependence

[b] BP86/SV(P) and BP86/TZVP coincide; no basis set dependence

[c] experimental value, Reference 132

[d] BP86/SV(P)

0.96 eV (HSE) by Barone *et al.*, who used periodic boundary conditions for their calculations.[133] Only a small basis set effect is found for the HODMO–LUDMO gaps and the extrapolated band gaps. Applying the extrapolation to the metallic (9,0) SWCNT (by means of Hückel theory) yields a small finite band gap of approximately 0.2 eV. This result is in agreement with small but nonzero band gaps reported by Sun *et al.* for small-diameter zigzag tubes that should be metallic according to Hückel theory.[134]

Yumura *et al.* in their work compared HOMO–LUMO gaps in H-terminated (9,0) tube sections with gaps in the corresponding [60]fullerene capped species at the B3LYP/6-31G* level of theory.[111] These authors reported a fast decay of the gap in the H-terminated sections with increasing section length, whereas the gap in the capped sections was an order of magnitude larger and decreasing much slower with the section length. Repeating these calculations for a H-terminated (9,0) tube section ($x = 5$) and for the corresponding capped tube at a similar level of theory (B3LYP/SV(P)), the following is observed: A HOMO–LUMO gap of 1.51 eV is found in the capped tube section. This gap is between orbitals that are delocalised over the entire tube, including the caps. A high-spin calculation for the H-terminated section (quintet state) and subsequently identifying the delocalised frontier orbitals yields virtually the same value for the HODMO–LUDMO gap (1.56 eV). In the singlet state (not the ground state, *vide supra*) the same H-terminated tube reveals a very small HOMO–LUMO gap of 0.25 eV, which is the value Yumura *et al.* reported. As shown above for the (7,0) tube sections, this small HOMO–LUMO gap corresponds to the gap between orbitals that are localised at the ends of the tube. The near degeneracy of these orbitals increases with the section length, resulting in an apparently fast decay of the HOMO–LUMO gap.

The number of orbitals that are localised at the zigzag tube ends increases with increasing diameter of the SWCNTs. As the diameter of the calculated finite SWCNTs increases from 0.57 to 0.80 nm, and then to 1.02 nm in the (7,0), (10,0), and (13,0) tubes, the number of localised orbitals rises from four to six and then eight, resulting in a quintet state for the (7,0) and (9,0) sections, a septet for the (10,0) sections, and up to a nonet for the (13,0) tube sections (cf. Table 3.6). Due to the $D_{n\mathrm{h}}$ symmetry of tube sections with odd x and the $D_{n\mathrm{d}}$ symmetry of those with even x, there exists either a mirror plane perpendicular to the tube axis or an inversion point in the tube centre. Consequently, each orbital (in this symmetry) localised at the tube ends has contributions from *both* ends. Boys localisation is used for these orbitals to obtain MOs that are localised only at one end of the tube. Flipping the spins and calculating the symmetry-broken singlet for the (7,0) tube sections with $x = 4$ and 5, a vanishing interaction between the spins at opposite tube ends is observed. For the (7,0) section with $x = 4$, the symmetry-broken singlet is 3.4 kJ mol^{-1} lower in energy than the quintet. This energy difference reduces to 2.1 kJ mol^{-1} for the section with $x = 5$. According to these calculations, the results of a high-spin calculation using symmetry are equivalent to the broken-symmetry results. Therefore, the high-spin calculation using symmetry will be favoured from a computational point of view in succeeding computations, whenever zigzag finite SWCNTs as well as graphene sheet models with zigzag ends are investigated.

Table 3.6. Diameter-dependence of the number of local spin-orbitals at the tube ends of H-terminated finite zigzag SWCNTs and resulting high-spin states.

	diameter /nm	local spin-orbitals	high-spin state
(7,0) SWCNT	0.57	4	quintet
(9,0) SWCNT	0.72	4	quintet
(10,0) SWCNT	0.80	6	septet
(13,0) SWCNT	1.02	8	nonet

The ground state of finite armchair SWCNTs is the singlet state. Frontier orbitals of these tubes are delocalised and energy gaps of the tube sections can be derived directly from the energy difference of the HOMO and LUMO orbitals. HOMO–LUMO gaps of finite (4,4) armchair SWCNTs are shown with respect to the section length (0.24–2.97 nm) in Fig. 3.8. An oscillation pattern of the HOMO–LUMO gaps is found for the armchair sections with increasing tube length, as reported in many other studies.[108,109,113,115] Based on a Clar valence bond model, the tube sections fall into three different classes of chemical structures. Matsuo *et al.* first referred to these three different classes as tube sections belonging to Kekulé, incomplete Clar, and complete Clar (fully benzenoid) networks.[113] The authors reported for the (5,5) tube sections the largest HOMO–LUMO gap for the Kekulé structure and the smallest gap for the next complete Clar network within the same period. The change of the calculated HOMO–LUMO gaps within (4,4) tube sections of one class, either Kekulé, incomplete Clar, or complete Clar network, is illustrated in Fig. 3.8. Whereas the HOMO–LUMO gaps in the sections with a complete Clar network stay constant (within 0.1 eV) over a wide length range (the gap has to drop to zero in the limit of infinite length), the gaps in sections with an incomplete Clar

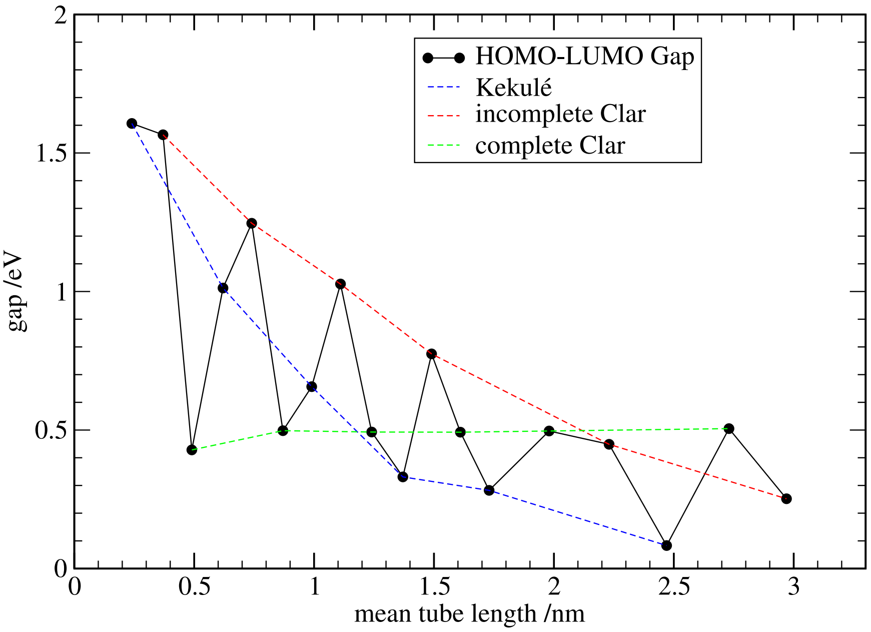

Figure 3.8. HOMO–LUMO gaps in armchair (4,4) SWCNT sections (0.24 to 2.97 nm) calculated at the BP86/TZVP//BP86/SV(P) level. HOMO–LUMO gaps within one class, either Kekulé (blue), incomplete Clar (red), or complete Clar (green) networks are categorised by dashed lines.

network or Kekulé structure decrease monotonically with increasing tube length. The decay for sections with a Kekulé structure is considerably faster than for the sections with an incomplete Clar network. Consequently, the HOMO–LUMO gaps in the Kekulé structures are only larger than in the complete Clar networks for the short tubes. For the longer tube sections ($\geq 1.4\,\text{nm}$), the gap in the Kekulé structures drops below the value for the complete Clar networks.

In summary, when defining cluster models of SWCNTs, special care has to be taken such that the finite tube sections are valid representatives of the infinite tubes. In the case of the zigzag SWCNTs, diligent attention must be given to the local orbitals that are artificially introduced by the finite model. Any intermolecular interaction has to be studied far enough away from these orbitals to avoid fringe effects and model artefacts. In the case of the armchair SWCNTs, the electronic structure of the finite models correlates with the electronic structure of the corresponding infinite nanotube only for some cluster lengths. Thus, any property studied with cluster models has to be tested for its dependency on the type of model (length, electronic structure, *etc.*).

3.2.2. Interaction of small primary alcohols with SWCNTs

The exohedral and endohedral interactions of both MeOH and EtOH with SWCNTs of various diameters are investigated within a cluster approach, employing DFT-D. The diameter-dependence of the interaction energies is determined for various H-terminated finite armchair SWCNTs, with diameters ranging from 0.5 nm for the smallest tube to 1.6 nm for the largest. This interaction at different sites of the tube is illustrated for the example of finite (8,8) SWCNTs, with a diameter of about 1.1 nm in Fig. 3.9. Graphene can be considered the limiting case with respect to the diameter, wherein the exo- and endohedral interactions coalesce due to the zero-curvature. Thus, the interaction of MeOH and EtOH with different graphene models is also investigated. The infinitely long armchair (n, n) SWCNTs are metallic, while the zigzag (7,0) SWCNT, for example, is a semiconductor (as discussed in section 3.2.1), with a diameter that is very similar to the (4,4) SWCNT. The influence of the electronic properties on the adsorption energies is examined for the example of the exohedral interaction of MeOH with these two different tube types. In attempt to investigate the effect of the chosen section length on the electronic properties of the tube (as discussed in the previous section), different finite tube models are tested in the cluster approach. Special care is taken to ensure the convergence of the results with respect to the section length. The suitability of smaller models in describing the interaction is examined by considering coronene models of varying curvatures,

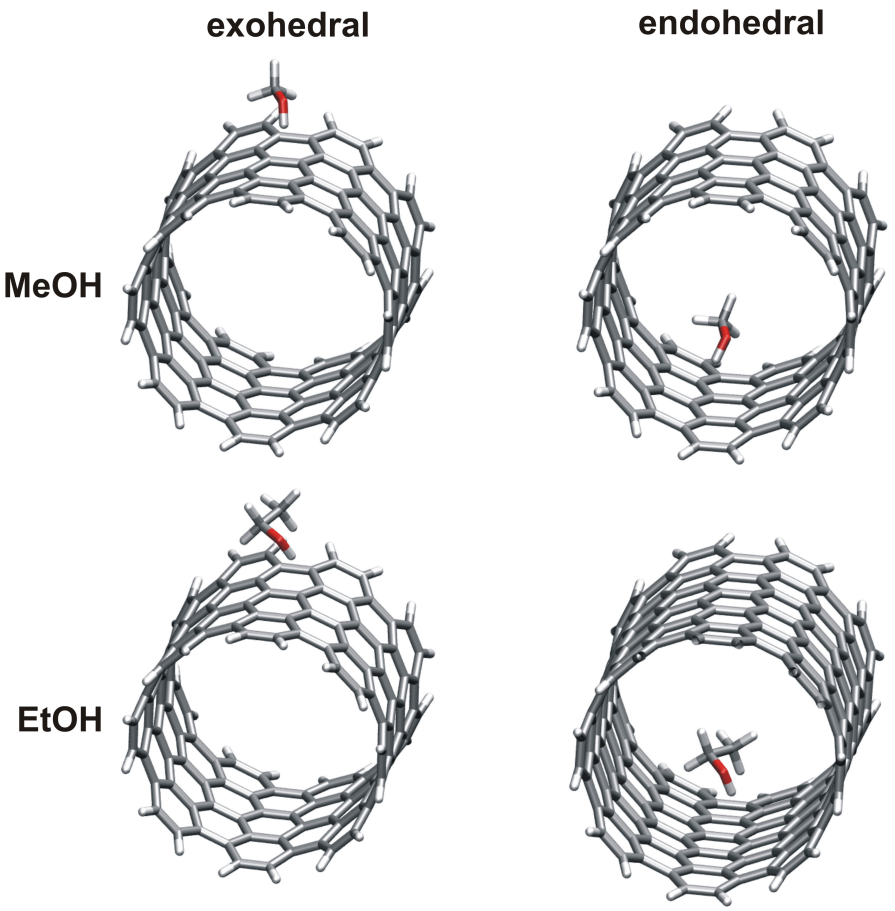

Figure 3.9. Interaction of the primary alcohols, MeOH and EtOH, with the outer (exohedral) and the inner (endohedral) surface of the finite armchair (8,8) SWCNTs. The diameter of the tubes is 1.08 nm.

designed to mimic the different curvatures of the tubes (cf. Fig. 3.10). For the coronene–MeOH subsections, a comparison of the DFT-D results with SCS-MP2 shall be performed for further verification of the DFT-D method (benchmark).

The computational details are as follows. All geometries of MeOH and EtOH interacting with finite SWCNTs of various diameters and lengths are optimised at the BP86-D/TZVP level of theory. A multiple integration grid with gridsize m4 is used, along with an SCF convergence criterion of $10^{-6}\,E_h$ for the structure optimisations. The final convergence criteria are $10^{-4}\,E_h/a_0$ for the Cartesian gradient norm and $10^{-6}\,E_h$ for the energy change. A perpendicular approach of the alcohol molecules to a 6-ring centre (X) in the middle of the tube sections (see Figs. 3.9 and 3.10) is used, similar to the benzene and coronene models described in the benchmark section (see section 3.1). Final total energies used in

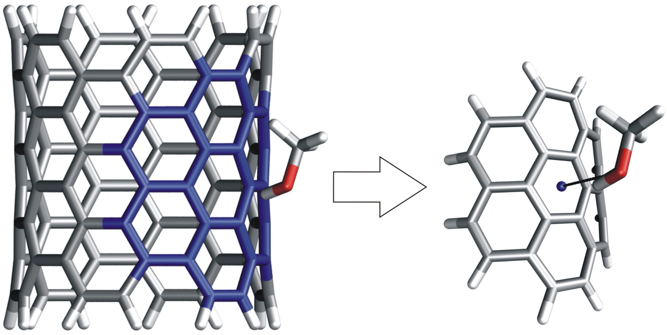

Figure 3.10. A model coronene–MeOH subsection is cut from the equilibrium structure of MeOH interacting with a finite armchair SWCNT. The dangling bonds are saturated with hydrogen atoms with a C–H distance of 110 pm (along the former C–C bonds).

the calculation of interaction energies are evaluated at the same level of theory, but employing a very fine integration grid (gridsize 7). This is done to minimise the statistical error that results from the orientation of the tubes within the grid (cf. section 2.3.2), and becomes especially important for the large diameter SWCNTs with increasing number of atoms (*e.g.* the largest tube calculated has 290 atoms).

First, the influence of the tube length is investigated with different finite (4,4) and (7,0) SWCNTs for the exohedral interaction and different finite (5,5) SWCNTs for the endohedral interaction. The model tube sections range from three to 7 benzene units along the tube axis ($x = 3 - 7$). Then, the exohedral MeOH interaction with the finite (4,4), (5,5), (6,6), (8,8), and (10,10) SWCNTs, as well as the exohedral EtOH interaction with the finite (4,4), (8,8), and (10,10) SWCNTs, are all calculated with tube sections of length $x = 3$. The endohedral MeOH and EtOH interactions are investigated for the finite (4,4), (5,5), (6,6), (7,7), (8,8), and (10,10) SWCNTs. Additionally, for MeOH the large (12,12) tube ($d = 1.62\,\text{nm}$) is tested. For the endohedral MeOH interactions, finite sections of $x = 3$ are found to be sufficient, whereas 5 benzene units along the tube axis ($x = 5$) are needed to obtain converged results for the endohedral EtOH interactions. The interaction with graphene, the limit of an infinite-diameter tube, is calculated for MeOH with two graphene sheet models comprising 66 and 112 carbon atoms, respectively. In both models, boundary carbon atoms are saturated with hydrogens (see Fig. 3.11). The larger graphene model is chosen in such a way that no zigzag ends arise. As a consequence local orbitals and the calculation of high-spin states encountered in the previous section are avoided. For EtOH, the interaction is calculated with the coronene molecule and the smaller of the graphene models. All these geometries are optimised at the BP86-D/TZVP

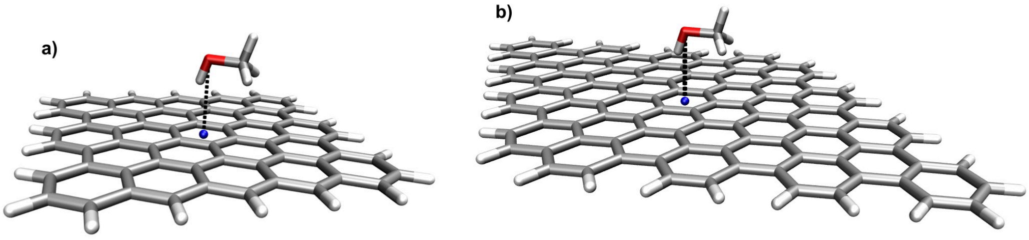

Figure 3.11. MeOH molecule interacting with graphene, modelling an infinite-diameter tube (zero-curvature). a) model with 66 C atoms, H-terminated b) model with 112 C atoms, H-terminated, no zigzag ends.

level, applying the same structural confinement as described for the finite tubes. For the study of smaller models, coronene–MeOH subsections are cut from each equilibrium geometry of the armchair tube–MeOH structures. Then, the dangling bonds are saturated with hydrogen atoms placed along the former C–C bonds at a distance of 110 pm (shown in Fig. 3.10), followed by single-point energy calculations at the BP86-D/TZVP and SCS-MP2/QZVP levels of theory. All binding energies are corrected for BSSE by applying the function counterpoise technique including fragment relaxation.[74,94]

The binding energies, D_e, and R_{OX} distances for the exohedral MeOH and EtOH interaction with finite armchair (4,4) tube sections of different lengths (3, 4, 5, and 7) are summarised in Table 3.7. Tube sections are chosen from all three classes: Kekulé, incomplete Clar network, and complete Clar network, according to the classification presented in section 3.2.1. Comparing the tube section with $x = 4$ (Kekulé type) to the next longer tube section with $x = 5$ (complete Clar type), the section type is found to have no effect on the binding energy or the R_{OX} distance. The same holds true for the shorter section with $x = 3$ that has an incomplete Clar network. Whereas the Kekulé type and the subsequent Clar type sections represent extremes in the oscillations of HOMO–LUMO gaps and reaction energies,[115] *vide supra*, this is not observed for the weak and mainly dispersive interaction of SWCNT–alcohol. The section length is found to have only little effect on the interaction, weakening the binding consistently by $<1\,\mathrm{kJ\,mol^{-1}}$ without any oscillations when going from three to seven benzene units along the tube axis. Thereby, the R_{OX} distance is hardly affected. These results lead one to conclude that the tube–alcohol interaction is mainly of local character. Similar results are obtained for the endohedral interaction examined with finite (5,5) tube sections (cf. Table 3.7). Also for this interaction, no oscillations in the binding energies are observed. In contrast to the exohedral interaction, the binding energies for the endohedral interaction

Table 3.7. Dependence of D_e and R_{OX} on the section length of the finite SWCNTs. This is tested for the exohedral interaction of MeOH, EtOH with armchair (4,4) SWCNT sections ($x = 3, 4, 5, 7$ benzene units along the tube axis) and zigzag (7,0) SWCNT sections ($x = 4, 5, 7$). The endohedral interaction is assessed with (5,5) SWCNT sections ($x = 3, 5, 7$). All values are obtained with BP86-D/TZVP.

	MeOH		EtOH	
x	D_e /kJ mol^{-1}	R_{OX} /pm	D_e /kJ mol^{-1}	R_{OX} /pm
	(4,4) SWCNT (exohedral)			
3	−15.1	328	−20.6	319
4	−14.8	328	−20.6	320
5	−14.7	327	−20.3	320
7	−14.2	329	−20.4	318
	(7,0) SWCNT (exohedral)			
4	−14.1	344		
5	−13.7	344		
7	−13.9	341		
	(5,5) SWCNT (endohedral)			
3	−51.4	345 (322^a)	−15.3	414 (267^a)
5	−55.1	345 (326^a)	−23.6	414 (268^a)
7	−54.8	345 (326^a)	−25.7	415 (268^a)

^{a} distance to CC bond above the 6-ring centre X

increase with the tube length. For MeOH a short tube section with $x = 3$ captures more than 90% of the interaction energy of the infinite tube, but for the larger EtOH molecule, a tube section with at least $x = 5$ is needed to obtain converged results.

The binding energy D_e of $-14\,\mathrm{kJ\,mol^{-1}}$ computed for the zigzag (7,0) tube sections is within $1\,\mathrm{kJ\,mol^{-1}}$ of the corresponding binding energy of the armchair (4,4) tube sections with comparable diameter. In contrast, the equilibrium R_{OX} values of 341 to 344 pm found in the zigzag (7,0) tubes are by 12 to 16 pm longer than that of the armchair (4,4) tubes. There is almost no variation in the binding energies with increasing section length of the zigzag tubes and the equilibrium R_{OX} values agree to within 3 pm. Two conclusions can be drawn from these results. First, the zigzag tube model is chosen to be sufficiently large, to avoid edge effects due to the localised orbitals at the ends of this tube type (cf. section 3.2.1). In accordance with the results for the (4,4) tube models, a section with $x = 4$ is sufficient to describe the full interaction. Second, the weak interaction of alcohols (MeOH and EtOH) with finite SWCNTs is influenced by geometrical effects (the diameter), but is independent of the tube type (armchair or zigzag). In summary, the convergence of the model with respect to the tube length is achieved for the exohedral interaction of both alcohols and the endohedral interaction of MeOH with sections of $x = 3$–4. Tube sections of length $x = 5$ are only necessary for describing the endohedral interaction of EtOH. Alternative exohedral approaches of the alcohols to the tubes, *i.e.* to a CC bond instead of to a ring centre, yield virtually the same energies (within $1\,\mathrm{kJ\,mol^{-1}}$).

The binding energies, D_{e}, and the equilibrium distances, R_{OX}, for the exohedral approach of MeOH and EtOH to the armchair tube sections ($x = 3$) with various diameters (0.53–1.35 nm) are summarised in Table 3.8. Equilibrium geometries of varying tube curvatures and diameters are shown for SWCNT–MeOH, as an example, in the first panel of Fig. 3.12. An increase of D_{e} by 2.4–$2.5\,\mathrm{kJ\,mol^{-1}}$ for both MeOH and EtOH is observed, going from the small diameter (4,4) SWCNT ($d = 0.53\,\mathrm{nm}$) with a binding energy of -15.0 $(-20.6)\,\mathrm{kJ\,mol^{-1}}$ for MeOH (EtOH), to the larger diameter (10,10) SWCNT ($d = 1.35\,\mathrm{nm}$) with D_{e} of -17.4 $(-23.1)\,\mathrm{kJ\,mol^{-1}}$. Considering the zero-curvature of graphene as the limit of an infinite-diameter tube, the increase of the binding energy with the tube diameter continues until a threshold value of -19.6 to -20.0 $(-27.5)\,\mathrm{kJ\,mol^{-1}}$ (depending on the graphene model) is reached for D_{e}. As the binding energy increases, the equilibrium R_{OX} distance elongates by 3–4 pm from 328 (319) pm in the (4,4) SWCNT to 332 (322) pm in graphene. The described changes for the exohedral EtOH interaction with increasing diameters of the tubes are virtually the same as for MeOH, but the binding energy is about 1.4 times larger than that of MeOH. In turn, the equilibrium distances R_{OX} found in SWCNT–EtOH are 9–10 pm shorter than the ones found in SWCNT–MeOH. This observed stronger exohedral binding of EtOH (in comparison to MeOH) with the finite SWCNTs is due to additional dispersive forces, arising from the longer carbon chain in EtOH that interacts with the tube's wall.

The curved coronene–MeOH subsections that are cut from the SWCNT–MeOH structures in order to model the interaction are shown in the second panel of Fig. 3.12. The binding energies evaluated with these smaller models are given in Table 3.9.

Table 3.8. Binding energies D_e and equilibrium distances R_OX for the exohedral interaction of MeOH and EtOH with finite armchair SWCNTs of various diameters at the BP86-D/TZVP level of theory (sections with $x = 3$, perpendicular approach). The limiting case of zero-curvature is modelled by a coronene molecule and two graphene models.

	MeOH		EtOH	
tube	D_e /kJ mol^{-1}	R_OX /pm	D_e /kJ mol^{-1}	R_OX /pm
(4,4) SWCNT	−15.0	328	−20.6	319
(5,5) SWCNT	−15.6	329	–	–
(6,6) SWCNT	−16.0	329	–	–
(8,8) SWCNT	−16.8	330	−22.5	320
(10,10) SWCNT	−17.4	330	−23.1	320
coronene	−18.7	332	−24.5	328
graphene[a]	−19.6	331	−27.5	322
graphene[b]	−20.0	332	–	–

[a] graphene model with 66 carbon atoms, shown in Fig. 3.11a

[b] graphene model with 112 carbon atoms, shown in Fig. 3.11b

The curved coronene–MeOH subsections capture >90% of the SWCNT–MeOH interaction. Whereas the largest deviations arise for the border cases of the narrow diameter tubes and the graphene layer in the range of 1.3 to 1.5 kJ mol^{-1}, the deviation for the medium to larger diameter tubes is negligible. Utilising the model of a curved coronene–MeOH to mimic the tube–MeOH interaction, a dipole moment is introduced artificially due to the cutting and saturating of the dangling bonds with hydrogen atoms. Furthermore, the quadrupole moments are affected by the cutting. These perturbations become evident in the plots of the energy contributions in Fig. 3.13. Whereas the curves of the dispersive contribution to the binding energy for the full tube and the coronene model are roughly parallel with a difference of 1–2 kJ mol^{-1}, the curves of the full interaction intersect with one another. In conclusion, the coronene–MeOH model is only appropriate when the contribution of these dipole and quadrupole

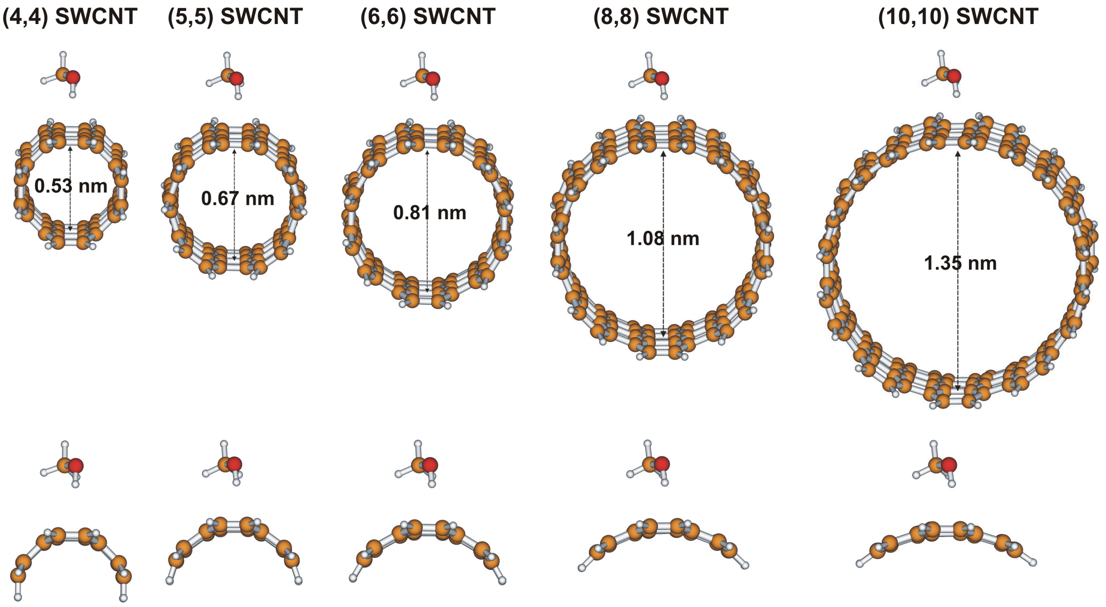

Figure 3.12. Equilibrium geometries of the exohedral interaction of MeOH with finite armchair SWCNTs of various diameters at the BP86-D/TZVP level of theory (sections with $x = 3$, perpendicular approach). The corresponding coronene–MeOH subsections are shown to illustrate the change in the curvature of the coronene model.

Table 3.9. Binding energies D_e (kJ mol^{-1}) for the exohedral MeOH interaction evaluated with a curved coronene model. The coronene–MeOH subsections are taken from each equilibrium geometry of the different SWCNTs (cf. Figs. 3.10 and 3.12) and single-point energy calculations are performed with BP86-D/TZVP. For comparison, SCS-MP2/QZVP values are also given.

	MeOH	
subsection of	D_e (BP86-D)	D_e (SCS-MP2)
(4,4) SWCNT	−13.5	−13.5
(5,5) SWCNT	−14.4	−14.3
(6,6) SWCNT	−15.4	−15.5
(8,8) SWCNT	−16.7	−16.8
(10,10) SWCNT	−17.6	−17.5
coronene	−18.7	−18.3

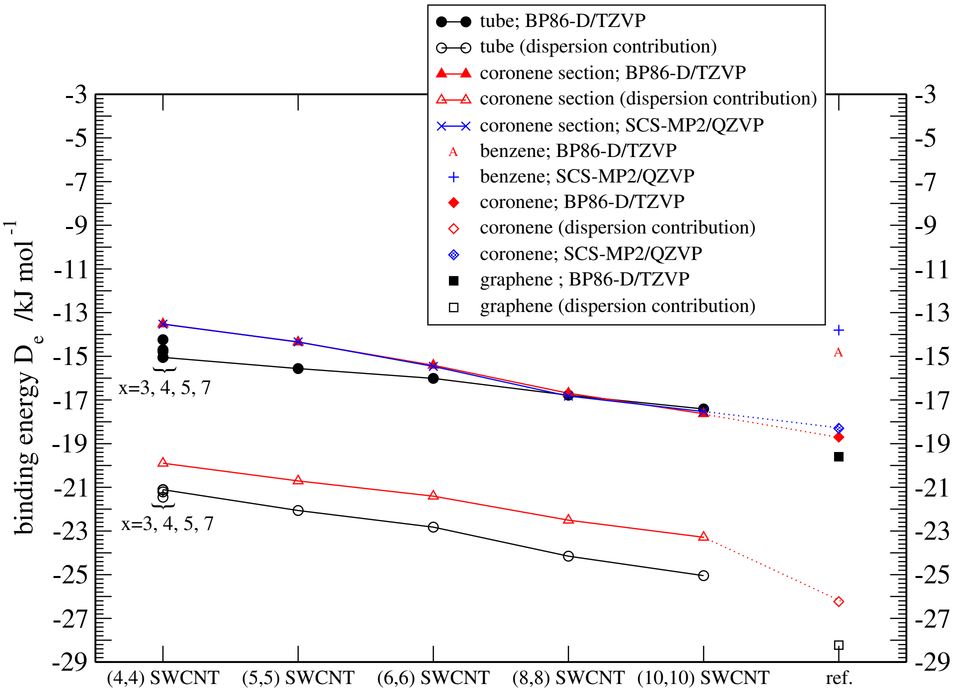

Figure 3.13. The binding energies D_e of MeOH interacting with the different armchair tube sections and the curved coronene subsections are plotted. The dispersion contributions to the binding energy are also shown, as evaluated with the empirical dispersion correction scheme. (x is the number of benzene units along the tube axis.)

moments is of minor importance. The equilibrium R_{OX} values of 331–332 pm in graphene–MeOH and 332 pm in coronene–MeOH show that the geometries are less sensitive to the model size than the binding energies. From Fig. 3.13, it can be seen that the SWCNT–alcohol binding energy is governed by dispersive forces acting in a local region, and thus the interaction is mainly of local character as was already concluded when tube sections of different lengths were investigated. Aside from the aforementioned perturbations, the chosen model will fail if it is too small such that the local region is described insufficiently, as seen for the coronene–EtOH model. Here, a binding energy of only $-24.5\,\mathrm{kJ\,mol^{-1}}$ ($R_{OX} = 328\,\mathrm{pm}$) is computed, whereas D_e is $-27.5\,\mathrm{kJ\,mol^{-1}}$ ($R_{OX} = 322\,\mathrm{pm}$) for graphene–EtOH. The SCS-MP2 binding energies for the coronene–MeOH subsections coincide perfectly with the BP86-D/TZVP values, supporting the conclusions from section 3.1. This result emphasises the applicability of the DFT-D approach for these systems.

The endohedral binding energies, D_e, for MeOH and EtOH interacting with the interior of the finite armchair SWCNT series are given in Table 3.10. Although the smaller alcohol molecule MeOH does not fit into the narrow (4,4) tube

Table 3.10. Binding energies D_e and equilibrium distances R_{OX} for the endohedral interaction of MeOH and EtOH with finite armchair SWCNTs of various diameters at the BP86-D/TZVP level of theory (sections with $x = 3$ (MeOH) and $x = 5$ (EtOH), perpendicular approach). For the limiting case of zero-curvature in graphene, see Table 3.8.

	MeOH		EtOH	
tube	D_e /kJ mol^{-1}	R_{OX} /pm	D_e /kJ mol^{-1}	R_{OX} /pm
(4,4) SWCNT	+252.6	285 (257[a])	–	–
(5,5) SWCNT	−51.4	345 (322[b])	−23.6	414 (268[b])
(6,6) SWCNT	−45.0	346	−70.0	333
(7,7) SWCNT	−34.6	327	−55.5	327
(8,8) SWCNT	−29.7	325	−47.2	328
(10,10) SWCNT	−25.2	325	−37.0	326
(12,12) SWCNT	−23.9	332	–	–

[a] distance to 6-ring centre opposite to centre X
[b] distance to CC bond above the 6-ring centre X

($d = 0.53\,$nm) and possesses an interaction energy that is strongly repulsive ($D_e = +252.6\,$kJ mol^{-1}), the ideal tube diameter within the armchair series is already achieved for the (5,5) tube ($d = 0.67\,$nm). The strongest interaction for MeOH is observed inside the (5,5) tube, with a binding energy of $-51.4\,$kJ mol^{-1} that decreases with increasing tube diameter, reaching a value of $D_e = -23.9\,$kJ mol^{-1} in the wide (12,12) tube ($d = 1.62\,$nm). The latter binding energy is close to the value of $D_e = -20.0\,$kJ mol^{-1} found for MeOH interacting with a graphene layer. In the equilibrium geometry of the endohedral (5,5) SWCNT–MeOH complex, the oxygen atom is 345 pm above a central 6-ring resulting in a distance of 322 pm to the CC bond above. The larger EtOH molecule fits into the (5,5) SWCNT, weakly binding by $-23.6\,$kJ mol^{-1} (comparable to the exohedral (10,10) SWCNT–EtOH interaction), yet it is the (6,6) SWCNT ($d = 0.81\,$nm) that has the ideal diameter for EtOH in the armchair series. Here, the binding energy increases by a factor of 3 to $D_e = -70.0\,$kJ mol^{-1}. In the equilibrium geometry of the endohedral (6,6) SWCNT–EtOH complex, the orientation of the EtOH molecule is similar to that found for MeOH. The OH bond is pointing down towards one side of the tube ($R_{\mathrm{OX}} = 333\,\mathrm{pm}$, OH bond rotated away from the OX connecting line by about 16°) with the O–CH_2 bond almost parallel to the tube axis, while the methyl group (in contrary to MeOH) points to the wall on the opposite side. This dispersive interaction of the methyl group with the opposite tube wall is weakened with increasing diameter, and the orientation of EtOH with the OH and the methyl groups interacting with the same side of the tube as in the exohedral interaction is favoured (an example of the (8,8) SWCNT is shown at the bottom right of Fig. 3.9). These structural changes due to the increasing diameter are again accompanied by a decrease in binding energy, heading towards the value of $D_{\mathrm{e}} = -27.5\,\mathrm{kJ\,mol^{-1}}$ computed for graphene.

The results and conclusions of this section are summarised here. For both alcohols, MeOH and EtOH, the endohedral adsorption site on SWCNTs is favoured over the exohedral site. This computational result confirms the conclusions of Ellison *et al.* and Burghaus *et al.*, drawn from their FTIR and TDS experiments, respectively. A diameter-dependence of the binding energy for MeOH and EtOH is found for both adsorption sites. For the exohedral interaction, D_{e} increases with increasing diameter, reaching its maximum for a graphene layer. In contrast, for the endohedral site there exists an ideal tube diameter for each of the alcohols, wherein D_{e} reaches a maximum but then decreases with increasing diameter. The value of D_{e} in the graphene layer is thus the minimum binding energy for the endohedral interaction. For the armchair series, the ideal diameter corresponds to the (5,5) tube for MeOH, and to the (6,6) tube for the larger EtOH molecule. Reducing the tube's diameter beyond the optimum value reduces the binding energy drastically, even making it repulsive at times the alcohol molecule just does not fit into the tube anymore.
The observed diameter-dependence reveals dispersion to be the main contribution to the interaction, which can be modelled by a simple Lennard–Jones type potential. Changes in the tubes' curvature affect the number of carbon atoms that are at an ideal distance from the alcohol molecules, consequently enhancing the dispersive forces. In tubes with large diameters, the exohedral and endohedral adsorptions reduce to interactions with a convex or concave layer of graphene. The stronger binding found for EtOH in comparison to MeOH arises from the additional dispersive contributions of the extra carbon atom.
In cases where the interior of the CNTs is blocked due to the production method (non-HiPCO methods), the shown diameter-dependence of the exohedral interaction, independent of the tube type, would allow for a very sophisticated tuning of the binding strength in the range of -15.0 to $-20.0\,\mathrm{kJ\,mol^{-1}}$ for MeOH and -20.6 to $-27.5\,\mathrm{kJ\,mol^{-1}}$ for EtOH. This tuning of the binding strength is

experimentally achievable by sorting CNTs according to their diameter, *i.e.* employing density-gradient ultracentrifugation techniques (sorting within a 0.02 nm range).[135–137] The determined energy interval in the physisorption region is of special interest in the research field of storage in carbon-based materials.

3.3. Water encapsulation in open cage [59]fullerenones

Intense interest in the endohedral chemistry of fullerenes, that is, the encapsulation of atoms or molecules in the hollow carbon cage, came about simultaneously with the fullerenes' discovery by way of the synthesis of metallofullerenes.[138] These endohedral metallofullerenes are generally prepared by vaporisation (*e.g.* laser vap.) of graphite/metal oxide or carbide composites, wherein the metal atom is enclosed during the fullerene formation. In contrast, rare gases and atomic nitrogen can be inserted under high-pressure, high-temperature conditions or plasma reactions into the pristine fullerene.[139–143] Endohedral fullerene complexes are of great scientific interest because of their host–guest interactions that serve to stabilise reactive species, and because of their promise for new properties that could be potentially useful in material science.[144] In line with this, the scope of several studies is the impact of the guest molecule on its host, and vice versa.[145–147] The insertion under forced conditions described above is only possible for atoms, mostly metals and rare gases, but is not feasible for molecules. For the latter, 'molecular surgery' has to be conducted, wherein carbon–carbon bonds of the fullerene are cleaved to create an opening in the cage that lets the guest molecule pass. Although there have been numerous computational investigations on small molecules such as H_2, N_2, CO, and H_2O that theoretically form endohedral complexes with fullerenes,[148–151] it was not until 2005 when Komatsu *et al.* succeeded in a beautiful example of molecular design to open C_{60} and then restore the cage after the insertion of H_2, forming $H_2@C_{60}$.[152] Nevertheless, the skeleton modification of fullerenes to obtain open-cage fulleroids with different orifice sizes has been and still is an active field in fullerene science.[153–157] In contrast to full endohedral complexes, the open-cage fullerenes easily enclose and release guest molecules in a reversible manner. This property makes them especially interesting as delivery molecules, *i.e.* for pharmaceutical applications. Thus, increasing the orifice size to allow for the insertion of larger molecules is currently of great interest. It was Iwamatsu and co-workers that originally synthesised cage-opened fullerenes with openings large enough to insert carbon monoxide or water.[158,159] With the increasing number of available open-cage fulleroids, the need for a reliable quantification of their properties, such as orifice size[160] or barrier height for insertions, has become necessary. Computationally, special care has to be taken to accurately describe the weak host–guest interaction with suitable methods.

The present quantum chemical study shall focus on two cage-opened [59]fullerenones with large orifices recently reported by Xiao *et al.*[161] By multistep chemical reactions that start from $C_{60}(OO\textit{t}Bu)_6$, including the cleavage of five fullerene carbon–carbon bonds and the elimination of one skeleton carbon atom from the C_{60} cage, these authors have synthesised the [59]fullerenones **1** with an 18-membered-ring orifice and **2** with a 19-membered-ring orifice. The corresponding structures are displayed in Fig. 3.14. Xiao *et al.* found **1** and **2** to be 'excellent molecular water traps' forming the complexes H_2O@**1** and H_2O@**2**, which were characterised by ^{1}H-NMR experiments and X-ray structure analysis. Thus, the focus of this section is on the computational characterisation of the cages **1** and **2** and their complexes H_2O@**1** and H_2O@**2**. Structures, binding energies, and barrier heights shall be calculated using the DFT-D approach that was benchmarked in section 3.1 and successfully applied to carbon nanotubes in section 3.2. Since in this benchmark and initial application, BP86-D has proven to yield accurate results of SCS-MP2 quality for the systems benzene–MeOH and coronene–MeOH, and, as reported there, also performs especially well for benzene–H_2O and benzene–NH_3, one can expect BP86-D to perform equally well for the structurally and chemically related system H_2O@[59]fullerenone. This reasonable assumption is the motivation for the following study.

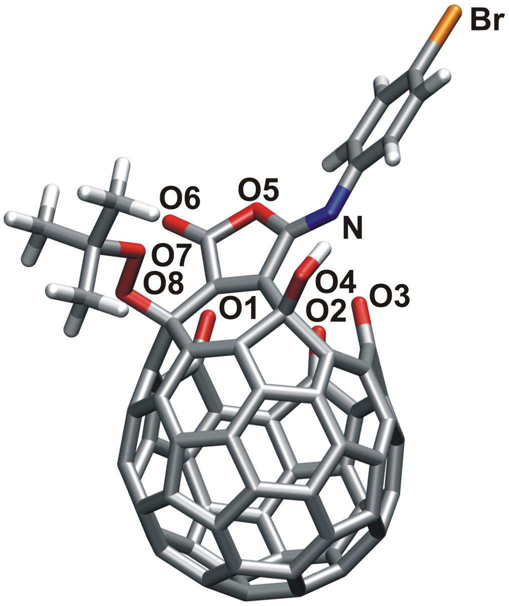

1

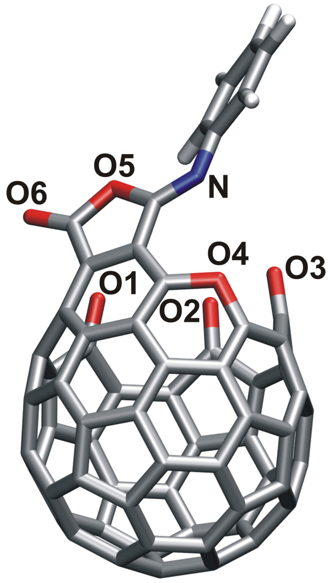

2

Figure 3.14. The geometries of the two [59]fullerenone cages **1** and **2** at the BP86-D/def2-TZVP level of theory. **1** has an 18-membered-ring orifice, **2** a larger 19-membered-ring orifice. Atoms not labelled explicitly are carbon (grey) and hydrogen (white).

The computational details are as follows. Equilibrium structures of the [59]fullerenone cages **1**, **2** and of the water-encapsulated complexes H_2O@**1**, H_2O@**2** are optimised using BP86-D with the def-SV(P) and def2-TZVP basis sets, applying the RI approximation with corresponding auxiliary basis sets.[65,66,86–88,162,163] A fine multiple integration grid (gridsize m4) is used, setting the SCF convergence to $10^{-7}\,E_h$. The final convergence criteria are set to $10^{-4}\,E_h/a_0$ for the Cartesian gradient norm and $10^{-6}\,E_h$ for the energy change. These settings are also used for the TS searches described later in this section. For all BP86-D/def-SV(P) equilibrium geometries, harmonic vibrational frequencies are calculated analytically to confirm real minima.[164–166] For comparison, the structures of the Buckminsterfullerene C_{60} and the corresponding water complex $H_2O@C_{60}$ are calculated at the same level.

In addition, MP2 and SCS-MP2 single point energies are calculated for the BP86-D/def2-TZVP equilibrium structures of C_{60} and $H_2O@C_{60}$, using the module Ricc2 and applying a def2-TZVP and def2-QZVP basis with corresponding auxiliary basis sets.[66,68,89–91,162,167] The HF reference wave functions for the subsequent MP2 runs are calculated using the RI approximation for the Coulomb part (RI-J) employing def2-TZVP, and for both the Coulomb and exchange parts (RI-JK) employing def2-QZVP.[168–170]

The procedure of the TS search for the water molecule leaving the cages of H_2O@**1** and H_2O@**2** is composed of the following steps: The water molecule of each complex, H_2O@**1** and H_2O@**2**, is moved from its equilibrium position in the cage towards the orifice by increasing the distance d(OR) in steps of 50 pm. The distance, d(OR), is measured from the water's oxygen atom to the centre of the bottom pentagon in the fullerene cage. Then, the perpendicular position of the water molecule is fixed by freezing its distance, angle, and dihedral angle with respect to the bottom pentagon. For each structure along the perpendicular pathway, all other degrees of freedom are optimised at the BP86-D/def2-TZVP level. The total energies of these optimised structures are plotted and the energy pathways are refined by calculating additional points (10–20 pm steps) about the maximum of the plot.

The maximum energy structure on the perpendicular pathway of H_2O@**2** is then reoptimised at the BP86-D/def-SV(P) level and taken as the best initial guess for a saddle point search, applying the surface walking algorithm of the module Statpt. To do so, an exact initial Hessian is calculated at the BP86-D/def-SV(P) level of theory, and the transition vector that will be followed in the course of the TS optimisation is identified. It is the eigenvector with a negative eigenvalue that corresponds to the vibrational mode of the water molecule moving in the direction of the cage's opening. Updated Hessians are used within one run, but it has become obvious throughout the optimisations with BP86-D/def-SV(P) that several restarts with a recomputed exact Hessian are necessary to finally locate the saddle point.

As it turns out, the initial guess from the perpendicular pathway for H_2O@**1** is insufficiently close to the TS, that is, too far to directly reach the saddle point via the surface walking procedure. This observation suggests a somewhat more complicated PES of H_2O@**1** in comparison to H_2O@**2**. Thus, a more sophisticated approach must be used by combining the interpolation algorithm of the growing string method, as described in section 2.6.2, with a subsequent surface walking calculation on the resulting new best guess for the saddle point. Distorting the maximum energy structure obtained from the perpendicular pathway along the normal mode (imaginary frequency) that resembled the movement of the water molecule towards the orifice, the reactant and product structures for the growing string method are generated. A total of 9 nodes are used along the string. Both the growing string method and the surface walking procedure are performed at the BP86-D/def-SV(P) level of theory.

The final TS for H_2O@**1** and H_2O@**2** are confirmed by computing the exact Hessians and vibrational frequencies at the BP86-D/def-SV(P) level, showing one and only one imaginary frequency. Final single point energies for these TS are calculated at the BP86-D/def2-TZVP level. All binding energies and barrier heights are corrected for BSSE by the function counterpoise technique.[74,94]

3.3.1. Equilibrium structures of H_2O@[59]fullerenones

The equilibrium structures (EQ) of H_2O@**1** and H_2O@**2** are shown on the left panels of Figs. 3.15 and 3.16, respectively. To analyse the influence of the host–guest interaction on the structural parameters, the equilibrium geometries of these complexes are compared to the empty cages (Fig. 3.14) and to a free water molecule optimised at the same level of theory. Neither the parameters of the guest water molecule nor the local structure of the [59]fullerenone host cages undergo measurable changes at encapsulation. The C–C bond lengths within the pentagons and hexagons of the cages as well as the bond lengths of the substituents around the orifice stay unaltered. Comparing the soft binding parameters of the through space O–O distances listed in Table 3.11, a decrease in the O1–O3 distance by 2 pm and 5 pm for H_2O@**1** and H_2O@**2**, respectively, are observed at the BP86-D/def-SV(P) level. Using the larger basis set def2-TZVP, this decrease is reduced to about 0.7 pm, revealing the change to be largely a basis set effect. To summarise these findings: The host cage has no impact on the structure of its guest. Furthermore, the impact of the guest water molecule on its host is fairly negligible and only measurable in soft through space binding parameters. In Table 3.12, counterpoise corrected binding energies, ΔE^{CP}, are

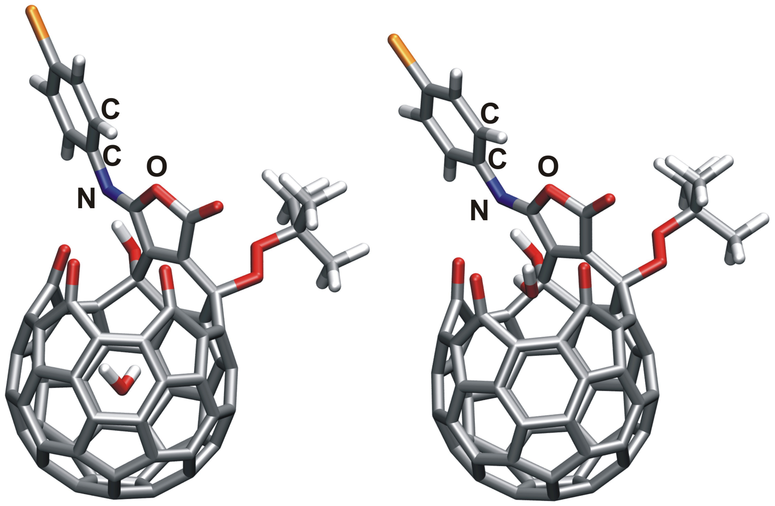

H_2O@1 (EQ) **H_2O@1 (TS)**

Figure 3.15. Equilibrium (EQ, left) and transition state (TS, right) structure of H_2O@**1** at the BP86-D/def-SV(P) level of theory. The barrier height is 107.9 kJ mol^{-1} (BP86-D/def2-TZVP//BP86-D/def-SV(P)). The indicated atoms form the dihedral angle ONCC between the phenyl substituent and the isomaleimide unit.

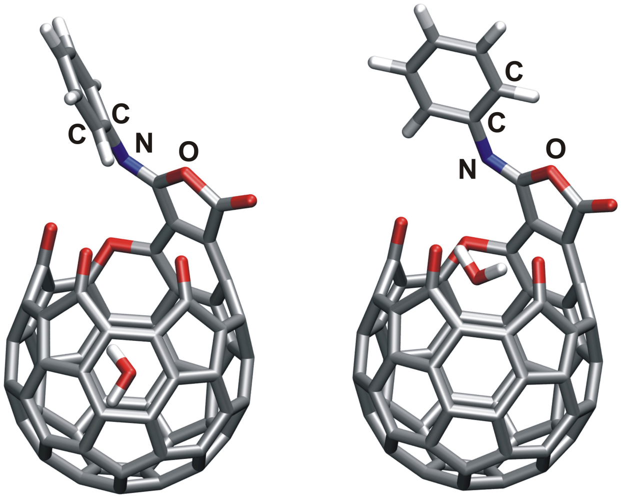

H_2O@2 (EQ) **H_2O@2 (TS)**

Figure 3.16. Equilibrium (EQ, left) and transition state (TS, right) structure of H_2O@**2** at the BP86-D/def-SV(P) level of theory. The barrier height is 46.4 kJ mol^{-1} (BP86-D/def2-TZVP//BP86-D/def-SV(P)). The indicated atoms form the dihedral angle ONCC between the phenyl substituent and the isomaleimide unit.

Table 3.11. The O–O distances (pm) between the keto groups surrounding the rim of the orifices for the empty fullerenone cages **1** and **2** and for the equilibrium and TS structures of H_2O@**1** and H_2O@**2** (at the BP86-D level).

	1	H_2O@**1**(EQ)	H_2O@**1**(TS)	**2**	H_2O@**2**(EQ)	H_2O@**2**(TS)
BP86-D/def-SV(P)						
O1–O3	405.9	400.9	508.4	476.1	474.2	500.8
O1–O2	293.9	294.2	347.9	291.3	290.2	317.0
O2–O3	296.0	296.7	331.4	299.4	299.6	322.3
BP86-D/def2-TZVP						
O1–O3	414.7	414.0		481.0	480.3	
O1–O2	299.1	298.4	–	297.6	296.4	–
O2–O3	301.6	300.8		305.9	305.6	

given with ΔE evaluated as $\Delta E = E(\mathrm{H_2O@[59]fullerenone}) - E(\mathrm{[59]fullerenone}) - E(\mathrm{H_2O})$. ΔE^{CP} is found to be virtually the same for H_2O@**1** and H_2O@**2**, that is, $-44.4\,\mathrm{kJ\,mol^{-1}}$ and $-44.6\,\mathrm{kJ\,mol^{-1}}$, respectively. It is instructive to compare these results to ΔE^{CP} values calculated at the conventional BP86 level (cf. Table 3.12). At this level, ΔE^{CP} is repulsive, and the water is not bound in the cage. Thus, the stability of the host–guest complex is only due to dispersive forces. This result emphasises once again how essential it is to include long-range dispersion in the

Table 3.12. Uncorrected and counterpoise corrected binding energies ΔE, ΔE^{CP} for an encapsulated water molecule in H_2O@**1** and H_2O@**2** at the BP86-D level of theory. For comparison, the BP86 results without dispersion correction are also shown. All energies are in $\mathrm{kJ\,mol^{-1}}$.

	H_2O@**1**		H_2O@**2**	
	ΔE	ΔE^{CP}	ΔE	ΔE^{CP}
BP86/def2-TZVP	2.3	13.1	0.7	11.0
BP86-D/def-SV(P)	−81.6	−43.5	−79.0	−40.8
BP86-D/def2-TZVP	−55.2	−44.4	−55.4	−44.6

computational method of choice, if one is to describe weakly interacting systems of this type even *qualitatively* correctly. Comparing the binding energy of water in H_2O@**1** and H_2O@**2** to that of a water molecule encapsulated in an intact C_{60} cage, ΔE^{CP} diminishes only by about 10% due to the cage opening. The finding that the stabilisation of the water inside the cage is not significantly affected by cage modifications allows for a further check of the chosen method using the complex $H_2O@C_{60}$. In contrast to H_2O@**1** and H_2O@**2**, SCS-MP2 single point energy calculations including CP corrections are still feasible with large enough basis sets for the host–guest complex $H_2O@C_{60}$ which has no substituents. The results of these calculations are summarised in Table 3.13. Comparing the BSSE corrected binding energies at the def2-TZVP level, MP2 is again found to bind stronger (11 kJ mol^{-1}) than SCS-MP2, as discussed previously in the benchmark section 3.1. In the basis set limit, this would result in an overbinding of MP2 for the $H_2O@C_{60}$ system. Increasing the basis set size from def2-TZVP to def2-QZVP, the SCS-MP2 binding energy ΔE^{CP} increases by 5 kJ mol^{-1} to 48.8 kJ mol^{-1}, emphasising the need for large orbital basis sets within the correlation treatment. The BP86-D/def2-TZVP binding energy agrees with the SCS-MP2/def2-QZVP//BP86-D/def2-TZVP values to within 0.3 kJ mol^{-1}, confirming the conclusions drawn about the method's performance in the benchmark section 3.1. This convincing performance of BP86-D further validates the accuracy of the barrier heights that shall be discussed in the next section.

The diameter of the C_{60} cage (atom to atom distance) is 709.4 pm at the BP86-D/def2-TZVP level, whereas the distance between the centres of two opposite

Table 3.13. Uncorrected and counterpoise corrected binding energies ΔE, ΔE^{CP} for an encapsulated water molecule in $H_2O@C_{60}$ at the BP86-D, MP2 and SCS-MP2 levels of theory. All energies are in kJ mol^{-1}.

	$H_2O@C_{60}$	
	ΔE	ΔE^{CP}
BP86-D/def-SV(P)	−85.3	−47.0
BP86-D/def2-TZVP	−60.1	−49.1
MP2/def2-TZVP//BP86-D/def2-TZVP	−86.6	−54.5
SCS-MP2/def2-TZVP//BP86-D/def2-TZVP	−66.9	−43.5
SCS-MP2/def2-QZVP//BP86-D/def2-TZVP	−58.6	−48.8

pentagons is 665.0 pm. Thus, the cage centre is 332.5 pm perpendicular to any pentagon's plane. In both cage-opened fullerenones H_2O@**1** and H_2O@**2**, the water molecule is located off-centre closer to the unaltered hemisphere of the cage, 312 pm and 327 pm above the bottom pentagon, respectively. Hence, in H_2O@**2** the guest molecule is closer to the orifice than in H_2O@**1**. On the one hand, this relative difference between the configurations of H_2O in the cages **1** and **2** agrees with the experimental results from the X-ray structure analysis, but on the other hand, the absolute positions do not. Experimentally, the water molecule in H_2O@**2** is found off-centre, but closer to the orifice of the cage. The distance to the bottom pentagon is 367 pm. In the X-ray structure of H_2O@**1** the water molecule is almost centred ($d(\mathrm{OR}) = 330\,\mathrm{pm}$). These deviations of computed to experimentally observed absolute positions can be traced back to the fact that the potential energy surfaces of the complexes are very shallow around the equilibrium positions of the water molecule. As will be shown with surface scans in the next section 3.3.2, elongating the oxygen's distance from the bottom pentagon by 50 pm with respect to the equilibrium changes the energy by only about $5\,\mathrm{kJ\,mol^{-1}}$. These shallow minima lead to a challenging equilibrium structure optimisation and result in a correspondingly larger error bar for the absolute positions of the water molecule. Furthermore, non-negligible deviations between the experimental r_0 and the calculated r_e values arise due to the shallow minima and vibrational averaging would be needed for quantitatively comparing the experimental and computed distances.

Apart from its position with respect to the orifice, the orientations of the water molecule inside the cages and the possibility of a rotational barrier are subject to further investigations. In ^{1}H-NMR experiments at room temperature, Xiao *et al.* observed a free rotation of the water molecule in both H_2O@**1** and H_2O@**2**, whereas the rotation in H_2O@**2** was partially frozen in X-ray experiments at lower temperature (200 K).[161] The authors concluded from these observations that H_2O@**1** should have a lower barrier to rotation compared to H_2O@**2**. An attempt to computationally estimate the rotational barriers of water in these two complexes is made in this work by scanning the rotation with respect to the three principal axes of the H_2O molecule (BP86-D/def2-TZVP single points). At this level of theory, the energy difference for all three principal axes in H_2O@**2** is $<2\,\mathrm{kJ\,mol^{-1}}$, implying a free rotation of the water molecule. Also for H_2O@**1**, the energy difference for the rotation about I_a is $<2\,\mathrm{kJ\,mol^{-1}}$, while the barrier for both I_b and I_c is $3–4\,\mathrm{kJ\,mol^{-1}}$. Consequently, the [59]fullerenone with a smaller orifice H_2O@**1** possesses a very small rotational barrier for the water molecule, while the rotation is virtually free in H_2O@**2** with larger orifice. The computational results contradict the conclusions drawn from experiment. Taking into account the computational level that was applicable, as well as its limitations reported above for the absolute positions of the water molecule, these BP86-D results for the rotational barriers have to be considered as exploratory. To obtain more reliable quantitative rotational barriers for these large systems, highly accurate computational methods such as CCSD(T) are necessary but currently impractical.

3.3.2. Transition state structures of H_2O@[59]fullerenones

The TS structures of the water molecule leaving H_2O@**1** and H_2O@**2** are shown on the right panels of Figs. 3.15 and 3.16. The calculated barrier heights for the water molecule leaving the cage are 107.9 kJ mol^{-1} in H_2O@**1** and 46.4 kJ mol^{-1} in H_2O@**2** at the BP86-D/def2-TZVP//BP86-D/def-SV(P) level (Table 3.14). Note that the barrier height in H_2O@**2** is only about 2 kJ mol^{-1} larger than the binding energy. Consequently, there is an exceedingly small barrier of 2 kJ mol^{-1} to overcome for a water molecule to enter the cage through the 19-membered-ring orifice. In H_2O@**1**, the difference between the barrier height and binding energy is much more pronounced (64 kJ mol^{-1}). To summarise, the barrier for a water molecule to enter through the more narrow 18-membered-ring orifice in **1** is an order of magnitude higher than for the 19-membered-ring orifice in **2**. The structural changes in the TS with respect to the equilibrium structure reflect the above findings (cf. Fig. 3.15 and 3.16). The water molecule approaching and passing through the opening of the cage causes strain within the orifice, which in turn has to expand to some degree. This extent of necessary structural rearrangements from the equilibrium to the TS is a qualitative measure for the barrier height. The O–O distances between the three keto groups (C=O) around the rim of the orifice are a set of relevant structural changes for this purpose

Table 3.14. Counterpoise corrected barrier heights ΔE^{CP} for the encapsulated water molecule leaving H_2O@**1** and H_2O@**2** at the BP86-D level of theory. In addition, counterpoise corrections (ΔCP) for the equilibrium and TS structures of H_2O@**1** and H_2O@**2** are given. All energies are in kJ mol^{-1}.

	H_2O@**1**			H_2O@**2**		
	ΔE^{CP}	ΔCP(EQ)	ΔCP(TS)	ΔE^{CP}	ΔCP(EQ)	ΔCP(TS)
BP86-D/def-SV(P)	114.7	38.1	54.7	47.7	38.3	51.0
BP86-D/def2-TZVP[a]	107.9	11.1	11.6	46.4	10.9	11.5

[a] BP86-D/def2-TZVP//BP86-D/def-SV(P)

(Table 3.11; for numbering of the O atoms, cf. Fig 3.14). The C=O groups prefer to be coplanar with the ring they are attached to. In H_2O@**1** with the smaller orifice, the O1–O3 distance across the opening elongates by 107.5 pm, from 400.9 to 508.4 pm. To allow the passage of the water molecule, the keto groups have to bend towards the outside (out-of-plane), as suggested by the elongation of the O1–O2 and O2–O3 distances, from 294.2 to 347.9 pm and from 296.7 to 331.4 pm, respectively. These significant structural changes explain the larger barrier height reported for H_2O@**1** above. Cage **2** is formally obtained from **1** by inserting an oxygen atom (O4) in the rim of the orifice. This alters a five-membered ring within the rim to a six-membered cyclic ether, making the orifice not only larger but also more flexible. According to the much smaller barrier calculated for H_2O@**2**, the O1–O3 distance across the opening elongates by a mere 26.6 pm (from 474.2 pm to 500.8 pm) as the water passes. The higher flexibility of this orifice is also apparent from the O1–O2 and O2–O3 distances changing much less between equilibrium and TS structure than in H_2O@**1**. As a consequence, the maximum energy along the path of the water leaving the cage (the TS) is reached much earlier for the larger orifice. Here, the surrounding keto groups no longer act as a hindrance to passing, and d(OR) in the TS structure is 612.4 pm in H_2O@**2** whereas it is 648.8 pm in H_2O@**1**.

All these computational results are in agreement with the experimental findings of Xiao *et al*. These authors found **2** to 'incorporate water more efficiently' even at decreased temperatures (88% at −20 °C), whereas elevated temperatures were needed for H_2O@**1** (78% at 80 °C). On the other hand, **2** 'released water more readily', since no H_2O@**2** could be detected in the ESI mass spectrum and only empty **2** was present there.

In the EQ structure of the phenyl-isomaleimide molecule (cf. insert in Fig. 3.17), the ONCC dihedral angle between the plane of the phenyl substituent and the isomaleimide unit is 0°. This coplanar conformation is energetically favoured over the perpendicular conformation by about 12 kJ mol^{-1} (BP86-D/def2-TZVP), due to a hydrogen bridge between the *ortho*-H of the phenyl substituent and the oxygen atom in the ring (distance: 225 pm). In the phenyl-isomaleimide units of the cage-opened [59]fullerenones (Figs. 3.15 and 3.16), the phenyl substituent is rotated, altering ∠ONCC due to additional interactions between the *ortho*-H and the keto groups in the rim of the orifice. For the EQ structure of H_2O@**1**, the dihedral angle ONCC changes to −17.5°, elongating the former hydrogen bridge to 240 pm (cf. Table 3.15). The different shape of the larger orifice in H_2O@**2** allows for a more central position of the phenyl-*ortho*-H above the three keto-oxygen atoms O1, O2, and O3, resulting in stronger interactions (refer to Fig 3.14 for the numbering of atoms). Thus, the hydrogen bridge within the phenyl-isomaleimide unit of H_2O@**2** is further weakened (250 pm) and the

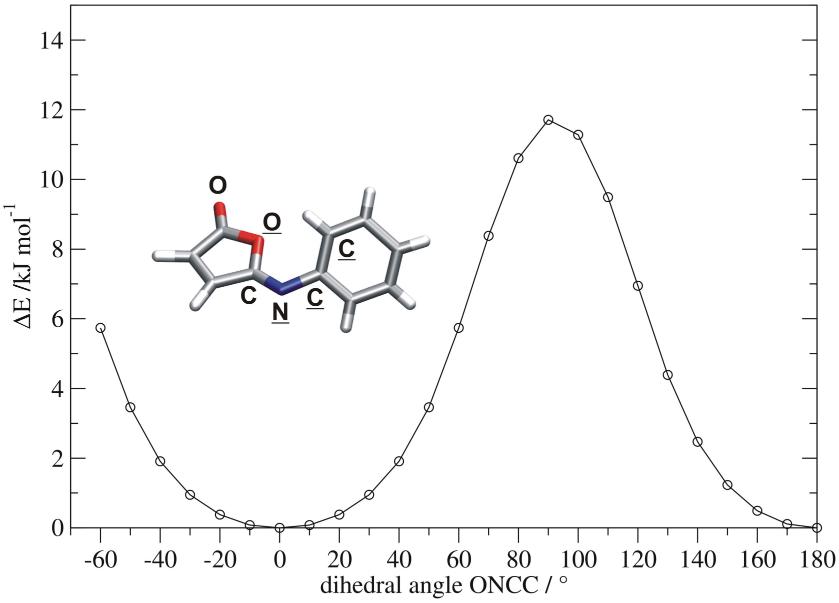

Figure 3.17. Rotational energy in the phenyl-isomaleimide molecule as function of the dihedral angle ONCC (BP86-D/def2-TZVP). The phenyl-isomaleimide molecule is displayed as insert, atoms forming ∠ONCC are indicated with underlined labels. Atoms not labelled explicitly are carbon (grey) and hydrogen (white).

ONCC dihedral angle increases to −49.0°. The experimental X-ray value of ∠ONCC agrees well with the calculated value for H_2O@**2**, but differ by a factor of 1.7 in case of H_2O@**1** (perhaps due to packing effects in the crystal). On the one hand, the out of plane movement of the keto groups in the TS of H_2O@**1** decreases their interaction with the *ortho*-H, but on the other hand the phenyl group has to make way for the approaching water molecule. As a consequence, the phenyl group turns back (∠ONCC: −10.2°), restoring the hydrogen bridge

Table 3.15. Comparison of the dihedral angle ONCC (°) in the equilibrium and TS structures of H_2O@**1** and H_2O@**2** (BP86-D/def-SV(P)). Values in the crystal structures are given between parentheses.

	∠ONCC	
	H_2O@**1**	H_2O@**2**
EQ	−17.5(−30.1)	−49.0(−50.8)
TS	−10.2	+21.0

of the *ortho*-H to the oxygen of the isomaleimide unit (228 pm). The deviations of the dihedral angle ONCC and of the bond length of the H-bridge in the TS of $H_2O@\mathbf{1}$ with respect to the isolated phenyl-isomaleimide molecule can be ascribed to the strain in the orifice that affects the isomaleimide unit. The ONCC dihedral angle in $H_2O@\mathbf{2}$ changes drastically from $-49.0°$ in the EQ to $+21.0°$ in the TS structure. This orientation of the phenyl group in the TS structure unblocks the opening of the cage for the passing water, but allows for two hydrogen contacts of the *ortho*-H atoms: one with the O3 keto-oxygen atom, and the other with the ring-oxygen atom of the isomaleimide unit (236 pm). To summarise, the ONCC dihedral angle in the substituents of the [59]fullerenones is a sensitive indicator for the strain in the orifice, as well as for its changes from EQ to TS.

In addition to the ΔE^{CP} values in Tables 3.12 and 3.13, the uncorrected binding energies (ΔE) are listed to examine the extent of the effect of BSSE with increase in basis set size in such weakly interacting systems. With the DFT-D method, the small to medium sized basis set def-SV(P) results in a BSSE of about 80–90% of the binding energy. Increasing the basis set to def2-TZVP, the BSSE is reduced to about 20–25% of ΔE^{CP} but remains substantial. Thus, a correction for BSSE is important even for def2-TZVP, which is considered as a large basis set yielding quantitative results within a DFT treatment. Without any doubt, the BSSE correction for def-SV(P) is indispensable to obtaining qualitatively meaningful results. In the wavefunction-based correlation treatment, it is observed that def2-TZVP and def2-QZVP are to MP2 as def-SV(P) and def2-TZVP are to DFT. The proportions of BSSE are 50–60% (def2-TZVP) and around 20% (def2-QZVP), respectively. Table 3.14 additionally shows the counterpoise energies ΔCP, correcting for BSSE in the equilibrium and TS structures. It becomes evident from this table that the counterpoise correction is not only important for the EQ binding energies but also for the TS energies when small to medium sized basis sets, such as def-SV(P) are employed. In $H_2O@\mathbf{1}$, for example, ΔCP in the EQ structure is $38.1\,\mathrm{kJ\,mol^{-1}}$ but increases to $54.7\,\mathrm{kJ\,mol^{-1}}$ in the TS structure when the water molecule and its basis functions are close to the atoms of the orifice. As a consequence, the BSSE does not cancel out when calculating the barrier height, and the CP correction has to be included to obtain the right result. Large basis sets such as def2-TZVP must be utilised to make the difference in ΔCP sufficiently small, ensuring error cancellation.

3.4. Metal complexes with functionalised fullerene ligands

Exohedral addition chemistry of fullerenes is well developed and widely used in functionalising the fullerenes' cages. This functionalisation is key to fullerene-based advanced materials.[144,171,172] Almost any functional group can be connected to the [60]fullerene cage via addition or cyclo-addition reactions to obtain fullerene derivatives with promising new properties, *e.g.* building units for polymers and solids.[171,173–176] In contrast to the skeleton modifications described in the previous application (section 3.3), the C_{60} cage remains intact in these reactions.

Cyclopropanation of fullerene C_{60} with malonate derivatives via the Bingel and Bingel–Hirsch reactions yields methanofullerenes bearing the desired functional groups.[173,177] Selective multiadditions to fullerenes are achieved following the concept of 'tether-directed remote functionalisation' pioneered by Diederich and co-workers.[175,178–180] A molecule consisting of two reactive groups, separated by a spacer (the tether) is attached to the fullerene via the first reactive group. Steric constraints, controlled by the design of the tether, then allow the second reactive group to dock with just a single, specific position in the cage. Thus, predefined addition patterns are available for designing functionalised fullerenes as building blocks for nanostructures.

In the research group of Bräse at Karlsruhe University, methanofullerene malonates with different functional heading groups, such as pyridines, benzonitriles, and triphenylphosphines are synthesised. Due to their sticky sides, these structures are potential candidates for forming well-organised chains, 2D-, and 3D-networks with metal centres. The goal is to create new organic linkers, based on functionalised fullerenes, that form porous coordination polymers.[181,182] These metal–organic frameworks (MOFs) are of great scientific interest due to their exceptional physical and chemical properties, *e.g.* separation functionality, gas storage capacity, catalytic action, and so forth.[8,183]

Pierrat *et al.*[181] reported in 2008 on the synthesis of a bis-pyridine C_{60} mono-adduct that with $CuCl_2$ quantitatively forms the intramolecular complex **1**, as illustrated in Fig. 3.18. To obtain higher coordination adducts, *e.g.* chains, the ligands have to be tailored in such a way that intermolecular is favoured over intramolecular complexation. Pierrat *et al.* addressed this specification by the synthesis of C_{60} bis-adducts with bis-pyridine and bis-benzonitrile head groups, applying the tether concept in double Bingel cyclopropanations. These C_{60} bis-adduct ligands could favour an intermolecular metal coordination due to conformational requisites imposed by the spacer between the sticky sides.

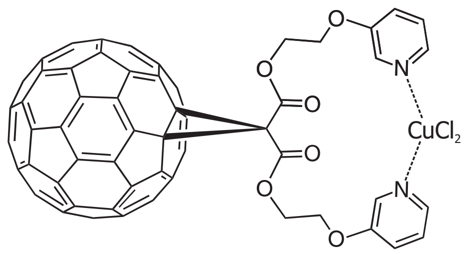

1

Figure 3.18. Metal complex **1** formed by a bis-pyridine C_{60} ligand and $CuCl_2$ (Pierrat *et al.*). The intramolecular metal complexation with both coordination sites of one ligand attached to the same Cu-centre takes place quantitatively.

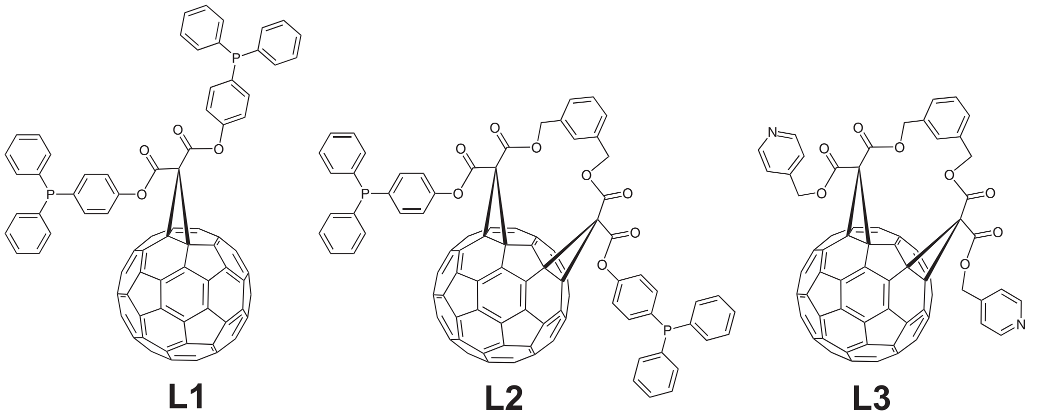

L1 **L2** **L3**

Figure 3.19. Fullerene ligands for metal complexation: Bis-triphenylphosphine C_{60} mono-adduct **L1**, bis-adduct **L2**, and bis-pyridine C_{60} bis-adduct **L3** functionalised via a single and double Bingel cyclopropanation.

The bis-pyridine C_{60} bis-adduct ligand **L3** is shown in Fig. 3.19 on the right. Substituting the pyridines with triphenylphosphine head groups, which have an increased spatial requirement themselves, is an alternative route for suppressing intramolecular coordination. On the left panel of Fig. 3.19, two of these functionalised fullerene ligands bearing triphenylphosphine head groups are shown: the C_{60} mono-adduct **L1** and bis-adduct **L2**. In ligand **L2**, there exists a combination of large functional head groups with a spacer-group in between. A theoretical classification of these functionalised fullerene ligands and a quantification of the impact of the utilised design elements are desired in order to sort out the candidates that are likely to build networks via intermolecular coordination.

In the following quantum chemical study, these issues arising from the experiments are addressed by computationally investigating the complexation of a metal centre with the functionalised fullerene ligands **L1**, **L2**, and **L3**. Intramolecular and intermolecular coordinations of the fullerene ligands to $PdCl_2$ are examined with regard to the effects that the tether and the different head groups have on the complexation energies.

The computational details are as follows. The equilibrium structures of the fullerene ligands **L1**, **L2**, and **L3**, as well as the intramolecular $PdCl_2L$ and intermolecular $PdCl_2(L)_2$ complexes are optimised at the BP86/def2-SV(P) level of theory, employing the RI approximation.[65,87,163] A fine multiple integration grid (gridsize m4) is used, setting the SCF convergence to $10^{-7}\,E_h$. The default values for the final convergence criteria are used (Cartesian gradient norm $10^{-3}\,E_h/a_0$, energy change $10^{-6}\,E_h$). Total energies for the structures are finally calculated as single points with BP86/def2-TZVP on top of the BP86/def2-SV(P) geometries.[66,162,163] Complexation energies are then evaluated for intramolecular complexes as $\Delta E = E(PdCl_2L) - E(PdCl_2) - E(L)$, and for intermolecular complexes as $\Delta E = E(PdCl_2(L)_2) - E(PdCl_2) - 2\cdot E(L)$. To check the functional dependence of the results, the intramolecular complexes $PdCl_2L$ are also optimised with TPSS/def2-SV(P), with complexation energies also evaluated at this level. The influence of the basis set on the geometries, and in turn on the complexation energies, is tested for **PdCl$_2$L1**, by reoptimising the structure with BP86/def2-TZVP and then calculating the complexation energy at this geometry.

The structures of the intramolecular coordination of the fullerene ligand **L1** and the intra- and intermolecular coordination of **L2** to $PdCl_2$ are shown in Figs. 3.20 and 3.21. Selected structural parameters of the intra- and intermolecular complexes are given in Table 3.16. Steric constraints in the ligands **L1**, **L2** force a *cis*-coordination of the sticky sides in the intramolecular complexes, whereas the more favourable *trans*-coordination is found for the intermolecular complexation.

Table 3.16. Selected bond lengths (pm) in the intramolecular complexes **PdCl$_2$L1**, **PdCl$_2$L2** and the intermolecular complexes **PdCl$_2$(L1)$_2$**, **PdCl$_2$(L2)$_2$** at the BP86/def2-SV(P) level of theory (values in parentheses at the BP86/def2-TZVP level). For the numbering of atoms refer to Figs. 3.20 and 3.21.

	PdCl$_2$L1	**PdCl$_2$L2**	**PdCl$_2$(L1)$_2$**	**PdCl$_2$(L2)$_2$**
Pd–P1	233.1 (231.5)	232.6	237.2	237.1
Pd–P2	235.1 (233.3)	232.2	237.1	237.0
Pd–Cl1	236.3 (234.7)	236.9	234.8	234.8
Pd–Cl2	236.5 (235.0)	236.6	234.9	234.9

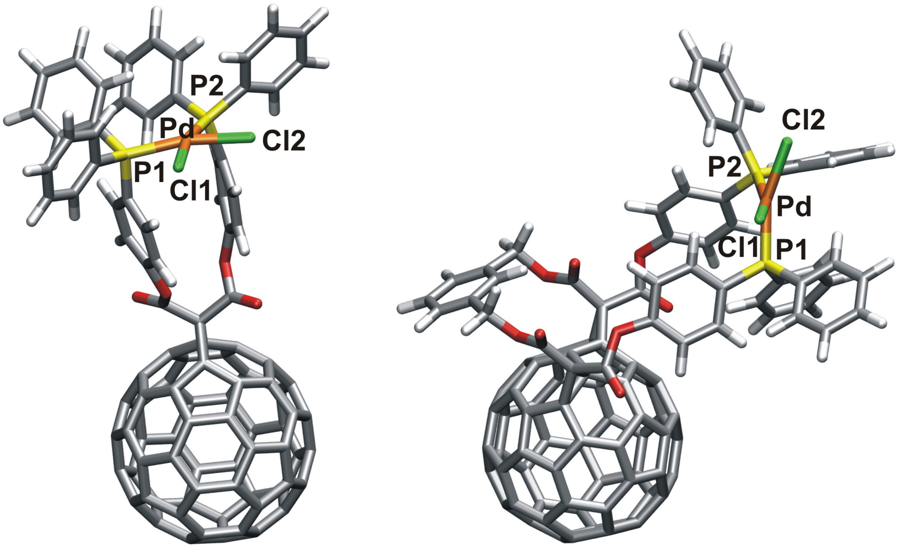

$PdCl_2L1$ **$PdCl_2L2$**

Figure 3.20. Intramolecular metal coordination of Pd(II) with the bis-triphenylphosphine C_{60} fullerene ligands **L1** and **L2**, forming the complexes **$PdCl_2L1$** (left) and **$PdCl_2L2$** (right), respectively. BP86/def2-SV(P) structures are displayed.

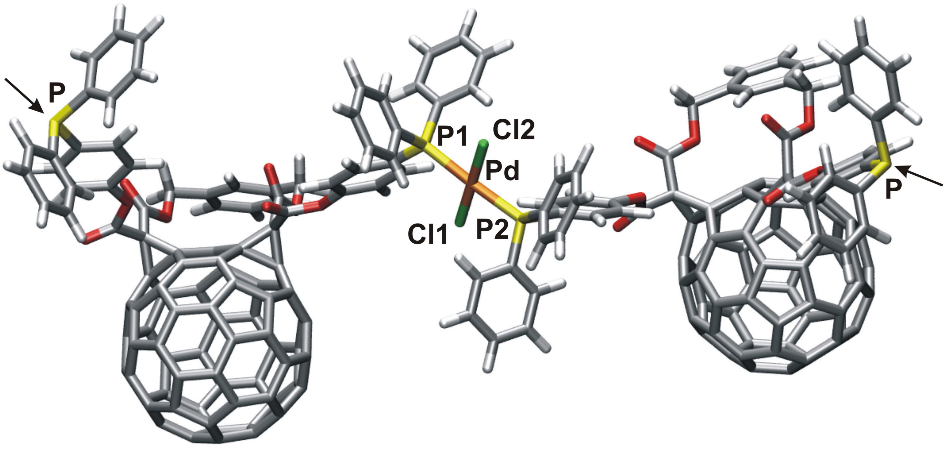

$PdCl_2(L2)_2$

Figure 3.21. Intermolecular metal coordination of Pd(II) with the bis-triphenylphosphine C_{60} fullerene ligand **L2**, forming the dimeric complex **$PdCl_2(L2)_2$**. The BP86/def2-SV(P) structure is displayed. The free coordination sites (P-triphenylphosphine) of the ligands for forming longer chains are indicated with arrows.

The *cis*-coordination of the large triphenylphosphine head groups introduces sterical strain within the coordination site, resulting in a distortion from the square-planar complexation of the metal centre. In **$PdCl_2L1$**, the atoms P–Pd–Cl deviate from a collinear orientation by about 12°. In the complex **$PdCl_2L2$** with the C_{60} bis-adduct ligand **L2** (which has its coordination sites separated by a tether), this deviation is even more pronounced ($\angle$PPdCl 16–20°). The sterical strain within the coordination site further manifests in an unsymmetrical bonding pattern where Pd–P1 differs from Pd–P2, consequently affecting Pd–Cl1 and Pd–Cl2. Intermolecular coordination of $PdCl_2$, resulting in the complexes **$PdCl_2(L1)_2$** and **$PdCl_2(L2)_2$**, is free of this steric strain, and a square-planar *trans*-coordination with equally distanced Pd–P and Pd–Cl bonds is realised (cf. Table 3.16 and Fig. 3.21). Compared to the *cis*-complex, the Pd–P bonds are elongated in the *trans*-complex by 2–5 pm, shortening the Pd–Cl bonds by 1–2 pm. These changes in bond lengths arise to some extent from an altered structural *trans*-effect in the P–Pd–P sequence (when compared to P–Pd–Cl). However, the large increase of the Pd–P bond length ($\sim$5 pm) found in **$PdCl_2(L2)_2$** indicates that in the intramolecular complex, the 'natural' Pd–P bond length is not achievable due to steric constraints. These structural findings will be reflected in the intra- and intermolecular complexation energies, discussed further below in this section.

The structures of the intra- and intermolecular coordination of the bis-pyridine ligand **L3** to $PdCl_2$ are shown in Figs. 3.22 and 3.23. Selected structural parameters are listed in Table 3.17. Whereas in the minimum energy structure of **$PdCl_2L2$**, the two ester groups of the tether are oriented the same way with both C=O bonds pointing away from the C_{60} cage, this conformer is only a local minimum for **$PdCl_2L3$** (Fig. 3.22, right side). The structure with an up–down

Table 3.17. Selected bond lengths (pm) in the intramolecular complex **$PdCl_2L3$** and intermolecular complex **$PdCl_2(L3)_2$** at the BP86/def2-SV(P) level of theory. For the numbering of atoms refer to Figs. 3.22 and 3.23.

	$PdCl_2L3$	**$PdCl_2(L3)_2$**
Pd–N1	207.8	204.4
Pd–N2	208.2	205.2
Pd–Cl1	230.6	234.1
Pd–Cl2	230.6	235.8

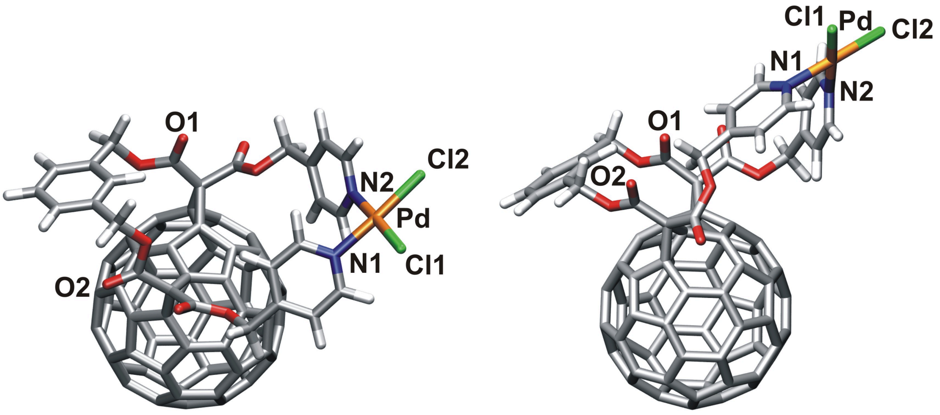

$PdCl_2L3$
±0.0

$PdCl_2L3$
+39.6

Figure 3.22. Intramolecular metal coordination of Pd(II) with the bis-pyridine C_{60} fullerene ligand **L3**, forming the complex **$PdCl_2L3$**. The minimum energy structure (left) with an up–down orientation of O1, O2 in the ester groups and a conformer with both O1, O2 pointing up (right) are displayed at the BP86/def2-SV(P) level (energies in kJ mol^{-1}).

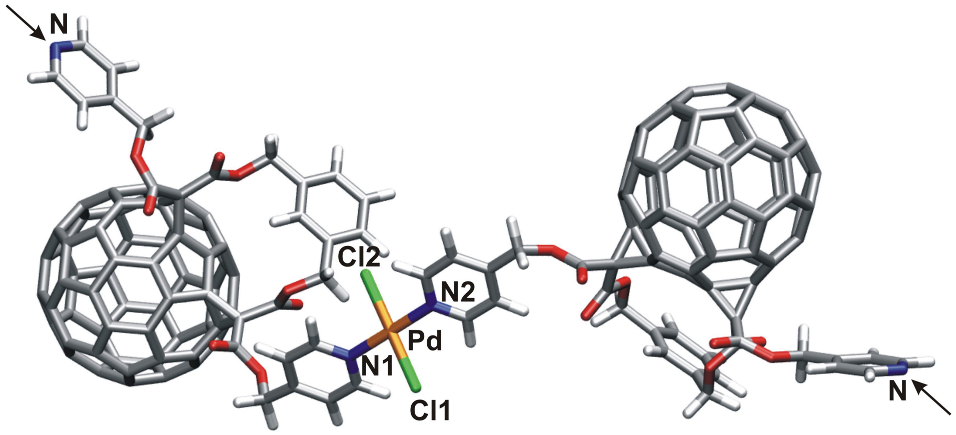

$PdCl_2(L3)_2$

Figure 3.23. Intermolecular metal coordination of Pd(II) with the bis-pyridine C_{60} fullerene ligand **L3**, forming the dimeric complex **$PdCl_2(L3)_2$**. The BP86/def2-SV(P) structure is displayed. The free coordination sites (N-pyridine) of the ligands for forming longer chains are indicated with arrows.

orientation of C=O1 and C=O2 in the ester groups of the tether, as displayed on the left panel of Fig. 3.22, is favoured by about 40 kJ mol^{-1}. The energy difference between a like and unlike orientation of the ester groups connecting the cage to the sticky sides (N-pyridine) is below 1 kJ mol^{-1}, an observation that can be attributed to a higher rotational flexibility in this area. Due to the sterically less demanding pyridine head groups (compared to triphenylphosphine), a square-planar complexation of the metal centre is found not only in the intermolecular *trans*-complex **PdCl$_2$(L3)$_2$**, but also in the intramolecular *cis*-complex **PdCl$_2$L3**. The Pd–N bonds in the *trans*-complex are shortened by 3–4 pm compared to the *cis*-complex, consequently elongating the Pd–Cl bonds by up to 5 pm (cf. Table 3.17). These opposite changes in bond lengths for the complexes of **L3** when comparing to the complexes of **L1** and **L2** are consistent with the *trans*-influence of the ligands, where chloride ranges in between pyridine and phosphine in the series.

The complexation energies for the intra- and intermolecular coordination of the functionalised fullerene ligands **L1**, **L2**, and **L3** to PdCl$_2$ calculated at the DFT level of theory are summarised in Table 3.18. The comparison between the BP86/def2-SV(P) and TPSS/def2-SV(P) results for the intramolecular complexation shows that the functional dependence of the complexation energy is marginal ($\leq$5%). The error in the complexation energy introduced by the use of a smaller basis set for the structure determination is less than 2%, as can be seen from the BP86/def2-TZVP//BP86/def2-SV(P) and BP86/def2-TZVP results. Therefore, only BP86/def2-TZVP//BP86/def2-SV(P) values will be discussed

Table 3.18. Complexation energies (kJ mol^{-1}) for the intra- and intermolecular coordination of the fullerene ligands **L1**, **L2** and **L3** to PdCl$_2$ forming the complexes PdCl$_2$L and PdCl$_2$(L)$_2$. The ΔE(inter−intra) values show the energetic preference of the intermolecular complexation for all ligands.

	PdCl$_2$L1	**PdCl$_2$(L1)$_2$**	**PdCl$_2$L2**	**PdCl$_2$(L2)$_2$**	**PdCl$_2$L3**	**PdCl$_2$(L3)$_2$**
BP86/def2-SV(P)	−290.4	−385.8	−281.6	−386.2	−313.2	−355.4
TPSS/def2-SV(P)	−301.1	–	−296.6	–	−324.3	–
BP86/def2-TZVP[a]	−277.1	−371.0	−260.4	−362.8	−298.6	−337.4
BP86/def2-TZVP	−272.6	–	–	–	–	–
ΔE(inter−intra)		−93.9		−102.3		−38.8

[a] BP86/def2-TZVP//BP86/def2-SV(P)

from now on. The intramolecular complexation energies for all three ligands **L1**, **L2**, and **L3** lie within 39 kJ mol^{-1} and range from -260 kJ mol^{-1} for **PdCl$_2$L2** to -299 kJ mol^{-1} for **PdCl$_2$L3**. Thus, the ligand **L3**, with its sterically less demanding pyridine coordination sites, forms the most stable intramolecular *cis*-complex with PdCl$_2$ among the three ligands tested. Furthermore, the intermolecular complexation energies for the three ligands lie within about 34 kJ mol^{-1}, but with **L3** now forming the weakest (-337 kJ mol^{-1}) and **L1** forming the strongest (-371 kJ mol^{-1}) intermolecular *trans*-complex with PdCl$_2$. Consequently, the intermolecular coordination of all three ligands **L1**, **L2**, and **L3** to PdCl$_2$ is energetically favourable with respect to the intramolecular coordination, but the energy separation ΔE(inter$-$intra) between **PdCl$_2$(L3)$_2$** and **PdCl$_2$L3** is the smallest found (a mere -38.8 kJ mol^{-1}). The ΔE(inter$-$intra) values evaluated for the ligands **L1** (-93.9 kJ mol^{-1}) and **L2** (-102.3 kJ mol^{-1}) bearing triphenylphosphine head groups are very similar, yet about 2.5 times larger than for **L3**.

Comparing this energetic sorting to the structural findings and to the concepts of the fullerene ligands' design discussed in the introduction, the following conclusions can be drawn. To favour the intermolecular coordination, the spatial requirements of the sticky sides directly influencing the coordination site play the most crucial role. Thus, sterically demanding head groups such as triphenylphosphine are able to suppress the undesired intramolecular *cis*-coordination. The conformational requisites introduced by the tether in the C$_{60}$ bis-adduct ligand **L2** enhance the preference for the intermolecular coordination by less than 10% compared to the mono-adduct **L1**. The employment of a larger tether that allows for the functionalisation of the cage at more spatially distanced sites could increase this preference dramatically.

3.5. Subvalent aluminium and magnesium compounds – on the diversity of metal–metal bonding

Low-valent metal compounds containing metal–metal bonds have gained increasing interest over the last decade.[184–186] The formation of these compounds requires the stabilisation of metal centres in low oxidation states. Most remarkable experimental achievements in this research field are the molecules with 2-electron-2-centre Zn–Zn and Mg–Mg bonds synthesised for the first time by Resa *et al.* and Green *et al.*, respectively.[187,188] The Mg(I) state in the crystalline $Mg_2R'_2$ species of Green *et al.* is stabilised by a bulky and thus sterically demanding anionic ligand that acts as protecting ligand and prevents the disproportionation reaction. The compound reveals a surprisingly high thermal stability but is consequently inert towards further reactions.

A fundamental understanding of the metal–metal bond formation needs to include side products and reactive intermediates that participate in a complex reaction process. The reactive intermediates are often radical species present in the elementary steps of chemical reactions when bonds are formed or cleaved. In a recent matrix isolation study, it was shown that the radical unit $[MgX]^\bullet$ spontaneously recombines in an exothermic reaction to form Mg_2X_2 dimers.[189] However, the radical species themselves, $[MgR]^\bullet$ or $[MgX]^\bullet$, have never been isolated as crystalline materials. The computational investigation of the Mg(I) oxidation state and the thermochemistry of Mg–Mg bonding can provide new insights that support synthesis strategies towards the so far unknown solid MgCl.

Aluminium in the oxidation state Al(II) is isoelectronic with Mg(I); both have one single valence electron occupying an s-orbital. Although the compounds Al_2R_4 ($R = CH(SiMe_3)_2$) and donor-stabilised $Al_2X_4{\cdot}2L$ (X = Cl, Br; L = ether or amine), corresponding to $Mg_2R'_2$ and Mg_2X_2, have been known for about 20 years now,[190–192] the $[AlR_2]^\bullet$ and $[AlX_2]^\bullet$ radical units have never been isolated thus far due to their high reactivity.

In a combined experimental and computational study at the University of Karlsruhe, Henke *et al.* and Pankewitz *et al.* report on the formation of Al_2R_4 ($R = PtBu_2$) and $Al_4R''_8$ ($R'' = OtBu$) compounds, the potential intermediates and reaction processes (for structures refer to Figs. 3.24 and 3.25).[193–195] A closed-shell 'butterfly' bicycle $RAl(\mu\text{-}R_2)AlR$ **1** (C_2 symmetry) with a short Al–Al bond of 258.7 pm and a four-membered ring $RAl(\mu\text{-}R_2)AlR$ **2** (C_i symmetry) with a nonbonding AlAl distance of 350.8 pm are experimentally observed. The relative energetic ordering of these compounds is presented along with hypothetical

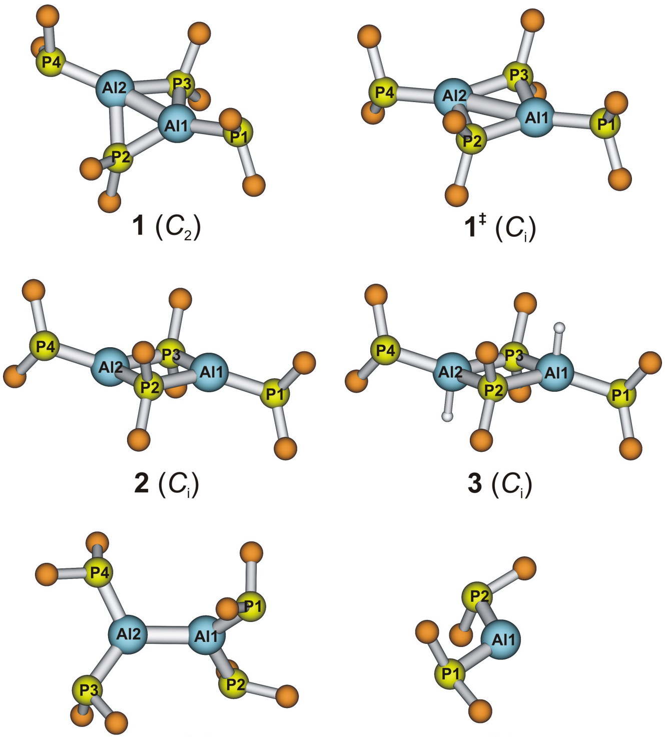
P4
Al2
P3
Al1
P1
P2
P4
Al2
P3
Al1
P1
P2
P4
Al2
P3
P2
Al1
P1
P4
Al2
P3
P2
Al1
P1
P4
Al2
Al1
P1
P3
P2
P2
Al1
P1

1 (C_2) **1**‡ (C_i)

2 (C_i) **3** (C_i)

4 (C_2) **5** (C_2)

Figure 3.24. Structures of the $Al_2(PtBu_2)_4$ isomers: the butterfly structure **1** (C_2 symmetry, ^1A), the TS **1**‡ (C_i symmetry) between the two equivalent butterfly structures, the triplet structure **2** (C_i symmetry, ^3A_u), the H-saturated isomer **3** (C_i symmetry, ^1A_g), the linear isomer **4** (C_2 symmetry, ^1A) and the radical fragment **5** (C_2 symmetry, ^2A). For clarity, only the tertiary carbons (orange) of the *t*Bu groups are shown.

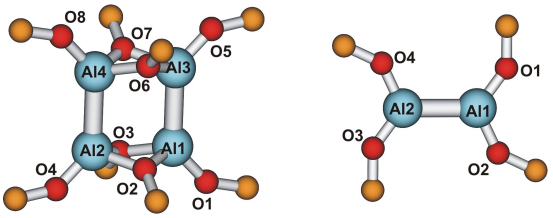
O8
O7
O5
Al4
O6
Al3
O3
Al2
Al1
O4
O2
O1
O4
O1
Al2
Al1
O3
O2

6 (D_2) **7** (C_{2h})

Figure 3.25. Structures of the dimer $(Al_2(OtBu)_4)_2$ **6** and the monomer **7**. For clarity, only the tertiary carbons (orange) of the *t*Bu groups are shown.

isomers and building units at the DFT computational level in Fig. 3.26. The combined experimental and computational results and considerations provide for the first time evidence that **2** is a biradical intermediate $RAl^{\uparrow}(\mu\text{-}R_2)Al^{\uparrow}R$

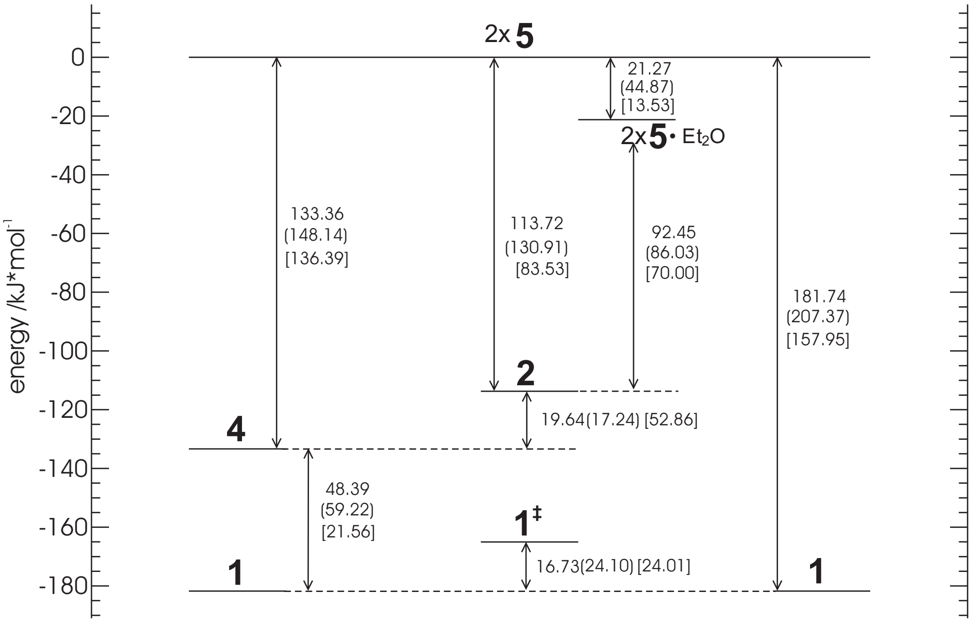

Figure 3.26. Relative electronic energies of the $Al_2(PtBu_2)_4$ isomers, the AlP_2tBu_4 fragment, and the TS $\mathbf{1}^{\ddagger}$ are given in kJ mol^{-1}. The diethyl ether stabilised radical of **5** is also shown. Values are at the BP86/def2-TZVP//BP86/def2-TZVP†, (TPSS/def2-TZVP//TPSS/def2-TZVP†) and [B3LYP/def2-TZVP//B3LYP/def2-TZVP†] levels.

(^3A_u state), isolated within an especially slow Al–Al bond formation process under very mild reaction conditions. The observed reactions are part of the disproportionation processes taking place in metastable AlX solutions.[192]

From these investigations it has become evident that in order to elucidate the Mg–Mg and Al–Al bond formation within the synthesis of Mg_2R_2 and Al_2R_4 species, it is necessary to invoke intermediates in which the ligands are engaged in versatile bonding motives, varying between terminal and bridging positions. Thus, the subhalides Al_2F_4, Al_2Cl_4 and dimerisation products thereof are computationally investigated as model compounds for the Al_2R_4 species in the following computational study. The fluorine and the larger chlorine atoms are chosen to tune the range of possible AlAl distances and thus increase the variety of potential structures. The structural diversity and the thermochemistry data of the aluminium bond formation shall be presented in this section. Furthermore, in analogy to the Al(II) compounds, isoelectronic Mg(I) species are also investigated. Based on the radical $[MgCl]^{\bullet}$ forming the dimer Mg_2Cl_2, the oligomerisation to larger clusters of MgCl is examined with respect to cluster structures, their disproportionation stability (to form solid magnesium metal and $MgCl_2$), and with respect to the formation of hypothetical solid MgCl.

The computational details are as follows. The aluminium compounds $(Al_2F_4)_x$ (**8**, **9a**–**9d**) and $(Al_2Cl_4)_x$ (**10**, **11a**–**11d**) with $x = 1, 2$ are optimised at the DFT level employing the functionals BP86 and B3LYP. A def2-TZVPP basis set and the corresponding auxiliary basis for the RI approximation are utilised.[66,86,87,163] Given that hard convergence criteria were required to obtain real minimum structures for the Al_2R_4 and $Al_4R''_8$ compounds, the same standards are applied to the model compounds. A fine integration grid (gridsize 4) and weight derivatives (cf. section 2.3.2) are used for the optimisations, with the final convergence criteria of 10^{-5} E_h/a_0 for the gradient norm and 10^{-8} E_h for the energy change. Harmonic vibrational frequencies are calculated analytically to confirm the minimum structures. Furthermore, a check for singlet and triplet instabilities in the wave function is conducted for each of these structures.[196] Enthalpies ΔH^0 (298 K) are evaluated by thermal correction of binding energies D_0 (0 K) using the module Freeh (ideal gas approximation). The D_0 values are obtained by zero point vibrational energy corrections (ZPVE) to the D_e values. MP2 single point energies are calculated for the B3LYP/def2-TZVPP optimal geometries utilising the module Ricc2. The calculations are carried out with an aug-cc-pwCVTZ basis set and employing the RI approximation with the corresponding auxiliary basis.[69–71,73,89–91,167] The frozen core is chosen as Al(1s), F(1s), and Cl(1s2s2p). The def2-QZVPP auxiliary basis set is used to approximate the Coulomb integrals and Hartree–Fock exchange in the RI-HF reference wave function calculations.[168–170] Thermal and ZPVE corrections to the MP2 energies are based on the unscaled B3LYP/def2-TZVPP vibrational frequencies.

A pool of relevant structures of the MgCl oligomers $(Mg_2Cl_2)_2$ and $(Mg_2Cl_2)_4$ has been created using a genetic algorithm (GA) approach within the DFT framework (TPSS/def-TZVP).[197,198] Starting with 30 initial structures for $(Mg_2Cl_2)_2$, a number of 20 child structures is generated in each of the 40 generations also including mutation. For $(Mg_2Cl_2)_4$, 40 initial structures are used to produce a number of 25 child structures over 100 generations. The set of initial structures for $(Mg_2Cl_2)_4$ is seeded with the five stable isomers of $(Mg_2Cl_2)_2$ that have been found in the previous GA run. From the resulting structures of the GA, the ones in a 60–80 kJ mol^{-1} range are selected and reoptimised at the BP86, TPSS, and B3LYP levels employing the same basis sets, grids and convergence criteria as described for the Al_2X_4 compounds (see above). The minimum structures are confirmed by vibrational frequency calculations. The aug-cc-pCVTZ basis set is used for the RI-HF reference and the MP2 and CCSD(T) energy calculations at the B3LYP/def2-TZVPP optimal geometries.[71,73,170,199] The auxiliary basis sets cc-pV5Z for Mg and aug-cc-pwCV5Z for Cl are utilised in the RI approximation in MP2.[91] Both, MP2 and CCSD(T) calculations are performed with a Mg(1s), F(1s), and Cl(1s2s2p) frozen core. Again, the thermal and ZPVE corrections to the MP2 and CCSD(T) energies are based on unscaled B3LYP/def2-TZVPP vibrational frequencies.

3.5.1. Isomers of Al_2F_4 and Al_2Cl_4 – model compounds for Al_2R_4 species

The isomers of Al_2F_4 **9a–9d** and Al_2Cl_4 **11a–11d** and their respective dimers, $(Al_2F_4)_2$ **8** and $(Al_2Cl_4)_2$ **10**, mutually show the two binding motives of ligand-bridged and directly σ-bonded aluminium centres. The structures of the monomeric isomers and the dimers are displayed in Figs. 3.27 and 3.28 along with the structural parameters in Tables 3.19 and 3.20. The calculated model compound dimers $(Al_2F_4)_2$ **8** and $(Al_2Cl_4)_2$ **10** show an analogous structure to the experimentally observed tetranuclear compound $(Al_2(OtBu)_4)_2$ **6**. Due to the sterically simpler ligands (F, Cl compared to O*t*Bu) an ideal D_{2h} symmetry with

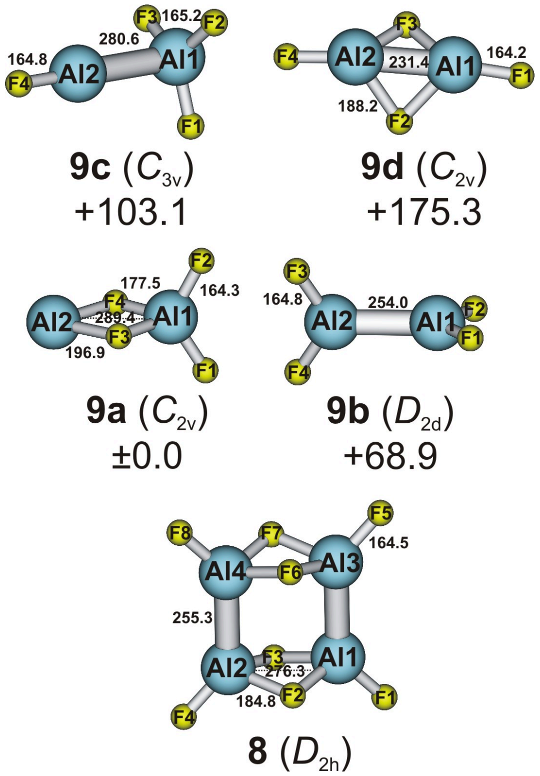
F3
165.2
F2
280.6
164.8
Al2
Al1
F4
F1
F3
F4
Al2
231.4
Al1
164.2
F1
188.2
F2
F2
177.5
164.3
F4
Al2
289.4
Al1
F3
196.9
F1
F3
164.8
254.0
Al2
Al1
F2
F1
F4
F5
F8
F7
164.5
Al4
F6
Al3
255.3
F3
Al1
Al2
276.3
184.8
F2
F4
F1

9c (C_{3v}) +103.1

9d (C_{2v}) +175.3

9a (C_{2v}) ±0.0

9b (D_{2d}) +68.9

8 (D_{2h})

Figure 3.27. Geometries of the dimer $(Al_2F_4)_2$ **8** and the isomeric monomers of Al_2F_4 **9a–d**. Given bond distances (pm) and relative energies (kJ mol^{-1}) are calculated at the B3LYP/def2-TZVPP level of theory.

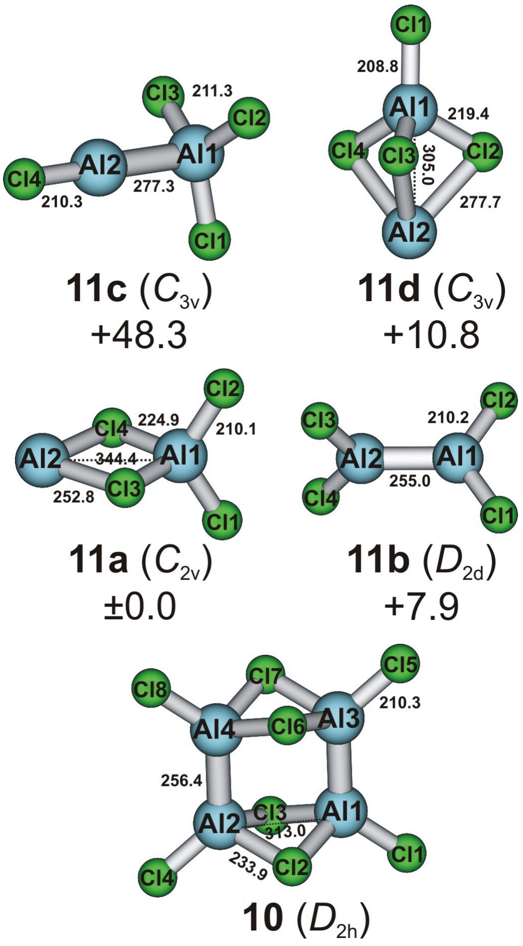
Cl3
211.3
Cl2
Cl4
Al2
Al1
210.3
277.3
Cl1
Cl1
208.8
Al1
219.4
Cl4
Cl3
305.0
Cl2
277.7
Al2
Cl2
Cl4
224.9
210.1
Al2
344.4
Al1
Cl3
252.8
Cl1
Cl3
210.2
Cl2
Al2
Al1
255.0
Cl4
Cl1
Cl5
Cl8
Cl7
210.3
Al4
Cl6
Al3
256.4
Cl3
Al1
Al2
313.0
Cl1
233.9
Cl2
Cl4

11c (C_{3v}) +48.3

11d (C_{3v}) +10.8

11a (C_{2v}) ±0.0

11b (D_{2d}) +7.9

10 (D_{2h})

Figure 3.28. Geometries of the dimer $(Al_2Cl_4)_2$ **10** and the isomeric monomers of Al_2Cl_4 **11a–d**. Given bond distances (pm) and relative energies (kJ mol^{-1}) are calculated at the B3LYP/def2-TZVPP level of theory.

all four metal centres in a plane (σ_h) is realised in **8** and **10**, whereas a slight distortion from planarity was observed in compound **6** reducing the symmetry to D_2. Formally, the dimer structures can be interpreted either as two butterfly monomers, *i.e.* **9d**, connected by Al–Al σ bonds or as the dimerisation products of two Al–Al σ-bonded linear monomers (*i.e.* **9b** and **11b**, respectively), where two of the former four terminal halide ligands take bridging positions. The nonbonding AlAl distances (Al1Al2 and Al3Al4) in **8** (**10**) are 276.3 (313.0) pm, compared to a distance of 255.3 (256.4) pm for the Al–Al σ bonds. In comparison to the linear monomers **9b** (**11b**), the Al–Al σ bond is elongated by about 1.3 pm upon dimerisation (B3LYP/def2-TZVPP). The observed corresponding Al–Al bond elongation in $(Al_2(OtBu)_4)_2$ **6** of 6.4 pm with respect to the linear

Table 3.19. Structural parameters of the compounds $(Al_2F_4)_2$ **8** and $(Al_2Cl_4)_2$ **10** calculated at the BP86/def2-TZVPP and B3LYP/def2-TZVPP levels (cf. Figs. 3.27 and 3.28 for numbering of atoms). Selected bond lengths (pm) and bond angles (°) are given. X denotes F or Cl.

	8		**10**	
	BP86	B3LYP	BP86	B3LYP
Al1–Al2	276.2	276.3	309.5	313.0
Al1–Al3	255.5	255.3	256.9	256.4
Al1–X1	165.7	164.5	210.9	210.3
Al1–X2	186.2	184.8	234.0	233.9
Al1–X2–Al2	95.7	96.7	82.8	84.0
X2–Al1–X3	79.5	78.9	88.0	87.3
X1–Al1–Al2	136.3	137.3	129.1	129.8

monomer **7** is much more pronounced due to the bulky ligand. This sterical influence of the ligands on the structure is also the reason why no dimerisation for the $Al_2(PtBu_2)_4$ compounds was observed.[193,195] The most stable Al_2F_4 monomer is isomer **9a** (C_{2v} symmetry, $^1A_1$ state) in which two fluorine atoms are terminally bound to one of the aluminium atoms. The other two remaining fluorine atoms asymmetrically bridge the first to the second aluminium centre. This leads to a very long nonbonding metal–metal distance of 289.4 pm compared to 276.3 pm in the more rigid dimer (B3LYP/def2-TZVPP). Formally, this isomer **9a** can be considered as composed of an $[Al(III)F_4]^-$ anion and an $[Al(I)]^+$ cation. The calculated charges of a natural population analysis (NPA)[200] are $+2.16\,e$ on Al1, $+0.87\,e$ on Al2, and $-0.74\,e$ on F1/2 and $-0.78\,e$ on F2/3, supporting this interpretation, yet revealing a covalent contribution of about 30% (for NPA charges refer to Table 3.21). The linear isomer **9b** (D_{2d} symmetry, $^1A_1$ state) is about 73 kJ mol^{-1} higher in energy than **9a** (MP2/aug-cc-pwCVTZ). The isomer shows a direct Al–Al σ bond of 254 pm, with the four fluoride ligands terminally bound to the aluminium centres in a staggered conformation. The charge on both aluminium centres is $+1.50\,e$. About 36 kJ mol^{-1} (MP2/aug-cc-pwCVTZ) above **9b** lies the isomer **9c** (C_{3v} symmetry, $^1A_1$ state). This isomer formally comprises an $Al(III)F_3$ and an Al(I)F unit that are connected via a largely ionogenic Al–Al bond. The calculated NPA charges of $+1.97\,e$ on Al1, $-0.75\,e$ on F1,

Table 3.20. Structural parameters of the monomeric isomers of Al_2F_4 **9a–d** and Al_2Cl_4 **11a–d** calculated at the BP86/def2-TZVPP and B3LYP/def2-TZVPP levels (cf. Figs. 3.27 and 3.28 for numbering of atoms). Selected bond lengths (pm) and bond angles (°) are given. X denotes F or Cl.

	Al_2F_4		Al_2Cl_4	
	BP86	B3LYP	BP86	B3LYP
	9a		**11a**	
Al1–Al2	289.9	289.4	341.9	344.4
Al1–X1	165.4	164.3	210.9	210.1
Al1–X3	179.1	177.5	225.5	224.9
Al2–X3	197.7	196.9	251.0	252.8
Al1–X3–Al2	100.5	101.1	91.5	92.1
X1–Al1–X2	121.1	120.9	119.5	119.1
X3–Al1–X4	84.2	83.8	94.4	94.5
X3–Al2–X4	74.8	74.0	82.5	81.5
	9b		**11b**	
Al1–Al2	254.7	254.0	255.5	255.0
Al1–X1	166.0	164.8	210.8	210.2
X1–Al1–Al2	120.6	120.8	121.0	121.1
X1–Al1–X2	118.9	118.3	118.1	117.9
	9c		**11c**	
Al1–Al2	277.0	280.6	273.2	277.3
Al1–X1	166.5	165.2	212.0	211.3
Al2–X4	166.0	164.8	211.1	210.3
X1–Al1–X2	118.4	118.3	117.6	117.5
X1–Al1–Al2	97.5	97.8	99.5	99.2
	9d			
Al1–Al2	233.1	231.4	–	
Al1–X1	165.5	164.2		
Al1–X2	189.9	188.2		
Al1–X2–Al2	75.7	75.9		
X1–Al1–Al2	166.9	166.7		
			11d	
Al1–Al2	–		300.8	305.0
Al1–X1			209.2	208.8
Al1–X2			220.0	219.4
Al2–X2			273.9	277.7
Al1–X2–Al2			74.1	74.7
X1–Al1–X2			118.8	118.6

Table 3.21. Atomic charges based on the natural population analysis (NPA) for the different isomers of Al_2F_4 and Al_2Cl_4, obtained at the B3LYP/def2-TZVPP level (X denotes F or Cl). Charges are in units of *e*.

	Al_2F_4				Al_2Cl_4			
	9a	**9b**	**9c**	**9d**	**11a**	**11b**	**11c**	**11d**
Al1	+2.160	+1.500	+1.971	+1.490	+1.426	+1.045	+1.153	+1.386
Al2	+0.869	+1.500	+1.080	+1.490	+0.756	+1.045	+1.021	+0.741
X1	−0.738	−0.750	−0.751	−0.744	−0.522	−0.522	−0.521	−0.501
X2	−0.738	−0.750	−0.751	−0.746	−0.522	−0.522	−0.521	−0.542
X3	−0.777	−0.750	−0.751	−0.746	−0.569	−0.522	−0.521	−0.542
X4	−0.777	−0.750	−0.799	−0.744	−0.569	−0.522	−0.611	−0.542

F2, and F3, $+1.08\,e$ on Al2, and $-0.80\,e$ on F4 together with a long Al–Al bond distance of 280.6 pm support this interpretation. The butterfly isomer **9d** (C_{2v} symmetry, $^1A_1$ state) is very unstable with respect to the isomers discussed so far, showing a large dimerisation enthalpy of $-450.5\,\mathrm{kJ\,mol^{-1}}$ (B3LYP/def2-TZVPP, cf. Table 3.22). This butterfly structure is a minimum only on the B3LYP potential energy surface. The Al–Al σ bond distance of 231.4 pm is extremely short when compared to the distances observed in the other structures, which range from 254.0 pm in **9b** to 255.3 pm in **8**. At the BP86 level, the butterfly structure is a saddle point (*i.e.*, it displays one imaginary frequency). The restricted Hartree–Fock solution for **9d** reveals a triplet instability that explains the large deviation of the MP2 dimerisation enthalpy from the DFT results observed for this isomer (cf. Table 3.22).

Despite the larger and more polarisable chloride ligand (with respect to fluoride) the Al_2Cl_4 isomers **11a–11d** and the $(Al_2Cl_4)_2$ dimer **10** show very similar structures and binding motives when compared to their counterparts with fluoride. Nevertheless, there are a few differences to be noted. Firstly, all Al_2Cl_4 isomers lie energetically much closer together (within a $60\,\mathrm{kJ\,mol^{-1}}$ range) than the Al_2F_4 isomers. Secondly, whereas the butterfly structure **9d** is found for Al_2F_4 at the B3LYP/def2-TZVPP level, it is not stable with the chloride ligand. The very short Al–Al distance of this butterfly structure is not feasible for chloride. Third, besides the structure **11a** (C_{2v} symmetry, $^1A_1$ state) there exists another structure with the $[Al(III)Cl_4]^-$ $[Al(I)]^+$ motif a mere $5\,\mathrm{kJ\,mol^{-1}}$ higher in energy, that is, isomer **11d** with C_{3v} symmetry ($^1A_1$ state). This C_{3v} isomer corresponds to the ex-

Table 3.22. Calculated reaction enthalpies ΔH_r^0 (298 K) for the dimerisation reaction of the isomeric monomers **9a–d** and **11a–d** ($2\,Al_2F_4 \rightarrow (Al_2F_4)_2$ and $2\,Al_2Cl_4 \rightarrow (Al_2Cl_4)_2$, respectively) at the BP86/def2-TZVPP, B3LYP/def2-TZVPP, and MP2/aug-cc-pwCVTZ levels of theory. Enthalpies are in kJ mol^{-1}.

	$2\,Al_2F_4 \rightarrow (Al_2F_4)_2$				$2\,Al_2Cl_4 \rightarrow (Al_2Cl_4)_2$			
	9a	**9b**	**9c**	**9d**	**11a**	**11b**	**11c**	**11d**
BP86	−123.1	−239.9	−311.6	−415.4	−141.0	−159.3	−236.4	−148.5
B3LYP	−99.9	−237.7	−306.1	−450.5	−112.6	−128.4	−209.1	−134.1
MP2	−241.0	−386.8	−458.1	−725.8	−174.4	−227.4	−296.5	−183.7

perimentally known structures of $GaGaCl_4$ and $KAlCl_4$ in the gas phase.[201–203] The calculated atomic charges for the isomers **11a** and **11d** are comparable (cf. Table 3.21), whereas the bridged AlAl distance of 305.0 pm in **11d** is almost 40 pm shorter than in **11a**.

The effects of the different ligands (Cl compared to F) on the dimer structures $(Al_2Cl_4)_2$ **10** and $(Al_2F_4)_2$ **8** are marginal. A slight elongation of the direct Al–Al σ bonds ($\sim$1 pm) is found for the dimer with chloride ligands. As expected, the NPA shows an increased covalent contribution for the chloride ligands in comparison with fluoride. The same elongation of the direct Al–Al σ bond is also observed for the monomeric isomer Al_2Cl_4 **11b** when compared to Al_2F_4 **9b**.

3.5.2. Oligomeric clusters of Mg_2Cl_2

Upon removing the terminal chloride ligands from the dimer $(Al_2Cl_4)_2$ **10** described in the previous section, one ends up with the stable ionic compound $(Al_2Cl_2)_2^{4+}$ **14** (D_{2h} symmetry, ^1A_g state). This ionic Al(II) compound **14** is isoelectronic and isostructural to the corresponding neutral magnesium compound $(Mg_2Cl_2)_2$ **12d**, where all magnesium centres have the rare oxidation state of Mg(I). Structures and structural parameters of **12d** and **14** are displayed together with the monomeric isomers **13a** and **13b** in Fig. 3.29 and Table 3.23. Similar to $(Al_2X_4)_2$ and $(Al_2(OtBu)_4)_2$, the tetranuclear compound **12d** shows two long, nonbonding MgMg distances (303.8 pm) and two σ-bonded metal centres with a short bond distance of 281.8 pm. This Mg–Mg σ bond is elongated by 2 pm with respect to the corresponding bond in the linear monomer **13a** ($D_{\infty h}$ symmetry, $^1\Sigma_g^+$ state). The two magnesium centres in the rhombic monomer **13b** (D_{2h} symmetry, ^1A_g state) are bridged by two chloride ligands, giving rise to a large

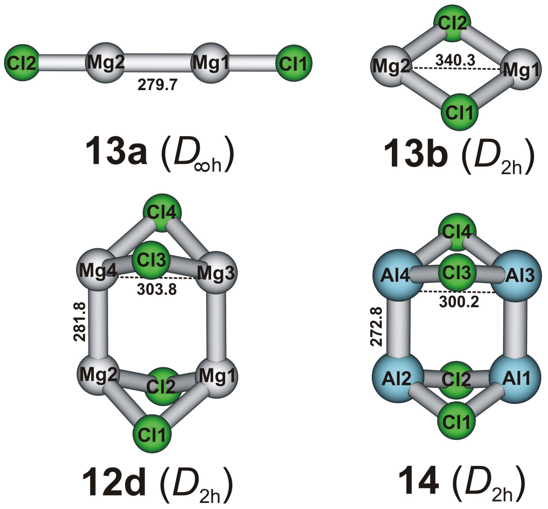
Cl2
Mg2
Mg1
Cl1
279.7
Cl2
Mg2
340.3
Mg1
Cl1
Cl4
Mg4
Cl3
Mg3
303.8
281.8
Mg2
Cl2
Mg1
Cl1
Cl4
Al4
Cl3
Al3
300.2
272.8
Al2
Cl2
Al1
Cl1

13a ($D_{\infty h}$) **13b** (D_{2h})

12d (D_{2h}) **14** (D_{2h})

Figure 3.29. Geometries of $(Mg_2Cl_2)_2$ **12d** and the isomeric monomers Mg_2Cl_2 **13a–b**. The isoelectronic ion $(Al_2Cl_2)_2^{4+}$ **14** is also given. Metal–metal distances (pm) in the different compounds are calculated at the B3LYP/def2-TZVPP level of theory.

Table 3.23. Structural parameters for $(Mg_2Cl_2)_2$ **12d**, the isoelectronic ion $Al_4Cl_4^{4+}$ **14**, and the monomeric isomers Mg_2Cl_2 **13a–b** (cf. Fig. 3.29 for numbering of atoms). Selected bond lengths (pm) and bond angles (°) are at the BP86/def2-TZVPP and B3LYP/def2-TZVPP levels of theory.

	BP86	B3LYP	BP86	B3LYP
	13a		**13b**	
Mg1–Mg2	281.1	279.7	337.1	340.3
Mg1–Cl1	221.5	220.8	247.8	240.3
Mg1–Cl1–Mg2	0.0	0.0	85.7	90.1
Cl1–Mg1–Cl2	180.0	180.0	94.3	89.9
	12d		**14**	
M1–M2	300.5	303.8	299.1	300.2
M1–M3	282.7	281.8	274.7	272.8
M1–Cl1	245.6	245.2	229.0	228.2
M1–Cl1–M2	75.4	76.6	81.6	82.3
Cl1–M1–Cl2	87.7	87.3	89.7	89.2

nonbonding MgMg distance of 340.3 pm. Compound **13b** is a minimum only with respect to nuclear degrees of freedom. The restricted DFT (BP86, B3LYP) as well as the restricted Hartree–Fock solutions show a triplet instability.
The GA search on the $(Mg_2Cl_2)_2$ potential energy surface reveals that compound **12d** is not the most stable isomer. Two 2D-chain structures, **12a** and **12b**, and a 3D-cage isomer **12c** are lower in energy than **12d** at the BP86, TPSS, MP2, and CCSD(T) levels (for structures and structural parameters refer to Fig. 3.30).

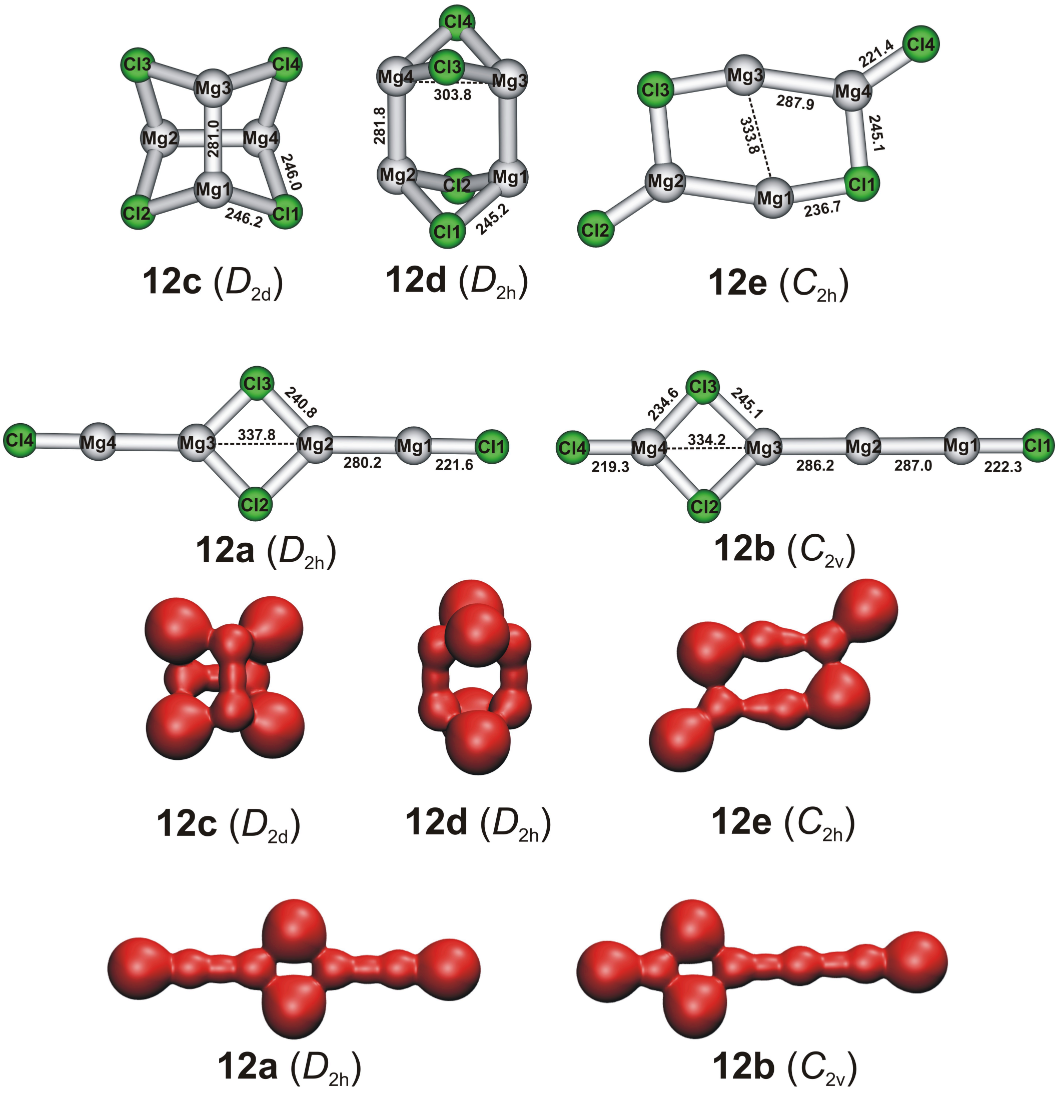
Cl3
Cl4
Mg3
Mg2
Mg4
281.0
246.0
Mg1
Cl2
246.2
Cl1
Cl4
Mg4
Cl3
Mg3
303.8
281.8
Mg2
Cl2
Mg1
Cl1
245.2
Cl4
221.4
Cl3
Mg3
Mg4
287.9
333.8
245.1
Mg2
Mg1
Cl1
236.7
Cl2
Cl3
240.8
Cl4
Mg4
Mg3
337.8
Mg2
Mg1
Cl1
280.2
221.6
Cl2
234.6
Cl3
245.1
Cl4
Mg4
334.2
Mg3
Mg2
Mg1
Cl1
219.3
286.2
287.0
222.3
Cl2

12c (D_{2d}) **12d** (D_{2h}) **12e** (C_{2h})

12a (D_{2h}) **12b** (C_{2v})

12c (D_{2d}) **12d** (D_{2h}) **12e** (C_{2h})

12a (D_{2h}) **12b** (C_{2v})

Figure 3.30. Structures of the five identified $(Mg_2Cl_2)_2$ isomers **12a–e** in a 25–60 kJ mol^{-1} range (depending on the method and functional). Bond distances (pm) are obtained at the B3LYP/def2-TZVPP level. Total electron density plots for all isomers are also included (isosurfaces with isovalue at 0.022 a_0^{-3}).

The most stable isomer identified is the highly symmetric chain structure **12a** (D_{2h} symmetry, ^1A_g state), where two ClMg(I)Mg(I) units are symmetrically bridged by two chloride ligands, resulting in a nonbonding MgMg distance of 337.8 pm. The two Mg–Mg σ bonds, both 280.2 pm, are marginally elongated with respect to the linear monomer **13a**. About 16–18 kJ mol^{-1} higher in energy, a chain structure with lower symmetry, **12b** (C_{2v} symmetry, $^1A_1$ state), is found. Formally, this structure consists of ClMg(II) and ClMg(I)Mg(0)Mg(I) units that are bridged by two chloride ligands. In the Mg(I)Mg(0)Mg(I) sequence the σ bonds differ slightly from each other by 0.8 pm (286.2 and 287.0 pm, respectively) and are strongly elongated by about 7 pm with respect to the linear monomer. Isomer **12c** (D_{2d} symmetry, $^1A_1$ state) is the most stable cage structure observed. The Mg–Mg bonds are rotated by 90° with respect to each other, exhibiting a bond distance of 281.0 pm, that is, 0.8 pm shorter than in the highly symmetric isomer **12d**. Isomer **12e** (C_{2h} symmetry, ^1A_g state) has a planar ring structure with a long Mg–Mg bond of 287.9 pm. Two magnesium centres of this isomer are in the formal oxidation state of $+1.5$, while the two other metal centres possess the formal oxidation state of $+0.5$.

Total electron density plots at the B3LYP/def2-TZVPP level are displayed for all $(Mg_2Cl_2)_2$ isomers **12a–e** along with the structures to illustrate the different bonding situations (cf. Fig. 3.30). The assignment of bonds in the structures is based on bond distances and the total electron density plots. Taking into account the covalent contributions to the Mg–Cl bonds, the calculated atomic charges of a natural population analysis confirm for all $(Mg_2Cl_2)_2$ isomers the formal oxidation states assigned to the metal centres (cf. Table 3.24).

All $(Mg_2Cl_2)_2$ isomers **12a–e** lie within a 26–32 kJ mol^{-1} range at the BP86, TPSS, MP2, and CCSD(T) levels. Only at the B3LYP level this range broadens to about 56 kJ mol^{-1}. The energetic ordering of the individual isomers varies depending on the different functionals, though all of them confirm **12a** as the global minimum structure, in agreement with the MP2 and CCSD(T) results.

The relative stabilities of the $(Mg_2Cl_2)_2$ isomers depending on the method are as follows (values in kJ mol^{-1}):

BP86: **12a** $<$ **12b** (15.9) $<$ **12c** (23.5) $<$ **12e** (26.5) $<$ **12d** (29.2)

TPSS: **12a** $<$ **12c** (10.9) $<$ **12b** (16.7) $<$ **12d** (19.4) $<$ **12e** (26.3)

B3LYP: **12a** $<$ **12b** (16.9) $<$ **12e** (38.8) $<$ **12d** (53.2) $<$ **12c** (56.4)

MP2: **12a** $<$ **12b** (17.8) $<$ **12c** (19.3) $<$ **12d** (20.5) $<$ **12e** (31.7)

CCSD(T): **12a** $<$ **12b** (16.1) $<$ **12c** (27.0) $<$ **12d** (27.6) $<$ **12e** (31.6)

Table 3.24. Atomic charges based on a natural population analysis (NPA) for the $(Mg_2Cl_2)_2$ isomers **12a–e** calculated at the B3LYP/def2-TZVPP level. Charges are in units of *e*.

	$(Mg_2Cl_2)_2$				
	12a	**12b**	**12c**	**12d**	**12e**
Mg1	+0.848	+0.715	+0.850	+0.858	+0.535
Mg2	+0.862	+0.294	+0.850	+0.858	+1.162
Mg3	+0.862	+0.727	+0.850	+0.858	+0.535
Mg4	+0.848	+1.638	+0.850	+0.858	+1.162
Cl1	−0.855	−0.863	−0.850	−0.858	−0.847
Cl2	−0.855	−0.842	−0.850	−0.858	−0.849
Cl3	−0.855	−0.842	−0.850	−0.858	−0.848
Cl4	−0.855	−0.828	−0.850	−0.858	−0.849

The GA search of the $(Mg_2Cl_2)_4$ potential energy surface yields the structural isomers **15a–f** showing a large variety of bonding motives (cf. Figs. 3.31 and 3.32). Note that the assignment of bonds in the presented structures is based again on the distances and the total electron density plots. In these $(Mg_2Cl_2)_4$ isomers, metal centres in different formal oxidation states are found, as was already observed for the smaller $(Mg_2Cl_2)_2$ compounds. Whereas some of the $(Mg_2Cl_2)_4$ isomers are purely built from σ-bonded Mg_2^{2+} units that are bridged by chloride ligands, and thus only have Mg(I) metal centres (*i.e.* **15a** and **15b**), others exhibit magnesium centres in mixed oxidation states formally ranging from Mg(0) to Mg(II) (*i.e.* **15c–f**). The latter may be interpreted as internal disproportionation of Mg(I) centres already occurring in these small to medium sized clusters, resulting in isolated magnesium centres with formal oxidation states between +1 and +2, and 'metal rich' units (*e.g.* the Mg(I)Mg(0)Mg(I) sequence found in the isomers **15c** and **15e**). This interpretation is supported by the calculated NPA charges for the different magnesium centres (cf. Table 3.25). However, the NPA charges also reveal that the assignment of bonds and bonding partners based on atom–atom distances and the total electron densities is not unambiguous for some of the larger clusters (as will be discussed along with the individual clusters). The simple picture of the formal oxidation states does not work in these cases for explaining the complex bonding situation.

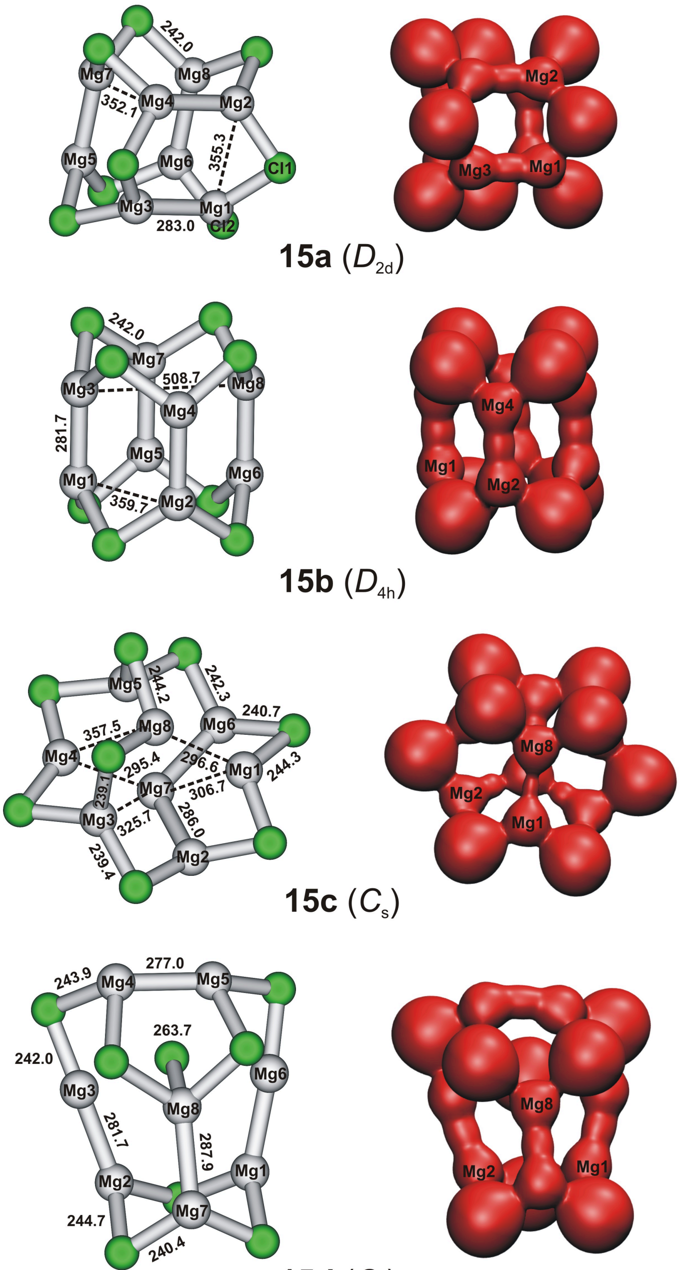
242.0
Mg7
Mg8
352.7
Mg4
Mg2
Mg5
Mg6
355.3
Cl1
Mg3
Mg1
283.0
Cl2
Mg2
Mg3
Mg1
242.0
Mg7
508.7
Mg3
Mg8
Mg4
281.7
Mg5
Mg1
Mg6
359.7
Mg2
Mg4
Mg1
Mg2
Mg5
244.2
242.3
240.7
357.5
Mg8
Mg6
Mg4
295.4
296.6
Mg1
244.3
239.1
Mg7
306.7
Mg3
325.7
286.0
239.4
Mg2
Mg8
Mg2
Mg1
243.9
277.0
Mg4
Mg5
263.7
242.0
Mg6
Mg3
Mg8
281.7
287.9
Mg1
Mg2
244.7
Mg7
240.4
Mg8
Mg2
Mg1

15a (D_{2d})

15b (D_{4h})

15c (C_s)

15d (C_s)

Figure 3.31. Geometries (left) of four out of six identified $(Mg_2Cl_2)_4$ isomers **15a–f** in a 45–80 kJ mol^{-1} range (depending on the method and functional). Bond distances (pm) are obtained at the B3LYP/def2-TZVPP level. Total electron density plots are given for each isomer on the right (isosurfaces with isovalue at 0.022 a_0^{-3}).

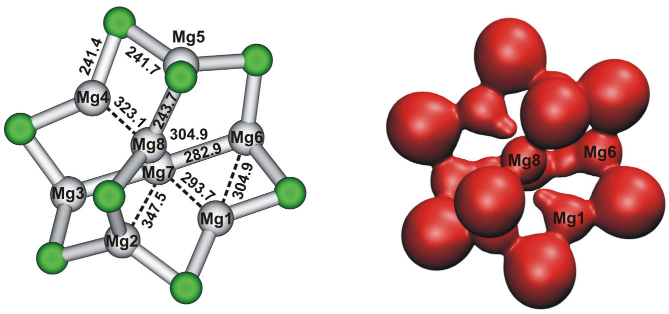
Mg5
241.4
241.7
Mg4
323.1
243.7
304.9
Mg8
282.9
Mg6
Mg7
293.7
304.9
Mg3
347.5
Mg1
Mg2
Mg8
Mg6
Mg1

15e (C_2)

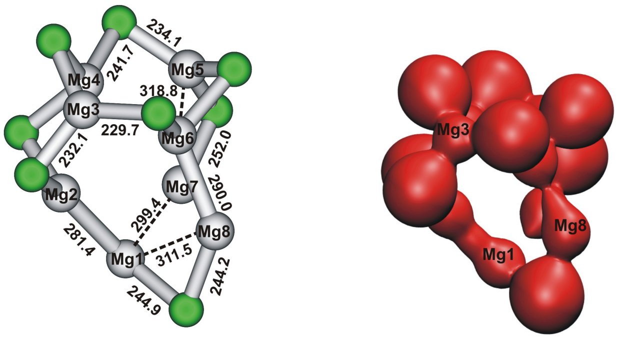
234.1
241.7
Mg4
Mg5
318.8
Mg3
229.7
Mg6
252.0
232.1
Mg7
290.0
Mg2
299.4
Mg8
281.4
Mg1
311.5
244.2
244.9
Mg3
Mg8
Mg1

15f (C_1)

Figure 3.32. Geometries (left) of two out of six identified $(Mg_2Cl_2)_4$ isomers **15a–f** in a 45–80 kJ mol^{-1} range (depending on the method and functional). Bond distances (pm) are obtained at the B3LYP/def2-TZVPP level. Total electron density plots are given for each isomer on the right (isosurfaces with isovalue at 0.022 a_0^{-3}).

Isomer **15a** (D_{2d} symmetry, $^1A_1$ state) structurally consists of two Mg_4Cl_2 hexagons that are rotated by 90° with respect to each other and connected by bridging chloride ligands. At about 12 kJ mol^{-1} (MP2/aug-cc-pCVTZ) above **15a** resides the related high symmetry isomer **15b** (D_{4h} symmetry, $^1A_{1g}$ state) that is composed of the two Mg_4Cl_2 hexagons connected in a coplanar orientation. All metal centres of both isomers are Mg(I) centres in agreement with the calculated NPA charges. However, at the BP86, TPSS, and MP2 levels, two star-shaped isomers possessing either a mirror plane σ_v or a C_2 rotational axis, **15c** (C_s symmetry, ^1A state) and **15e** (C_2 symmetry, ^1A state), are the most stable isomers, with **15c** favoured by 6–8 kJ mol^{-1} over **15e**. Both structures possess, apart from three isolated Mg(I) centres, two magnesium centres in the formal oxidation state of +1.5 and a Mg(I)Mg(0)Mg(I) unit. This formal description is affirmed by the calculated NPA charges of the magnesium centres (cf. Table 3.25). While a distance of 282.9 pm is found for the Mg–Mg bonds in the linear Mg(I)Mg(0)Mg(I)

Table 3.25. Atomic charges on the magnesium centres of the different $(Mg_2Cl_2)_4$ isomers **15a–f** based on a natural population analysis (NPA) (B3LYP/def2-TZVPP level). Charges are in units of e.

	$(Mg_2Cl_2)_4$					
	15a	**15b**	**15c**	**15d**	**15e**	**15f**
Mg1	+0.856	+0.857	+0.887	+0.888	+0.932	+0.571
Mg2	+0.856	+0.857	+0.933	+0.888	+1.303	+0.791
Mg3	+0.856	+0.857	+1.301	+0.832	+0.938	+1.578
Mg4	+0.856	+0.857	+0.979	+0.873	+0.932	+0.990
Mg5	+0.856	+0.857	+1.301	+0.873	+1.303	+1.534
Mg6	+0.856	+0.857	+0.933	+0.832	+0.938	+0.428
Mg7	+0.856	+0.857	−0.309	+0.903	−0.227	+0.314
Mg8	+0.856	+0.857	+0.649	+0.812	+0.546	+0.479

sequence of **15e**, this distance is elongated by about 3 pm (to 286.0 pm) in the angled Mg(I)Mg(0)Mg(I) sequence of **15c**.

Isomer **15d** (C_s symmetry, ^1A state) is destabilised by 64.1 kJ mol^{-1} at the MP2 level. This structure is, besides isomer **15f**, an example where the assignment of some of the bonding partners is not definite, and thus the assignment of formal oxidation states for the metal centres ceases to be useful. The calculated NPA charges on all magnesium centres are $+0.81\,e$ to $+0.90\,e$, thus suggesting the presence of Mg(I) centres, as these NPA charges are very similar to the values observed in **15a** and **15b**. One σ-bonded Mg(I)Mg(I) unit (as discussed for the isomers **15a** and **15b**) with a very short Mg–Mg distance of 277.0 pm (Mg4–Mg5) can be identified in the structure. Furthermore, a chloride add-ligand is located in the cavity that the magnesium centres span in isomer **15d**. Although Mg8 is the closest metal centre in a distance of 263.7 pm to this add-ligand, the NPA does not show an increased positive charge on this magnesium centre. Nevertheless, the Mg7–Mg8 bond is elongated by 10–11 pm with respect to the aforementioned σ bond Mg4–Mg5. A Mg–Mg bond distance of 281.7 pm is found for Mg2–Mg3 and Mg1–Mg6. In summary, three dissimilar Mg–Mg bond distances, differing by up to 11 pm in a range of 277.0–287.9 pm, are observed for magnesium centres that should have similar atomic charges according to the NPA. The C_1 isomer **15f** (^1A state) exhibits a similarly complicated bonding of Mg(I)Mg(<I) units and

of isolated magnesium centres in oxidation states between +1 and +1.5. These findings demonstrate the complex electronic structure and bonding situations present in the $(Mg_2Cl_2)_4$ clusters.
All identified $(Mg_2Cl_2)_4$ isomers **15a–f** lie within a 45–82 kJ mol^{-1} range at the BP86, TPSS, B3LYP, and MP2 levels. The energetic ordering of the individual isomers varies depending on the functional, though all functionals agree on isomer **15c** as the most stable structure in agreement with the MP2 results.
The relative stabilities of the $(Mg_2Cl_2)_4$ isomers depending on the method are as follows (values in kJ mol^{-1}):

BP86: **15c** < **15e** (5.5) < **15a** (46.3) < **15f** (55.9) < **15b** (57.7)< **15d** (61.6)

TPSS: **15c** < **15e** (8.1) < **15a** (59.5) < **15f** (62.9) < **15d** (67.7) < **15b** (77.5)

B3LYP: **15a** ≈ **15c** < **15b** (7.0) ≈ **15e** (7.2) < **15d** (31.1) < **15f** (45.1)

MP2: **15c** < **15e** (5.7) < **15a** (61.1) < **15d** (64.1) < **15b** (72.9) < **15f** (82.0)

The reaction enthalpies, ΔH_r^0 (298 K), of the oligomerisation reactions

$$x\,\mathrm{Mg(g)} + x\,\mathrm{MgCl_2(g)} \rightarrow (\mathrm{Mg_2Cl_2})_x\mathrm{(g)}$$

are calculated for $x = 1$, 2, and 4. For $x = 1$, that is, the formation of the linear monomer **13a**, ΔH_r^0 (298 K) is -56.6 kJ mol^{-1} at the CCSD(T)/aug-cc-pCVTZ level. Furthermore, the formations of the larger MgCl oligomers ($x = 2$ and 4) are exothermic reactions (cf. Table 3.26 and 3.27). The MP2 and corresponding CCSD(T) results for the $(Mg_2Cl_2)_x$ compounds with $x = 1$ and 2 are in good mutual agreement, suggesting that MP2 reaction enthalpies for larger clusters, *e.g.* $x = 4$ (where the CCSD(T) calculations are no longer feasible) would be of sufficient accuracy as well. In all cases, the clusters gain stabilisation with increasing cluster size. Taking only 3D structures for the larger clusters into account, there is an energy gain of about 128 kJ mol^{-1} (CCSD(T)/aug-cc-pCVTZ) to 139 kJ mol^{-1} (MP2/aug-cc-pCVTZ) for $(Mg_2Cl_2)_2$ isomer **12c** when compared to the linear monomer **13a**. The extra stabilisation (dimerisation enthalpy) increases to 305 kJ mol^{-1} for $(Mg_2Cl_2)_4$ isomer **15a** (composed purely of Mg_2^{2+} units) with respect to the $(Mg_2Cl_2)_2$ isomer **12c**.
The calculated stabilisation energies, starting from Mg(g) and $MgCl_2$(g), are so large that with the vaporisation enthalpy of 148 kJ mol^{-1} for solid Mg(s),[204] the reaction of $MgCl_2$(g) with *solid* Mg(s) in a nonpolar solvent forming $(Mg_2Cl_2)_x$ oligomers is exothermic for cluster sizes with $x \geq 4$.

Table 3.26. Calculated reaction enthalpies ΔH_r^0 (298 K) for the reaction $2\,Mg(g) + 2\,MgCl_2(g) \rightarrow (Mg_2Cl_2)_2(g)$ at the BP86/def2-TZVPP, TPSS/def2-TZVPP, B3LYP/def2-TZVPP, MP2/aug-cc-pCVTZ, and CCSD(T)/aug-cc-pCVTZ levels of theory. Enthalpies are in kJ mol^{-1}.

	12a	**12b**	**12c**	**12d**	**12e**
BP86	−234.8	−218.9	−211.3	−205.6	−208.3
TPSS	−266.1	−249.4	−255.2	−246.7	−239.8
B3LYP	−216.2	−199.3	−159.8	−163.7	−177.4
MP2[a]	−271.2	−253.4	−251.9	−250.7	−239.5
CCSD(T)[a]	−268.8	−252.7	−241.8	−241.2	−237.2

[a] energies at the B3LYP/def2-TZVPP optimal geometries

Table 3.27. Calculated reaction enthalpies ΔH_r^0 (298 K) for the reaction $4\,Mg(g) + 4\,MgCl_2(g) \rightarrow (Mg_2Cl_2)_4(g)$ at the BP86/def2-TZVPP, TPSS/def2-TZVPP, B3LYP/def2-TZVPP, and MP2/aug-cc-pCVTZ levels of theory. Enthalpies are in kJ mol^{-1}.

	15a	**15b**	**15c**	**15d**	**15e**	**15f**
BP86	−666.1	−654.7	−712.4	−650.8	−707.0	−656.6
TPSS	−761.6	−743.6	−821.1	−753.4	−813.0	−758.2
B3LYP	−582.4	−575.7	−582.7	−551.6	−575.5	−537.6
MP2[a]	−808.5	−796.7	−869.6	−805.5	−863.9	−787.6

[a] energies at the B3LYP/def2-TZVPP optimal geometries

The investigation of the dihalides Al_2X_4 and the $(Mg_2Cl_2)_x$ oligomers reveals a large variety of bonding motives ranging from direct metal–metal bonds to ligand-bridged metal centres present in the Al(II) and Mg(I) compounds.

As model compounds for Al_2R_4 species, the Al_2X_4 monomers and their respective dimers demonstrate the effects of different ligands on the orientation of the metal centres, giving rise to a structural diversity.

For the recently observed molecule Mg_2Cl_2, a dissociation energy of the Mg–Mg σ bond between the two Mg(I) centres has been determined experimentally to amount to 200 kJ mol^{-1} in agreement with the DFT calculations. In the current investigation of the larger $(Mg_2Cl_2)_x$ oligomers, further stabilisation of the Mg_2Cl_2 units due to oligomerisation is found. On the one hand, the large calculated stabilisation energies, going from $128\,\mathrm{kJ\,mol^{-1}}$ for the oligomer $(Mg_2Cl_2)_2$ to $305\,\mathrm{kJ\,mol^{-1}}$ for $(Mg_2Cl_2)_4$, suggest further stabilisation of larger $(MgCl)_x$ clusters and indicates the thermodynamically possible existence of the so far unknown solid MgCl. On the other hand, the partial internal disproportionation that is already observed for some isomers of the small MgCl clusters could gain significance with larger $(MgCl)_x$ clusters, thus discouraging routes to solid MgCl.

4. Summary

The presented *ab initio* computational study of diverse bonding situations in nanostructures spans interactions in a broad energy range of 15 to 200 kJ mol^{-1}. This energy range includes weak interactions (physisorption) that are mostly governed by dispersive forces, ionic and covalent metal–ligand interactions up to covalent metal–metal bonding.

The investigation of primary alcohols interacting with the inner and outer surfaces of single-walled carbon nanotubes (section 3.2) represents a computational study in the regime of weak interactions in nanostructures due to dispersive forces. In these systems, the observed interactions amount to 15–70 kJ mol^{-1}. This energy range allows for the reversible binding and subsequent release of the adsorbate under mild conditions, making it especially interesting for storage purposes.

The water-encapsulation in cage-opened [59]fullerenones (studied in section 3.3) demonstrates interactions within the same order of magnitude as described above ($\sim$45 kJ mol^{-1}) that are relevant for dynamical host–guest processes in these cages.

The interactions of functionalised fullerene ligands with metal centres (section 3.4) comprise ionic and covalent portions that both contribute to the bonding. The strength of these bonds lies in the centre span of the investigated energy range. The observed binding strength and the ligand's design facilitate the formation of stable porous coordination polymers, *i.e.* metal–organic frameworks.

For the direct metal–metal bonds that are subject to investigations of subvalent aluminium and magnesium compounds (section 3.5), the Mg–Mg σ bond of about 200 kJ mol^{-1} designates the upper limit for the studied bonding strengths. The investigations demonstrate a large variety of binding motives for these subvalent metal compounds and indicate the thermodynamically possible existence of solid MgCl, however also revealing possible obstacles.

The use of model compounds is inevitable in the course of an *ab initio* computational study of nanostructures. These model compounds serve as representatives of the nanostructures either to make the computations actually feasible or to validate and to benchmark results obtained for the complete system at a lower computational level. The computations performed in the sections 3.1 and 3.2 have demonstrated the valuable benefit of model compounds (*i.e.* finite tube sections and smaller carbon-based models) for investigating molecular interactions with SWCNTs, provided that a proper selection and validation is done. Furthermore, in dealing with the subvalent magnesium and aluminium compounds in section 3.5, it becomes clear that the use of model compounds, in most cases smaller building units (subunits) of the nanostructures, provides further insight into conceptual structural motives and bonding present in the larger systems.

An adequate validation of the empirical dispersion corrected DFT method proves the applicability to the systems of interest in this work and ensures the significance of the obtained results. With the DFT-D methods, a valuable and cost-efficient tool is on hand for large-scale computational investigations of nanostructures where dispersion plays a crucial role, provided that an appropriate benchmark study has been performed prior to the application, to validate said application. The SCS-MP2 method shows significant improvements over conventional MP2, accurately describing the weak interactions studied in this work. Consequently, SCS-MP2 allows for a correlation treatment at moderate costs, and is convenient for benchmarking purposes.

Zusammenfassung

Gegenstand der vorliegenden Arbeit sind quantenchemische Untersuchungen vielfältiger Bindungstypen, die in unterschiedlichsten Nanostrukturen über einen weiten Energiebereich von 15 bis 200 kJ mol^{-1} vorkommen. Dieser Energiebereich umfasst schwache Wechselwirkungen aufgrund von Dispersionskräften (Physisorption), ionische und/oder kovalente Metall-Ligand Wechselwirkungen, sowie starke Bindungen basierend auf reinen Metall-Metall Wechselwirkungen.
Die Wechselwirkungen primärer Alkohole (Methanol und Ethanol) mit den Innen- und Außenseiten einwandiger Kohlenstoffnanoröhren, die Gegenstand quatenchemischer Untersuchungen in Abschnitt 3.2 sind, stellen ein Beispiel für schwache, hauptsächlich auf Dispersion beruhender Bindungen in nanoskaligen Systemen dar. Die berechneten Wechselwirkungsenergien von 15–70 kJ mol^{-1} hängen zum einen vom Diameter der Röhren, zum anderen von der Größe des untersuchten Alkoholmoleküls ab. Der beobachtete Energiebereich erlaubt eine reversible Bindung und anschließende Wiederfreisetzung des Adsorbatmoleküls unter milden Reaktionsbedingungen, was von besonderem Interesse für Anwendungen im Bereich der Energiespeicherung ist.
Die experimentell beobachtete Aufnahme eines Wassermoleküls in offenen [59]Fullerenon-Käfigen ist Gegenstand von theoretischen Untersuchungen in Abschnitt 3.3. Die berechneten Wechselwirkungsenergien dieser Wirt-Gast-Systeme liegen mit ca. 45 kJ mol^{-1} im gleichen Energiebereich, der für die Alkohol–Kohlenstoffnanoröhren Systeme gefunden wurde. Die untersuchten Wirtskäfige sind damit ebenfalls relevant für dynamische Bindungsprozesse.
Die Wechselwirkungen funktionalisierter Fulleren-Liganden mit Metallzentren (Abschnitt 3.4) setzen sich sowohl aus ionischen als auch kovalenten Anteilen zusammen, die beide zur Bindung beitragen. Die berechneten Bindungsenergien in diesen Komplexen bilden das Mittelfeld des in dieser Arbeit untersuchten Energieintervalls und ermöglichen in Kombination mit den maßgeschneiderten Liganden die Ausbildung stabiler metall-organischer Netzwerke (Koordinationspolymere).
Das Hauptaugenmerk der quantenchemischen Untersuchungen an niedervalenten Aluminium- und Magnesiumverbindungen in Abschnitt 3.5 liegt auf den direkten Metall-Metall-Bindungen. Die Mg-Mg-σ-Bindung bildet mit einer Bindungsenergie von etwa 200 kJ mol^{-1} die Obergrenze des untersuchten Ener-

giebereiches. Die subvalenten Aluminium- und Magnesiumverbindungen zeigen eine große Vielfalt an unterschiedlichen Bindungsmotiven, die von terminalen Ligand-Metall Bindungen über ligandverbrückte Metallzentren bis hin zu Metall-Metall Bindungen reichen. Die Berechnungen belegen die thermodynamisch mögliche Bildung von bisher unbekanntem festem MgCl, zeigen jedoch auch denkbare Hürden auf dem Weg dorthin auf.

Modellverbindungen sind unverzichtbare Hilfsmittel für quantenchemische Untersuchungen von Nanostrukturen. Diese kleineren Modelle der zu untersuchenden Nanostrukturen machen die Berechnung sehr großer Systeme überhaupt erst möglich oder dienen in Kombination mit genaueren, aber auch teureren Rechenmethoden zur Validierung von Ergebnissen, die mit Methoden von geringerer Genauigkeit für das komplette System erhalten wurden. Die quantenchemischen Rechnungen in den Abschnitten 3.1 und 3.2 haben den großen Nutzen dieser Modellverbindungen (in Form von finiten Röhrenabschnitten bzw. kleineren Röhrenausschnitten) zur Beschreibung intermolekularer Wechselwirkungen von kleinen Molekülen mit Kohlenstoffnanoröhren gezeigt. Aussagekräftige Ergebnisse setzen jedoch immer eine passende Auswahl und anschließende Validierung der geeigneten Modellsysteme voraus. Da die Modellverbindungen in den meisten Fällen auch Bildungseinheiten der Nanostrukturen darstellen, liefern die Berechnungen an diesen kleineren Systemen zusätzlich oft auch konzeptionelle Erkenntnisse über Aufbauprinzipien und wiederkehrende Strukturmotive.

Eine umfangreiche Validierung der empirisch dispersionskorrigierten Dichtefunktionalmethode (DFT-D) zeigt die Anwendbarkeit der Methode für die in dieser Arbeit berechneten Systeme und sichert die Aussagekraft der erzielten Ergebnisse. Demnach eignet sich die DFT-D Methode in effizienter Weise zur Berechnung nanoskaliger Systeme, in denen Dispersion eine entscheidende Rolle spielt. Jeder Anwendung der Methode auf neue, unbekannte Systeme muss jedoch eine ausreichende Eignungsprüfung vorausgehen. Diese Arbeit bestätigt eine deutlich erhöhte Genauigkeit der SCS-MP2 Methode gegenüber konventionellem MP2 für die Beschreibung schwacher Wechselwirkungen. SCS-MP2 stellt damit die günstigste wellenfunktionsbasierte Korrelationsmethode für die nötigen Validierungen von weniger genauen quantenchemischen Methoden dar.

A. Abbreviations

AO	Atomic orbital
B3LYP	Becke 3 parameter hybrid functional, Lee–Yang–Parr functional for correlation energy
BLYP	Becke and Lee–Yang–Parr
BP86	Becke–Perdew 1986
BSSE	Basis set superposition error
CBS	Complete basis set
CC	Coupled cluster
CCS	Coupled cluster singles
CCSD	Coupled cluster singles and doubles
CCSD(T)	Coupled cluster singles, doubles, and pertubative triples
CCSDT	Coupled cluster singles, doubles, and triples
CGTO	Contracted Gaussian type orbital
CNT	Carbon nanotube
CP	Counterpoise
CV	Core valence
DFT	Density functional theory
DFTB	Density-functional tight-binding
DFT-D	Density functional theory with empirical dispersion correction
EHT	Extended Hückel theory
EQ	Equilibrium
FTIR	Fourier transform infrared
GA	Genetic algorithm
GGA	Generalised gradient approximation
GSM	Growing string method
GTO	Gaussian type orbital
HF	Hartree–Fock
HiPCO	High pressure carbon monoxide (production method for CNTs)
HODMO	Highest occupied delocalised molecular orbital
HOMO	Highest occupied molecular orbital
HSE	Heyd–Scuseria–Ernzerhof

KS	Kohn–Sham
LCAO	Linear combination of atomic orbitals
LDA	Local density approximation
LMO	Localised molecular orbital
LUDMO	Lowest unoccupied delocalised molecular orbital
LUMO	Lowest unoccupied molecular orbital
MARI-J	Multipole-accelerated resolution of the identity approximation for Coulomb repulsion integrals (J)
MEP	Minimum energy path
MO	Molecular orbital
MOF	Metal–organic framework
MP2	Møller–Plesset second-order pertubation theory
MWCNT	Multi-walled carbon nanotube
NEB	Nudged elastic band
NMR	Nuclear magnetic resonance
NPA	Natural population analysis
OS	Opposite spin
PBE	Perdew–Burke–Ernzerhof
PES	Potential energy surface
PGTO	Primitive Gaussian type orbital
PW	Perdew–Wang
QC	Quantum chemistry
QM	Quantum mechanics
RHF	Restricted Hartree–Fock
RI	Resolution of the identity
SCF	Self-consistent field
SCS-MP2	Spin-component-scaled MP2
SM	String method
SOMO	Singly occupied molecular orbital
SOS-MP2	Scaled opposite-spin MP2
SS	Same spin
STO	Slater type orbital
SWCNT	Single-walled carbon nanotube
TB	Tight binding
TDS	Thermal desorption spectroscopy
TPSS	Tao–Perdew–Staroverov–Scuseria
TRIM	Trust region image minimisation
TS	Transition state
UHF	Unrestricted Hartree–Fock
UKS	Unrestricted Kohn–Sham

vdW	van der Waals
VWN	Vosko–Wilk–Nusair
ZF	Zone-folding
ZPVE	Zero-point vibrational energy

B. Copyright Permissions

Chapter 3 contains in part material that has already been published as articles in scientific peer-reviewed journals. The copyright permissions for published and submitted material are granted from the right owners. In detail they are:
Results, tables and figures in the sections 3.1 and 3.2 are reproduced in part with permission from: Pankewitz, T.; Klopper, W.: *Ab Initio Modeling of Methanol Interaction with Single-Walled Carbon Nanotubes*, J. Phys. Chem. C **2007**, *111*, 18917–18926. Copyright **2007** American Chemical Society.
Results, tables and figures in section 3.3 are reproduced in part with permission from: Pankewitz, T.; Klopper, W.: *Theoretical Investigation of Equilibrium and Transition State Structures, Binding Energies and Barrier Heights of Water-Encapsulated Open-Cage [59]Fullerenone Complexes*, Chem. Phys. Lett. **2008**, *465*, 48–52. Copyright **2008** Elsevier B.V.
Results, tables and figures in section 3.5 are reproduced in part with permission from: Pankewitz, T.; Klopper, W.; Henke, P.; Schnöckel, H.: *Isomeric* Al_2R_4, Mg_2R_2 *Species and Oligomerisation Products: Investigation of Al–Al and Mg–Mg* σ*-Bonding*, Eur. J. Inorg. Chem. **2008**, *2008*, 4879–4890. Copyright **2008** Wiley-VCH Verlag GmbH & KGaA.

List of Tables

3.1. Optimised equilibrium distances R_{OX} and binding energies D_{e} for the test model benzene–MeOH using DFT, DFT-D, MP2, SCS-MP2, and CCSD(T). 30
3.2. Optimised equilibrium distances R_{OX} and binding energies D_{e} for the test model benzene–MeOH, applying the revised DFT-D approach (labelled as DFT-D*). 32
3.3. Optimised equilibrium distances R_{OX} and binding energies D_{e} for the test model coronene–MeOH using DFT-D are compared with MP2 and SCS-MP2 results. 34
3.4. Optimised equilibrium distances R_{OX} and binding energies D_{e} for the test model coronene–MeOH, applying the revised DFT-D approach (labelled as DFT-D*). 35
3.5. Band gaps (eV) of the infinite (7,0), (10,0), and (13,0) SWCNT, extrapolated from HODMO–LUDMO gaps by consecutive elongation of the calculated sections. 43
3.6. Diameter-dependence of the number of local spin-orbitals at the tube ends of H-terminated finite zigzag SWCNTs and resulting high-spin states. 44
3.7. Dependence of D_{e} and R_{OX} on the section length of the finite SWCNTs. This is tested for the exohedral interaction of MeOH, EtOH with armchair (4,4) SWCNT sections ($x = 3, 4, 5, 7$ benzene units along the tube axis) and zigzag (7,0) SWCNT sections ($x = 4, 5, 7$). The endohedral interaction is assessed with (5,5) SWCNT sections ($x = 3, 5, 7$). All values are obtained with BP86-D/TZVP. 50
3.8. Binding energies D_{e} and equilibrium distances R_{OX} for the exohedral interaction of MeOH and EtOH with finite armchair SWCNTs of various diameters at the BP86-D/TZVP level of theory (sections with $x = 3$, perpendicular approach). The limiting case of zero-curvature is modelled by a coronene molecule and two graphene models. 52

3.9. Binding energies D_e (kJ mol^{-1}) for the exohedral MeOH interaction evaluated with a curved coronene model. The coronene–MeOH subsections are taken from each equilibrium geometry of the different SWCNTs (cf. Figs. 3.10 and 3.12) and single-point energy calculations are performed with BP86-D/TZVP. For comparison, SCS-MP2/QZVP values are also given. 53

3.10. Binding energies D_e and equilibrium distances R_{OX} for the endohedral interaction of MeOH and EtOH with finite armchair SWCNTs of various diameters at the BP86-D/TZVP level of theory (sections with $x = 3$ (MeOH) and $x = 5$ (EtOH), perpendicular approach). For the limiting case of zero-curvature in graphene, see Table 3.8. 55

3.11. The O–O distances (pm) between the keto groups surrounding the rim of the orifices for the empty fullerenone cages **1** and **2** and for the equilibrium and TS structures of H_2O@**1** and H_2O@**2** (at the BP86-D level). 63

3.12. Uncorrected and counterpoise corrected binding energies ΔE, ΔE^{CP} for an encapsulated water molecule in H_2O@**1** and H_2O@**2** at the BP86-D level of theory. For comparison, the BP86 results without dispersion correction are also shown. All energies are in kJ mol^{-1}. 63

3.13. Uncorrected and counterpoise corrected binding energies ΔE, ΔE^{CP} for an encapsulated water molecule in $H_2O@C_{60}$ at the BP86-D, MP2 and SCS-MP2 levels of theory. All energies are in kJ mol^{-1}. 64

3.14. Counterpoise corrected barrier heights ΔE^{CP} for the encapsulated water molecule leaving H_2O@**1** and H_2O@**2** at the BP86-D level of theory. In addition, counterpoise corrections (ΔCP) for the equilibrium and TS structures of H_2O@**1** and H_2O@**2** are given. All energies are in kJ mol^{-1}. 66

3.15. Comparison of the dihedral angle ONCC (°) in the equilibrium and TS structures of H_2O@**1** and H_2O@**2** (BP86-D/def-SV(P)). Values in the crystal structures are given between parentheses. . 68

3.16. Selected bond lengths (pm) in the intramolecular complexes **$PdCl_2L1$**, **$PdCl_2L2$** and the intermolecular complexes **$PdCl_2(L1)_2$**, **$PdCl_2(L2)_2$** at the BP86/def2-SV(P) level of theory (values in parentheses at the BP86/def2-TZVP level). For the numbering of atoms refer to Figs. 3.20 and 3.21. 72

3.17. Selected bond lengths (pm) in the intramolecular complex **$PdCl_2L3$** and intermolecular complex **$PdCl_2(L3)_2$** at the BP86/def2-SV(P) level of theory. For the numbering of atoms refer to Figs. 3.22 and 3.23. 74

3.18. Complexation energies (kJ mol^{-1}) for the intra- and intermolecular coordination of the fullerene ligands **L1**, **L2** and **L3** to $PdCl_2$ forming the complexes $PdCl_2L$ and $PdCl_2(L)_2$. The ΔE(inter−intra) values show the energetic preference of the intermolecular complexation for all ligands. 76

3.19. Structural parameters of the compounds $(Al_2F_4)_2$ **8** and $(Al_2Cl_4)_2$ **10** calculated at the BP86/def2-TZVPP and B3LYP/def2-TZVPP levels (cf. Figs. 3.27 and 3.28 for numbering of atoms). Selected bond lengths (pm) and bond angles (°) are given. X denotes F or Cl. 84

3.20. Structural parameters of the monomeric isomers of Al_2F_4 **9a**–**d** and Al_2Cl_4 **11a**–**d** calculated at the BP86/def2-TZVPP and B3LYP/def2-TZVPP levels (cf. Figs. 3.27 and 3.28 for numbering of atoms). Selected bond lengths (pm) and bond angles (°) are given. X denotes F or Cl. 85

3.21. Atomic charges based on the natural population analysis (NPA) for the different isomers of Al_2F_4 and Al_2Cl_4, obtained at the B3LYP/def2-TZVPP level (X denotes F or Cl). Charges are in units of *e*. 86

3.22. Calculated reaction enthalpies ΔH_r^0 (298 K) for the dimerisation reaction of the isomeric monomers **9a**–**d** and **11a**–**d** ($2\,Al_2F_4 \rightarrow (Al_2F_4)_2$ and $2\,Al_2Cl_4 \rightarrow (Al_2Cl_4)_2$, respectively) at the BP86/def2-TZVPP, B3LYP/def2-TZVPP, and MP2/aug-cc-pwCVTZ levels of theory. Enthalpies are in kJ mol^{-1}. 87

3.23. Structural parameters for $(Mg_2Cl_2)_2$ **12d**, the isoelectronic ion $Al_4Cl_4^{4+}$ **14**, and the monomeric isomers Mg_2Cl_2 **13a**–**b** (cf. Fig. 3.29 for numbering of atoms). Selected bond lengths (pm) and bond angles (°) are at the BP86/def2-TZVPP and B3LYP/def2-TZVPP levels of theory. 88

3.24. Atomic charges based on a natural population analysis (NPA) for the $(Mg_2Cl_2)_2$ isomers **12a–e** calculated at the B3LYP/def2-TZVPP level. Charges are in units of *e*. 91

3.25. Atomic charges on the magnesium centres of the different $(Mg_2Cl_2)_4$ isomers **15a–f** based on a natural population analysis (NPA) (B3LYP/def2-TZVPP level). Charges are in units of *e*. 94

3.26. Calculated reaction enthalpies ΔH^0_r (298 K) for the reaction $2\,\mathrm{Mg(g)} + 2\,\mathrm{MgCl_2(g)} \rightarrow \mathrm{(Mg_2Cl_2)_2(g)}$ at the BP86/def2-TZVPP, TPSS/def2-TZVPP, B3LYP/def2-TZVPP, MP2/aug-cc-pCVTZ, and CCSD(T)/aug-cc-pCVTZ levels of theory. Enthalpies are in $\mathrm{kJ\,mol^{-1}}$. 96

3.27. Calculated reaction enthalpies ΔH^0_r (298 K) for the reaction $4\,\mathrm{Mg(g)} + 4\,\mathrm{MgCl_2(g)} \rightarrow \mathrm{(Mg_2Cl_2)_4(g)}$ at the BP86/def2-TZVPP, TPSS/def2-TZVPP, B3LYP/def2-TZVPP, and MP2/aug-cc-pCVTZ levels of theory. Enthalpies are in $\mathrm{kJ\,mol^{-1}}$. 96

List of Figures

3.1. Equilibrium geometries of the perpendicular approach of MeOH to the centre X of a benzene ring. a) conventional DFT, BP86/TZVP b) DFT-D including empirical dispersion correction, BP86-D/TZVP. 29

3.2. Potential energy curves of the perpendicular approach of MeOH to the ring centre X of benzene. a) BP86-D, BLYP-D, and PBE-D curves are compared to conventional BP86 and PBE curves without dispersion correction as well as to MP2 results. b) SCS-MP2 results compared to standard MP2 and DFT-D curves (formerly filled black symbols are shown in grey). 31

3.3. Potential energy curves of the perpendicular approach of MeOH to the centre X of coronene. BP86-D, BLYP-D, and PBE-D potential curves are compared to MP2 and SCS-MP2 results. The local minimum found at $R_{\mathrm{OX}} \sim 480\,\mathrm{pm}$ corresponds to a structure in which the CH_3 group is pointing down towards the coronene, as shown in the figure. 33

3.4. SWCNT vector map for right-handed tubes. The unit cell of graphene (highlighted in gray) is spanned by the two primitive lattice vectors $\mathbf{a}_1$ and $\mathbf{a}_2$ and contains two carbon atoms (marked as black dots). Armchair SWCNTs are defined by chiral vectors, $\mathbf{C_h}$, along the (n,n) direction (as indicated in blue) with a chiral angle of $\Theta = 30°$. Zigzag SWCNTs are defined by $\mathbf{C_h}$ along the $(n,0)$ direction with $\Theta = 0°$. As an example, $\mathbf{C_h}$ of the chiral (7,3) SWCNT, as well as the chiral angle, Θ are given (in red). 37

3.5. Energy diagram of frontier orbitals of the (7,0) SWCNT section, $x = 5$, 1.07 nm, $D_{7\mathrm{h}}$: a) singlet b) quintet (both UKS calculations). The quintet state is stabilised by $73.8\,\mathrm{kJ\,mol^{-1}}$ at the BP86/SV(P) level of theory. The HOMO–LUMO and HODMO–LUDMO gaps are indicated for the quintet state. 40

3.6. HOMO–LUMO and HODMO–LUDMO gaps in (7,0) SWCNT sections (0.64–4.29 nm) calculated with the functionals BP86, PBE, and TPSS in an SV(P) basis. Note that there is almost no functional effect on the HODMO–LUDMO gap. 41

3.7. Frontier orbitals of the (7,0) SWCNT section, $x = 5$, 1.07 nm, $D_{7\mathrm{h}}$ at the BP86/SV(P) level of theory. The highest occupied molecular orbitals (HOMOs), which are localised at the ends of the tube, and the highest occupied delocalised molecular orbitals (HODMOs), which are delocalised over the entire tube, are plotted. The lowest unoccupied molecular orbital (LUMO) is also shown. Note that in this case the LUMO is delocalised over the tube and therefore is also the LUDMO. 42

3.8. HOMO–LUMO gaps in armchair (4,4) SWCNT sections (0.24 to 2.97 nm) calculated at the BP86/TZVP//BP86/SV(P) level. HOMO–LUMO gaps within one class, either Kekulé (blue), incomplete Clar (red), or complete Clar (green) networks are categorised by dashed lines. 45

3.9. Interaction of the primary alcohols, MeOH and EtOH, with the outer (exohedral) and the inner (endohedral) surface of the finite armchair (8,8) SWCNTs. The diameter of the tubes is 1.08 nm. . 47

3.10. A model coronene–MeOH subsection is cut from the equilibrium structure of MeOH interacting with a finite armchair SWCNT. The dangling bonds are saturated with hydrogen atoms with a C–H distance of 110 pm (along the former C–C bonds). 48

3.11. MeOH molecule interacting with graphene, modelling an infinite-diameter tube (zero-curvature). a) model with 66 C atoms, H-terminated b) model with 112 C atoms, H-terminated, no zigzag ends. 49

3.12. Equilibrium geometries of the exohedral interaction of MeOH with finite armchair SWCNTs of various diameters at the BP86-D/TZVP level of theory (sections with $x = 3$, perpendicular approach). The corresponding coronene–MeOH subsections are shown to illustrate the change in the curvature of the coronene model. 53

3.13. The binding energies D_{e} of MeOH interacting with the different armchair tube sections and the curved coronene subsections are plotted. The dispersion contributions to the binding energy are also shown, as evaluated with the empirical dispersion correction scheme. (x is the number of benzene units along the tube axis.) 54

3.14. The geometries of the two [59]fullerenone cages **1** and **2** at the BP86-D/def2-TZVP level of theory. **1** has an 18-membered-ring orifice, **2** a larger 19-membered-ring orifice. Atoms not labelled explicitly are carbon (grey) and hydrogen (white). 59

3.15. Equilibrium (EQ, left) and transition state (TS, right) structure of H_2O@**1** at the BP86-D/def-SV(P) level of theory. The barrier height is 107.9 kJ mol^{-1} (BP86-D/def2-TZVP//BP86-D/def-SV(P)). The indicated atoms form the dihedral angle ONCC between the phenyl substituent and the isomaleimide unit. 62

3.16. Equilibrium (EQ, left) and transition state (TS, right) structure of H_2O@**2** at the BP86-D/def-SV(P) level of theory. The barrier height is 46.4 kJ mol^{-1} (BP86-D/def2-TZVP//BP86-D/def-SV(P)). The indicated atoms form the dihedral angle ONCC between the phenyl substituent and the isomaleimide unit. 62

3.17. Rotational energy in the phenyl-isomaleimide molecule as function of the dihedral angle ONCC (BP86-D/def2-TZVP). The phenyl-isomaleimide molecule is displayed as insert, atoms forming $\angle$ONCC are indicated with underlined labels. Atoms not labelled explicitly are carbon (grey) and hydrogen (white). 68

3.18. Metal complex **1** formed by a bis-pyridine C_{60} ligand and $CuCl_2$ (Pierrat *et al.*). The intramolecular metal complexation with both coordination sites of one ligand attached to the same Cu-centre takes place quantitatively. 71

3.19. Fullerene ligands for metal complexation: Bis-triphenylphosphine C_{60} mono-adduct **L1**, bis-adduct **L2**, and bis-pyridine C_{60} bis-adduct **L3** functionalised via a single and double Bingel cyclopropanation. 71

3.20. Intramolecular metal coordination of Pd(II) with the bis-triphenylphosphine C_{60} fullerene ligands **L1** and **L2**, forming the complexes **PdCl$_2$L1** (left) and **PdCl$_2$L2** (right), respectively. BP86/def2-SV(P) structures are displayed. 73

3.21. Intermolecular metal coordination of Pd(II) with the bis-triphenylphosphine C_{60} fullerene ligand **L2**, forming the dimeric complex **PdCl$_2$(L2)$_2$**. The BP86/def2-SV(P) structure is displayed. The free coordination sites (P-triphenylphosphine) of the ligands for forming longer chains are indicated with arrows. 73

3.22. Intramolecular metal coordination of Pd(II) with the bis-pyridine C_{60} fullerene ligand **L3**, forming the complex **$PdCl_2L3$**. The minimum energy structure (left) with an up–down orientation of O1, O2 in the ester groups and a conformer with both O1, O2 pointing up (right) are displayed at the BP86/def2-SV(P) level (energies in $kJ\,mol^{-1}$). 75
3.23. Intermolecular metal coordination of Pd(II) with the bis-pyridine C_{60} fullerene ligand **L3**, forming the dimeric complex **$PdCl_2(L3)_2$**. The BP86/def2-SV(P) structure is displayed. The free coordination sites (N-pyridine) of the ligands for forming longer chains are indicated with arrows. 75
3.24. Structures of the $Al_2(PtBu_2)_4$ isomers: the butterfly structure **1** (C_2 symmetry, ^1A), the TS $\mathbf{1}^\ddagger$ (C_i symmetry) between the two equivalent butterfly structures, the triplet structure **2** (C_i symmetry, ^3A_u), the H-saturated isomer **3** (C_i symmetry, ^1A_g), the linear isomer **4** (C_2 symmetry, ^1A) and the radical fragment **5** (C_2 symmetry, ^2A). For clarity, only the tertiary carbons (orange) of the *t*Bu groups are shown. 79
3.25. Structures of the dimer $(Al_2(OtBu)_4)_2$ **6** and the monomer **7**. For clarity, only the tertiary carbons (orange) of the *t*Bu groups are shown. 79
3.26. Relative electronic energies of the $Al_2(PtBu_2)_4$ isomers, the AlP_2tBu_4 fragment, and the TS $\mathbf{1}^\ddagger$ are given in $kJ\,mol^{-1}$. The diethyl ether stabilised radical of **5** is also shown. Values are at the BP86/def2-TZVP//BP86/def2-TZVP†, (TPSS/def2-TZVP// TPSS/def2-TZVP†) and [B3LYP/def2-TZVP//B3LYP/def2-TZVP†] levels. 80
3.27. Geometries of the dimer $(Al_2F_4)_2$ **8** and the isomeric monomers of Al_2F_4 **9a–d**. Given bond distances (pm) and relative energies ($kJ\,mol^{-1}$) are calculated at the B3LYP/def2-TZVPP level of theory. 82
3.28. Geometries of the dimer $(Al_2Cl_4)_2$ **10** and the isomeric monomers of Al_2Cl_4 **11a–d**. Given bond distances (pm) and relative energies ($kJ\,mol^{-1}$) are calculated at the B3LYP/def2-TZVPP level of theory. 83
3.29. Geometries of $(Mg_2Cl_2)_2$ **12d** and the isomeric monomers Mg_2Cl_2 **13a–b**. The isoelectronic ion $(Al_2Cl_2)_2^{4+}$ **14** is also given. Metal–metal distances (pm) in the different compounds are calculated at the B3LYP/def2-TZVPP level of theory. 88

3.30. Structures of the five identified $(Mg_2Cl_2)_2$ isomers **12a**–**e** in a 25–60 kJ mol^{-1} range (depending on the method and functional). Bond distances (pm) are obtained at the B3LYP/def2-TZVPP level. Total electron density plots for all isomers are also included (isosurfaces with isovalue at 0.022 a_0^{-3}). 89
3.31. Geometries (left) of four out of six identified $(Mg_2Cl_2)_4$ isomers **15a**–**f** in a 45–80 kJ mol^{-1} range (depending on the method and functional). Bond distances (pm) are obtained at the B3LYP/def2-TZVPP level. Total electron density plots are given for each isomer on the right (isosurfaces with isovalue at 0.022 a_0^{-3}). 92
3.32. Geometries (left) of two out of six identified $(Mg_2Cl_2)_4$ isomers **15a**–**f** in a 45–80 kJ mol^{-1} range (depending on the method and functional). Bond distances (pm) are obtained at the B3LYP/def2-TZVPP level. Total electron density plots are given for each isomer on the right (isosurfaces with isovalue at 0.022 a_0^{-3}). 93

Bibliography

[1] Kroto, H. W.; Heath, J. R.; O'Brien, S. C.; Curl, R. F.; Smalley, R. E. *Nature* **1985**, *318*, 162–163.

[2] Iijima, S. *Nature* **1991**, *354*, 56–58.

[3] Dresselhaus, M. S.; Dresselhaus, G.; Eklund, P. C. *Science of fullerenes and carbon nanotubes;* Academic Press: San Diego (USA), 1st ed., **1995**.

[4] Reich, S.; Thomsen, C.; Maultzsch, J. *Carbon Nanotubes;* Wiley-VCH: Weinheim (Germany), 1st ed., **2004**.

[5] Yürüma, Y.; Taralpa, A.; Veziroglu, T. N. *Int. J. Hydrogen Energy* **2009**, *34*, 3784–3798.

[6] Kong, J.; Franklin, N. R.; Zhou, C.; Chapline, M. G.; Peng, S.; Cho, K.; Dai, H. *Science* **2000**, *287*, 622–625.

[7] Avouris, P. *Acc. Chem. Res.* **2002**, *35*, 1026–1034.

[8] Kitagawa, S.; Kitaura, R.; Noro, S. *Angew. Chem. Int. Ed.* **2004**, *43*, 2334–2375.

[9] Son, S. J.; Reichel, J.; He, B.; Schuchman, M.; Lee, S. B. *J. Am. Chem. Soc.* **2005**, *127*, 7316–7317.

[10] Kam, N. W. S.; O'Connell, M.; Wisdom, J. A.; Dai, H. *Proc. Natl. Acad. Sci.* **2005**, *102*, 11600–11605.

[11] Schrödinger, E. *Ann. Physik* **1926**, *384*, 361–376.

[12] Schrödinger, E. *Phys. Rev.* **1926**, *28*, 1049–1070.

[13] Hartree, D. R. *Proc. Cambridge Phil. Soc.* **1928**, *24*, 89–110.

[14] Fock, V. *Z. Phys.* **1930**, *61*, 126–148.

[15] Szabo, A.; Ostlund, N. S. *Modern Quantum Chemistry – Introduction to Advanced Electronic Structure Theory;* McGraw-Hill: New York (USA), 1st ed., **1989**.

[16] Møller, C.; Plesset, M. S. *Phys. Rev.* **1934**, *46*, 618–622.

[17] Coester, F.; Kümmel, H. *Nucl. Phys.* **1960**, *17*, 477–485.

[18] Bartlett, R. J. *J. Phys. Chem.* **1989**, *93*, 1697–1708.

[19] TURBOMOLE V5.9–V6.0 **2006–2009**, a development of University of Karlsruhe and Forschungszentrum Karlsruhe GmbH, 1989–2007, TURBOMOLE GmbH, since 2007; available from `http://www.turbomole.com`.

[20] Ahlrichs, R.; Bär, M.; Häser, M.; Horn, H.; Kölmel, C. *Chem. Phys. Lett.* **1989**, *162*, 165–169.

[21] Strout, D. L.; Scuseria, G. E. *J. Chem. Phys.* **1995**, *102*, 8448–8452.

[22] Jensen, F. *Introduction to Computational Chemistry;* John Wiley & Sons, Ltd: Hoboken (USA), 2nd ed., **2007**.

[23] Raghavachari, K.; Trucks, G. W.; Pople, J. A.; Head-Gordon, M. *Chem. Phys. Lett.* **1989**, *157*, 479–483.

[24] Helgaker, T.; Klopper, W.; Tew, D. P. *Mol. Phys.* **2008**, *106*, 2107–2143.

[25] Hohenberg, P.; Kohn, W. *Phys. Rev.* **1964**, *136*, B864–B871.

[26] Thomas, L. H. *Proc. Cambridge Phil. Soc.* **1927**, *23*, 542–548.

[27] Fermi, E. *Rend. Accad. Lincei* **1927**, *6*, 602–607.

[28] Kohn, W.; Sham, L. J. *Phys. Rev.* **1965**, *140*, A1133–A1138.

[29] Dirac, P. A. M. *Proc. Cambridge Phil. Soc.* **1930**, *26*, 376–385.

[30] Slater, J. C. *Phys. Rev.* **1951**, *81*, 385–390.

[31] Ceperley, D. M.; Alder, B. J. *Phys. Rev. Lett.* **1980**, *45*, 566–569.

[32] Vosko, S. H.; Wilk, L.; Nusair, M. *Can. J. Phys.* **1980**, *58*, 1200–1211.

[33] Perdew, J. P.; Wang, Y. *Phys. Rev. B* **1992**, *45*, 13244–13249.

[34] Ernzerhof, M.; Perdew, J. P.; Burke, K. *Int. J. Quantum Chem.* **1997**, *64*, 285–295.

[35] Becke, A. D. *Phys. Rev. A* **1988**, *38*, 3098–3100.

[36] Perdew, J. P. *Phys. Rev. B* **1986**, *33*, 8822–8824.

[37] Perdew, J. P. *Phys. Rev. B* **1986**, *34*, 7406.

[38] Lee, C.; Yang, W.; Parr, R. G. *Phys. Rev. B* **1988**, *37*, 785–789.

[39] Perdew, J. P.; Burke, K.; Ernzerhof, M. *Phys. Rev. Lett.* **1996**, *77*, 3865–3868.

[40] Tao, J.; Perdew, J. P.; Staroverov, V. N.; Scuseria, G. E. *Phys. Rev. Lett.* **2003**, *91*, 146401.

[41] Staroverov, V. N.; Scuseria, G. E.; Tao, J.; Perdew, J. P. *J. Chem. Phys.* **2003**, *119*, 12129–12137.

[42] Staroverov, V. N.; Scuseria, G. E.; Tao, J.; Perdew, J. P. *J. Chem. Phys.* **2004**, *121*, 11507.

[43] Gritsenko, O. V.; Schipper, P. R. T.; Baerends, E. J. *J. Chem. Phys.* **1997**, *107*, 5007–5015.

[44] Becke, A. D. *J. Chem. Phys.* **1993**, *98*, 5648–5652.

[45] Stephens, P. J.; Devlin, F. J.; Chabalowski, C. F.; Frisch, M. J. *J. Phys. Chem.* **1994**, *98*, 11623–11627.

[46] Treutler, O.; Ahlrichs, R. *J. Chem. Phys.* **1995**, *102*, 346–354.

[47] Kristyán, S.; Pulay, P. *Chem. Phys. Lett.* **1994**, *229*, 175–180.

[48] Pérez-Jordá, J. M.; Becke, A. D. *Chem. Phys. Lett.* **1995**, *233*, 134–137.

[49] Allen, M. J.; Tozer, D. J. *J. Chem. Phys.* **2002**, *117*, 11113–11120.

[50] Ahlrichs, R.; Penco, R.; Scoles, G. *Chem. Phys.* **1977**, *19*, 119–130.

[51] Elstner, M.; Hobza, P.; Frauenheim, T.; Suhai, S.; Kaxiras, E. *J. Chem. Phys.* **2001**, *114*, 5149–5155.

[52] Wu, Q.; Yang, W. *J. Chem. Phys.* **2002**, *116*, 515–524.

[53] Grimme, S. *J. Comput. Chem.* **2004**, *25*, 1463–1473.

[54] Zimmerli, U.; Parrinello, M.; Koumoutsakos, P. *J. Chem. Phys.* **2004**, *120*, 2693–2699.

[55] Grimme, S. *J. Comput. Chem.* **2006**, *27*, 1787–1799.

[56] Curtiss, L. A.; Raghavachari, K.; Redfern, P. C.; Pople, J. A. *J. Chem. Phys.* **1997**, *106*, 1063–1079.

[57] Grimme, S. *J. Chem. Phys.* **2003**, *118*, 9095–9102.

[58] Grimme, S. *J. Phys. Chem. A* **2005**, *109*, 3067–3077.

[59] Sinnokrot, M. O.; Valeev, E. F.; Sherrill, C. D. *J. Am. Chem. Soc.* **2002**, *124*, 10887–10893.

[60] Tsuzuki, S.; Honda, K.; Uchimaru, T.; Mikami, M. *J. Chem. Phys.* **2004**, *120*, 647–659.

[61] Bauschlicher, Jr., C.-W.; Ricca, A. *Phys. Rev. B* **2004**, *70*, 115409.

[62] Klopper, W. *Mol. Phys.* **2001**, *99*, 481–507.

[63] Gerenkamp, M.; Grimme, S. *Chem. Phys. Lett.* **2004**, *392*, 229–235.

[64] Jung, Y.; Lochan, R. C.; Dutoi, A. D.; Head-Gordon, M. *J. Chem. Phys.* **2004**, *121*, 9793–9802.

[65] Schäfer, A.; Horn, H.; Ahlrichs, R. *J. Chem. Phys.* **1992**, *97*, 2571–2577.

[66] Weigend, F.; Ahlrichs, R. *Phys. Chem. Chem. Phys.* **2005**, *7*, 3297–3305.

[67] Schäfer, A.; Huber, C.; Ahlrichs, R. *J. Chem. Phys.* **1994**, *100*, 5829–5835.

[68] Weigend, F.; Furche, F.; Ahlrichs, R. *J. Chem. Phys.* **2003**, *119*, 12753–12762.

[69] Dunning, Jr., T. H. *J. Chem. Phys.* **1989**, *90*, 1007–1023.

[70] Kendall, R. A.; Dunning, Jr., T. H.; Harrison, R. J. *J. Chem. Phys.* **1992**, *96*, 6796–6806.

[71] Dunning, Jr., T. H.; Woon, D. E. *J. Chem. Phys.* **1993**, *98*, 1358–1371.

[72] Woon, D. E.; Dunning, Jr., T. H. *J. Chem. Phys.* **1995**, *103*, 4572–4585.

[73] Peterson, K. A.; Dunning, Jr., T. H. *J. Chem. Phys.* **2002**, *117*, 10548–10560.

[74] Boys, S. F.; Bernardi, F. *Mol. Phys.* **1970**, *19*, 553–566.

[75] Widmark, P.-O., Ed. *European Summerschool in Quantum Chemistry*, Vol. 2; Lund University: Lund (Sweden), 5th ed., **2007**.

[76] Mills, G.; Jónsson, H.; Schenter, G. K. *Surf. Sci.* **1995**, *324*, 305–337.

[77] Henkelman, G.; Jónsson, H. *J. Chem. Phys.* **2000**, *113*, 9978–9985.

[78] E, W.; Ren, W.; Vanden-Eijnden, E. *Phys. Rev. B* **2002**, *66*, 052301.

[79] Peters, B.; Heyden, A.; Bell, A. T.; Chakraborty, A. *J. Chem. Phys.* **2004**, *120*, 7877–7886.

[80] Smith, C. M. *Theor. Chim. Acta* **1988**, *74*, 85–99.

[81] Helgaker, T. *Chem. Phys. Lett.* **1991**, *182*, 503–510.

[82] MOLPRO, version 2006.1, a package of ab initio programs. Werner, H.-J.; Knowles, P. J.; Lindh, R.; Manby, F. R.; Schütz, M.; Celani, P.; Korona, T.; Rauhut, G.; Amos, R. D.; Bernhardsson, A.; Berning, A.; Cooper, D. L.; Deegan, M. J. O.; Dobbyn, A. J.; Eckert, F.; Hampel, C.; Hetzer, G.; Lloyd, A. W.; McNicholas, S. J.; Meyer, W.; Mura, M. E.; Nicklass, A.; Palmieri, P.; Pitzer, R.; Schumann, U.; Stoll, H.; Stone, A. J.; Tarroni, R.; Thorsteinsson, T. **2006**.

[83] ECCE, A Problem Solving Environment for Computational Chemistry, Software Version 4.0.1. Black, G.; Daily, J.; Didier, B.; Elsethagen, T.; Feller, D.; Gracio, D.; Hackler, M.; Havre, S.; Jones, D.; Jurrus, E.; Keller, T.; Lansing, C.; Matsumoto, S.; Palmer, B.; Peterson, M.; Schuchardt, K.; Stephan, E.; Sun, L.; Swanson, K.; Taylor, H.; Thomas, G.; Vorpagel, E.; Windus, T.; Winters, C. **2006**.

[84] Schaftenaar, G.; Noordik, J. H. *J. Comput.-Aided Mol. Design* **2000**, *14*, 123–134.

[85] Humphrey, W.; Dalke, A.; Schulten, K. *J. Molec. Graphics* **1996**, *14*, 33–38.

[86] Eichkorn, K.; Treutler, O.; Öhm, H.; Häser, M.; Ahlrichs, R. *Chem. Phys. Lett.* **1995**, *242*, 652–660.

[87] Eichkorn, K.; Weigend, F.; Treutler, O.; Ahlrichs, R. *Theor. Chem. Acc.* **1997**, *97*, 119–124.

[88] Ahlrichs, R. *Phys. Chem. Chem. Phys.* **2004**, *6*, 5119–5121.

[89] Weigend, F.; Häser, M. *Theor. Chem. Acc.* **1997**, *97*, 331–340.

[90] Weigend, F.; Häser, M.; Patzelt, H.; Ahlrichs, R. *Chem. Phys. Lett.* **1998**, *294*, 143–152.

[91] Hättig, C. *Phys. Chem. Chem. Phys.* **2005**, *7*, 59–66.

[92] Hampel, C.; Peterson, K. A.; Werner, H.-J. *Chem. Phys. Lett.* **1992**, *190*, 1–12.

[93] Deegan, M. J. O.; Knowles, P. J. *Chem. Phys. Lett.* **1994**, *227*, 321–326.

[94] Xantheas, S. S. *J. Chem. Phys.* **1996**, *104*, 8821–8824.

[95] Pribble, R. N.; Hagemeister, F. C.; Zwier, T. S. *J. Chem. Phys.* **1996**, *106*, 2145–2157.

[96] Grimme, S.; Antony, J.; Schwabe, T.; Mück-Lichtenfeld, C. *Org. Biomol. Chem.* **2007**, *5*, 741–758.

[97] Ebbesen, T. W.; Ajayan, P. M. *Nature* **1992**, *358*, 220–222.

[98] Iijima, S.; Ichihashi, T. *Nature* **1993**, *363*, 603–605.

[99] Bethune, D. S.; Klang, C. H.; de Vries, M. S.; Gorman, G.; Savoy, R.; Vazquez, J.; Beyers, R. *Nature* **1993**, *363*, 605–607.

[100] Dresselhaus, M. S.; Dresselhaus, G.; Charlier, J. C.; Hernández, E. *Phil. Trans. R. Soc. Lond. A* **2004**, *362*, 2065–2098.

[101] Britz, D. A.; Khlobystov, A. N. *Chem. Soc. Rev.* **2006**, *35*, 637–659.

[102] Ouyang, M.; Huang, J.-L.; Liebe, C. M. *Acc. Chem. Res.* **2002**, *35*, 1018–1025.

[103] Hamada, N.; Sawada, S.; Oshiyama, A. *Phys. Rev. Lett.* **1992**, *68*, 1579–1581.

[104] Saito, R.; Fujita, M.; Dresselhaus, G.; Dresselhaus, M. S. *Phys. Rev. B* **1992**, *46*, 1804–1811.

[105] Mintmire, J. W.; White, C. T. *Carbon* **1995**, *33*, 893–902.

[106] White, C. T.; Mintmire, J. W. *J. Phys. Chem. B* **2005**, *109*, 52–65.

[107] Bulusheva, L. G.; Okotrub, A. V.; Romanov, D. A.; Tomanek, D. *J. Phys. Chem. A* **1998**, *102*, 975–981.

[108] Rochefort, A.; Salahub, D. R.; Avouris, P. *J. Phys. Chem. B* **1999**, *103*, 641–646.

[109] Liu, L.; Jayanthi, C. S.; Guo, H.; Wu, S. Y. *Phys. Rev. B* **2001**, *64*, 033414.

[110] Barone, V.; Scuseria, G. E. *J. Chem. Phys.* **2004**, *121*, 10376–10379.

[111] Yumura, T.; Bandow, S.; Yoshizawa, K.; Iijima, S. *J. Phys. Chem. B* **2004**, *108*, 11426–11434.

[112] Cioslowski, J.; Rao, N.; Moncrieff, D. *J. Am. Chem. Soc.* **2002**, *124*, 8485–8489.

[113] Matsuo, Y.; Tahara, K.; Nakamura, E. *Org. Lett.* **2003**, *5*, 3181–3184.

[114] Ormsby, J. L.; King, B. T. *J. Org. Chem.* **2004**, *69*, 4287–4291.

[115] Bettinger, H. F. *Org. Lett.* **2004**, *6*, 731–734.

[116] Dillon, A. C.; Jones, K. M.; Bekkedahl, T. A.; Kiang, C. H.; Bethune, D. S.; Heben, M. J. *Nature* **1997**, *386*, 377–379.

[117] Liu, C.; Fan, Y. Y.; Liu, M.; Cong, H. T.; Cheng, H. M.; Dresselhaus, M. S. *Science* **1999**, *286*, 1127–1129.

[118] Dillon, A. C.; Heben, M. J. *Appl. Phys. A* **2001**, *72*, 133–142.

[119] Froudakis, G. E. *J. Phys.: Condens. Matter* **2002**, *14*, R453–R465.

[120] Denis, P. A. *Chem. Phys.* **2008**, *353*, 79–86.

[121] Ellison, M. D.; Crotty, M. J.; Koh, D.; Spray, R. L.; Tate, K. E. *J. Phys. Chem. B* **2004**, *108*, 7938–7943.

[122] Goldoni, A.; Larciprete, R.; Petaccia, L.; Lizzit, S. *J. Am. Chem. Soc.* **2003**, *125*, 11329–11333.

[123] Ellison, M. D.; Good, A. P.; Kinnaman, C. S.; Padgett, N. E. *J. Phys. Chem. B* **2005**, *109*, 10640–10646.

[124] Sung, D.; Hong, S.; Kim, Y. H.; Park, N.; Kim, S.; Maeng, S. L.; Kim, K. C. *Appl. Phys. Lett.* **2006**, *89*, 243110.

[125] Yang, C.-M.; Kanoh, H.; Kaneko, K.; Yudasaka, M.; Iijima, S. *J. Phys. Chem. B* **2002**, *106*, 8994–8999.

[126] Someya, T.; Small, J.; Kim, P.; Nuckolls, C.; Yardley, J. T. *Nano Lett.* **2003**, *3*, 877–881.

[127] Ellison, M. D.; Morris, S. T.; Sender, M. R.; Brigham, J.; Padgett, N. E. *J. Phys. Chem. C* **2007**, *111*, 18127–18134.

[128] Burghaus, U.; Bye, D.; Cosert, K.; Goering, J.; Guerard, A.; Kadossov, E.; Lee, E.; Nadoyama, Y.; Richter, N.; Schaefer, E.; Smith, J.; Ulness, D.; Wymore, B. *Chem. Phys. Lett.* **2007**, *442*, 344–347.

[129] Goering, J.; Kadossov, E.; Burghaus, U. *J. Phys. Chem. C* **2008**, *112*, 10114–10124.

[130] Dicks, A. L. *J. Power Sources* **2006**, *156*, 128–141.

[131] Sierka, M.; Hogekamp, A.; Ahlrichs, R. *J. Chem. Phys.* **2003**, *118*, 9136–9148.

[132] Odom, T. W.; Huang, J.-L.; Kim, P.; Lieber, C. M. *J. Phys. Chem. B* **2000**, *104*, 2794–2809.

[133] Barone, V.; Heyd, J.; Scuseria, G. E. *Chem. Phys. Lett.* **2004**, *389*, 289–292.

[134] Sun, G.; Kürti, J.; Kertesz, M.; Baughman, R. H. *J. Phys. Chem. B* **2003**, *107*, 6924–6931.

[135] Bronikowski, M. J.; Willis, P. A.; Colbert, D. T.; Smith, K. A.; Smalley, R. E. *J. Vac. Sci. Technol. A* **2001**, *19*, 1800–1805.

[136] Du, W.-F.; Wilson, L.; Ripmeester, J.; Dutrisac, R.; Simard, B.; Dénommée, S. *Nano Lett.* **2002**, *2*, 343–346.

[137] Arnold, M. S.; Green, A. A.; Hulvat, J. F.; Stupp, S. I.; Hersam, M. C. *Nature Nanotech.* **2006**, *1*, 60–65.

[138] Heath, J. R.; O'Brien, S. C.; Zhang, Q.; Liu, Y.; Curl, R. F.; Tittel, F. K.; Smalley, R. E. *J. Am. Chem. Soc.* **1985**, *107*, 7779–7780.

[139] Saunders, M.; Jiménez-Vázquez, H. A.; Cross, R. J.; Poreda, R. J. *Science* **1993**, *250*, 1428–1430.

[140] Saunders, M.; Jiménez-Vázquez, H. A.; Cross, R. J.; Mroczkowski, S.; Freedberg, D. I.; Anet, F. A. L. *Nature* **1994**, *367*, 256–258.

[141] Syamala, M. S.; Cross, R. J.; Saunders, M. *J. Am. Chem. Soc.* **2002**, *124*, 6216–6219.

[142] Murphy, T. A.; Pawlik, T.; Weidinger, A.; Höhne, M.; Alcala, R.; Spaeth, J.-M. *Phys. Rev. Lett.* **1996**, *77*, 1075–1078.

[143] Suetsuna, T.; Dragoe, N.; Harneit, W.; Weidinger, A.; Shimotani, H.; Ito, S.; Takagi, H.; Kitazawa, K. *Chem. Eur. J.* **2002**, *8*, 5080–5083.

[144] Wudl, F. *J. Mater. Chem.* **2002**, *12*, 1959–1963.

[145] Chuang, S.-C.; Murata, Y.; Murata, M.; Komatsu, K. *Chem. Commun.* **2007**, pages 1751–1753.

[146] Shameema, O.; Ramachandran, C. N.; Sathyamurthy, N. *J. Phys. Chem. A* **2006**, *110*, 2–4.

[147] Ramachandran, C.; Sathyamurthy, N. *Chem. Phys. Lett.* **2005**, *410*, 348–351.

[148] Cioslowski, J. *J. Am. Chem. Soc.* **1991**, *113*, 4139–4141.

[149] Williams, C. I.; Whitehead, M. A.; Pang, L. *J. Phys. Chem.* **1993**, *97*, 11652–11656.

[150] Hu, Y. H.; Ruckenstein, E. *Chem. Phys. Lett.* **2004**, *390*, 472–474.

[151] Hu, Y. H.; Ruckenstein, E. *J. Chem. Phys.* **2005**, *123*, 144303.

[152] Komatsu, K.; Murata, M.; Murata, Y. *Science* **2005**, *307*, 238–240.

[153] Hummelen, J. C.; Knight, B.; Pavlovich, J.; González, R.; Wudl, F. *Science* **1995**, *269*, 1554–1556.

[154] Rubin, Y.; Jarrosson, T.; Wang, G.-W.; Bartberger, M. D.; Houk, K. N.; Schick, G.; Saunders, M.; Cross, R. J. *Angew. Chem. Int. Ed.* **2001**, *40*, 1543–1546.

[155] Murata, Y.; Murata, M.; Komatsu, K. *J. Am. Chem. Soc.* **2003**, *125*, 7152–7153.

[156] Iwamatsu, S.-i.; Stanisky, C. M.; Cross, R. J.; Saunders, M.; Mizorogi, N.; Nagase, S.; Murata, S. *Angew. Chem. Int. Ed.* **2006**, *45*, 5337–5340.

[157] Yao, J.; Xiao, Z.; Gan, L.; Yang, D.; Wang, Z. *Org. Lett.* **2008**, *10*, 2003–2006.

[158] Iwamatsu, S.-i.; Uozaki, T.; Kobayashi, K.; Re, S.; Nagase, S.; Murata, S. *J. Am. Chem. Soc.* **2004**, *126*, 2668–2669.

[159] Iwamatsu, S.-i.; Murata, S. *Synlett* **2005**, *14*, 2117–2129.

[160] Chuang, S.-C.; Murata, Y.; Murata, M.; .; Komatsu, K. *J. Org. Chem.* **2007**, *72*, 6447–6453.

[161] Xiao, Z.; Yao, J.; Yang, D.; Wang, F.; Huang, S.; Gan, L.; Jia, Z.; Jiang, Z.; Yang, X.; Zheng, B.; Yuan, G.; Zhang, S.; Wang, Z. *J. Am. Chem. Soc.* **2007**, *129*, 16149–16162.

[162] Weigend, F.; Häser, M.; Patzelt, H.; Ahlrichs, R. *Chem. Phys. Lett.* **1998**, *294*, 143–152.

[163] Weigend, F. *Phys. Chem. Chem. Phys.* **2006**, *8*, 1057–1065.

[164] Deglmann, P.; Furche, F.; Ahlrichs, R. *Chem. Phys. Lett.* **2002**, *362*, 511–518.

[165] Deglmann, P.; Furche, F. *J. Chem. Phys.* **2002**, *117*, 9535–9538.

[166] Deglmann, P.; May, K.; Furche, F.; Ahlrichs, R. *Chem. Phys. Lett.* **2004**, *384*, 103–107.

[167] Weigend, F.; Köhn, A.; Hättig, C. *J. Chem. Phys.* **2002**, *116*, 3175–3183.

[168] Weigend, F. *Phys. Chem. Chem. Phys.* **2002**, *4*, 4285–4291.

[169] Kattannek, M. PhD thesis, Universität Karlsruhe (TH), **2006**.

[170] Weigend, F. *J. Comput. Chem.* **2008**, *29*, 167–175.

[171] Prato, M. *J. Mater. Chem.* **1997**, *7*, 1097–1109.

[172] Diederich, F.; Gómez-López, M. *Chem. Soc. Rev.* **1999**, *28*, 263–277.

[173] Bingel, C. *Chem. Ber.* **1993**, *126*, 1957–1959.

[174] Hirsch, A.; Lamparth, I.; Karfunkel, H. R. *Angew. Chem. Int. Ed.* **1994**, *33*, 437–438.

[175] Thilgen, C.; Diederich, F. *C. R. Chimie* **2006**, *9*, 868–880.

[176] Giacalone, F.; Martín, N. *Chem. Rev.* **2006**, *106*, 5136–5190.

[177] Camps, X.; Hirsch, A. *J. Chem. Soc., Perkin Trans. 1* **1997**, pages 1595–1596.

[178] Isaacs, L.; Haldimann, R. F.; Diederich, F. *Angew. Chem. Int. Ed.* **1994**, *33*, 2339–2342.

[179] Isaacs, L.; Diederich, F.; Haldimann, R. F. *Helv. Chim. Acta* **1997**, *80*, 317–342.

[180] Nierengarten, J.-F.; Habicher, T.; Kessinger, R.; Cardullo, F.; Diederich, F.; Gramlich, V.; Gisselbrecht, J.-P.; Boudon, C.; Gross, M. *Helv. Chim. Acta* **1997**, *80*, 2238–2276.

[181] Pierrat, P.; Réthoré, C.; Muller, T.; Bräse, S. *Synlett* **2008**, pages 1706–1710.

[182] Pierrat, P.; Vanderheiden, S.; Muller, T.; Bräse, S. *Chem. Commun.* **2009**, pages 1748–1750.

[183] Yaghi, O. M.; O'Keeffe, M.; Ockwig, N. W.; Chae, H. K.; Eddaoudi, M.; Kim, J. *Nature* **2003**, *423*, 705–714.

[184] Schnepf, A.; Himmel, H.-J. *Angew. Chem. Int. Ed.* **2005**, *44*, 3006–3008.

[185] Westerhausen, M. *Angew. Chem. Int. Ed.* **2008**, *47*, 2185–2187.

[186] Xie, Y.; Schaefer, III, H. F.; Jemmis, E. D. *Chem. Phys. Lett.* **2005**, *402*, 414–421.

[187] Resa, I.; Carmona, E.; Gutierrez-Puebla, E.; Monge, A. *Science* **2004**, *305*, 1136–1138.

[188] Green, S. P.; Jones, C.; Stasch, A. *Science* **2007**, *318*, 1754–1757.

[189] Köppe, R.; Henke, P.; Schnöckel, H. *Angew. Chem. Int. Ed.* **2008**, *47*, 8740–8744.

[190] Uhl, W. *Z. Naturforsch. B* **1988**, *43*, 1113–1118.

[191] Mocker, M.; Robl, C.; Schnöckel, H. *Angew. Chem. Int. Ed.* **1994**, *33*, 862–863.

[192] Dohmeier, C.; Loos, D.; Schnöckel, H. *Angew. Chem. Int. Ed.* **1996**, *35*, 129–149.

[193] Henke, P.; Pankewitz, T.; Klopper, W.; Breher, F.; Schnöckel, H. *Angew. Chem. Int. Ed.* **2009**, *48*, 8141–8145.

[194] Henke, P. PhD thesis, Universität Karlsruhe (TH), **2009**.

[195] Pankewitz, T.; Klopper, W.; Henke, P.; Schnöckel, H. *Eur. J. Inorg. Chem.* **2008**, *2008*, 4879–4890.

[196] Bauernschmitt, R.; Ahlrichs, R. *J. Chem. Phys.* **1996**, *104*, 9047–9052.

[197] Deaven, D. M.; Ho, K. M. *Phys. Rev. Lett.* **1995**, *75*, 288–291.

[198] Sierka, M.; Döbler, J.; Sauer, J.; Santambrogio, G.; Brümmer, M.; Wöste, L.; Janssens, E.; Meijer, G.; Asmis, K. R. *Angew. Chem. Int. Ed.* **2007**, *46*, 3372–3375.

[199] Schuchardt, K. L.; Didier, B. T.; Elsethagen, T.; Sun, L.; Gurumoorthi, V.; Chase, J.; Li, J.; Windus, T. L. *J. Chem. Inf. Mod.* **2007**, *47*, 1045–1052.

[200] Reed, A. E.; Weinstock, R. B.; Weinhold, F. *J. Chem. Phys.* **1985**, *83*, 735–746.

[201] Schmidbaur, H. *Angew. Chem. Int. Ed.* **1985**, *24*, 893–904.

[202] Downs, A. J. *Chemistry of Aluminium, Gallium, Indium, and Thallium;* Chapman & Hall: London (UK), **1993**.

[203] Kalaichev, Y. S.; Petrov, K. P.; Ugarov, V. V. *J. Struct. Chem.* **1983**, *24*, 805–807.

[204] Binnewies, M.; Milke, E. *Thermochemical Data of Elements and Compounds;* Wiley-VCH: Weinheim (Germany), **2002**.

List of Publications

Pankewitz, T.; Lagutschenkov, A.; Niedner-Schatteburg, G.; Xantheas, S. S.; Lee, Y. T.: *Infrared spectrum of $NH_4^+(H_2O)$: Evidence for mode specific fragmentation*, J. Chem. Phys. **2007**, *126*, 074307.

Pankewitz, T.; Klopper, W.: *Ab Initio Modeling of Methanol Interaction with Single-Walled Carbon Nanotubes*, J. Phys. Chem. C **2007**, *111*, 18917–18926.

Pankewitz, T.; Klopper, W.: *Theoretical Investigation of Equilibrium and Transition State Structures, Binding Energies and Barrier Heights of Water-Encapsulated Open-Cage [59]Fullerenone Complexes*, Chem. Phys. Lett. **2008**, *465*, 48–52.

Pankewitz, T.; Klopper, W.; Henke, P.; Schnöckel, H.: *Isomeric Al_2R_4, Mg_2R_2 Species and Oligomerisation Products: Investigation of Al–Al and Mg–Mg σ-Bonding*, Eur. J. Inorg. Chem. **2008**, *2008*, 4879–4890.

Henke, P.; Pankewitz, T.; Klopper, W.; Breher, F.; Schnöckel, H.: *Momentaufnahmen bei der Bildung einer Al-Al-σ-Bindung aus $\{AlR_2\}$-Einheiten – experimentelle und quantenchemische Befunde*, Angew. Chem. **2009**, *121*, 8285-8290;
Snapshots of the Al–Al σ Bond Formation Starting from $\{AlR_2\}$ Units: Experimental and Computational Observations, Angew. Chem. Int. Ed. **2009**, *48*, 8141–8145.

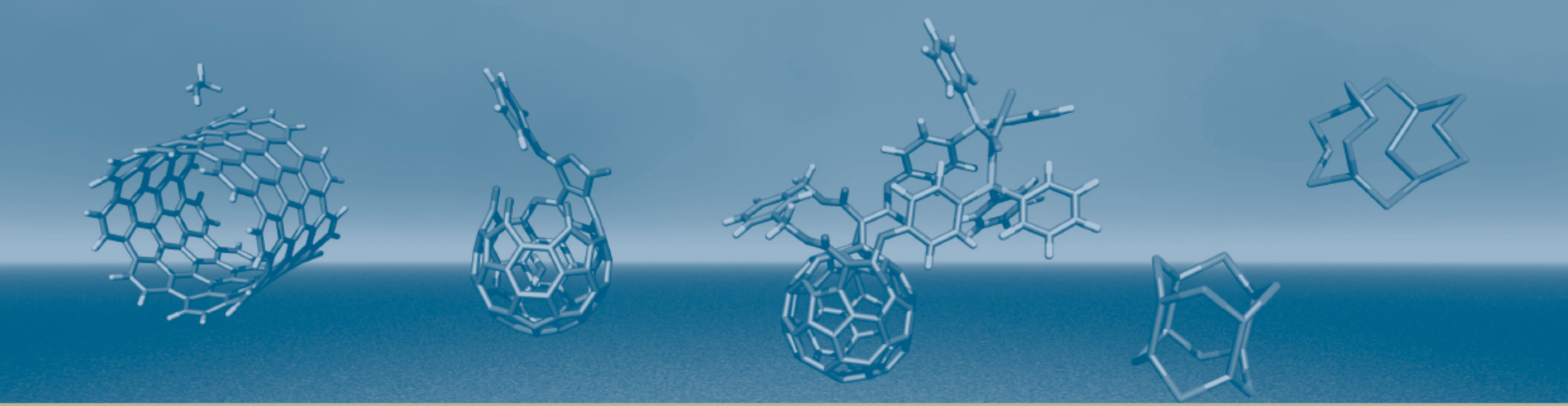

This computational study investigates diverse bonding situations in nanostructures spanning a broad range of energies. Weak, mostly dispersive interactions are examined, as well as covalent metal–ligand and metal–metal bonding. The following systems are presented: small primary alcohols interacting with the inner and outer surfaces of single-walled carbon nanotubes; water encapsulation in open-cage fullerenes; metal complexes with functionalised fullerene ligands; and subvalent metal compounds containing aluminium and magnesium centres in low oxidation states. The results of efficient density functional calculations are compared to those of correlated wavefunction calculations on model systems. This rigorous validation is crucial in evaluating the balance between computational cost and accuracy.

ISBN 978-3-86644-450-8

ISBN 978-3-86644-450-8
9 783866 444508 >